MULTI-MODAL SENSORY INPUT AND NOVEL INTERFACES FOR ROBOTIC PROSTHETIC DEVICES

by

JOSEPH DAVIS SANFORD

Presented to the Faculty of the Graduate School of
The University of Texas at Arlington in Partial Fulfillment
of the Requirements
for the Degree of

DOCTOR OF PHILOSOPHY

THE UNIVERSITY OF TEXAS AT ARLINGTON
August 2016

To Tiffany,

ACKNOWLEDGEMENTS

I would like to thank my supervising professor, Dr. Dan Popa, for the encouragement and motivation during my time as a doctoral student. I would also like to thank him for the invaluable advice given, and thoughtful guidance as well. I wish to thank my dissertation committee Dr. Jonathan Bredow, Dr. Frank Lewis, Dr. Michael Manry, and Dr. George Kondraske for their direction and interest in my research.

I also want to thank Dr. Rita Patterson and Dr. Nicoleta Bugnariu for their insight and guidance designing and analyzing the results of the clinical studies undertaken during my time at the University of Texas - Arlington. I would also like to thank the staff of the University of North Texas - Health Science Center Human Movement Performance Lab for their help during the many hours and days spent conducting these same studies.

I would like to thank all of those that contributed to the NSF Skin Project at NGS.

I am grateful to all of the teachers who have taken the time, and had the patience, to teach me... whether they were in a school room, lecture hall, in a gym or in the ring, or on a trail. Thank you.

Thank you to the friends and family that didn't have me committed when I first told them my not-so-diabolical plan. I would especially like to thank my family, my Mother, Father, Brother, and Sister, for their patience, willing ears, and their encouragement during my pursuit of this research.

Finally, I would like to thank Tony Fernandez for his friendship, inviting coffee shop where I spent so, so many hours working on this thesis, and the uncountable, seemingly bottomless cups of coffee.

August, 2016

ABSTRACT

MULTI-MODAL SENSORY INPUT AND NOVEL INTERFACES FOR ROBOTIC PROSTHETIC DEVICES

JOSEPH DAVIS SANFORD, Ph.D.

The University of Texas at Arlington, 2016

Supervising Professor: Dan O. Popa

Automated systems have progressed to begin allowing for Human-robot interaction and collaboration in the workplace and rehabilitation settings. Seamless collaboration between robotic systems and users requires intuitive modes of interaction and systems with advanced sensing capabilities. The research presented below focuses on identifying human intent through safe, intuitive and optimized input method and sensing.

In this dissertation novel sensor input modalities for Human-Robot Interaction (HRI) are discussed, fundamental research regarding physical Human-Robot Interaction (pHRI) is presented, and solutions towards optimal placement of sensors to facilitate intuitive interfaces are shown. EMG and Pressure: EMG and intrasocket pressure sensors are used in combination with a classifier to create a novel set of input modalities for low encumbrance input to robotic and prosthetic systems. Grip Pressure and Wrist Joint Angle and Human Intent Modeling: fundamental research provided insights in to grip-strategies during human robot interaction, grip-pressure, wrist angle during activities of daily living, and provided data to construct an intent model based on pre-grip arm configuration data. Wrist Velocity: Wrist velocity during activities of daily living is classified in order to im-

prove human-robot interaction. Optimization of Sensor Placement: optimal placement of accelerometers is studied in order to provide compensation for compliant manipulators and control systems.

The objective of this dissertation is to present tools and models which make use of gathered data to guide further development of sensorized robotic skin and improve physical interaction between human users and robotic systems. These tools will allow for more optimal placement of sensors on robotic systems. Improved intent models will be applied in the areas of powered prosthetic devices and rehabilitation robotics as well as industrial systems.

TABLE OF CONTENTS

ACKNOWLEDGEMENTS iv

ABSTRACT v

LIST OF ILLUSTRATIONS xi

LIST OF TABLES xvi

Chapter Page

1. INTRODUCTION 1
   - 1.1 Motivation 3
   - 1.2 Challenges 4
   - 1.3 Research Contribution 5
   - 1.4 List of Publications 6
     - 1.4.1 Conference Papers 7
   - 1.5 Dissertation Organization 9
2. LITERATURE SURVEY 10
   - 2.1 Physical Human-Robot Interaction 10
     - 2.1.1 Sensorized Robotic Skin 10
     - 2.1.2 Rehabilitation Robotics 12
     - 2.1.3 Anatomy of Human Hand 12
     - 2.1.4 Grip Pressure and pHRI 13
   - 2.2 Surface Electro-Myography and Force-Myography 14
     - 2.2.1 Anatomy of Human Forearm 14
     - 2.2.2 EMG Data Acquisition 15
     - 2.2.3 Force Myography 17

        2.2.4 Signal Classification 18
    2.3 Importance of Sensor Placement 19
        2.3.1 Joint-estimation from Acceleration Data 19
        2.3.2 Human Pose Estimation 19
        2.3.3 Noise Modeling 20
        2.3.4 Gesture Recognition through Signal Classification 21
3. Measurements of Interactions between Humans and Objects of Daily Living . . . 23
    3.1 Experimental Determination of Grip-Pressure and Joint-Angle Measurements during Interaction and Activities of Daily Living 23
        3.1.1 Subjects 24
        3.1.2 Sensor Setup and Data Acquisition 24
        3.1.3 Identification of Grip-Pressure During Manipulation of a Weighted Door 28
        3.1.4 Identification of Grip-Pressure and Joint Angle During Manipulation of a Weighted Cylinder 37
    3.2 Wrist Velocity Classification for Human Intent Detection 47
        3.2.1 Classification Methods 48
        3.2.2 Experiment and Data Collection 54
        3.2.3 Experimental Validation 58
        3.2.4 Discussion 62
    3.3 Pressure Sensors 66
        3.3.1 EHD Printed Senors 66
        3.3.2 EHD Senor Array 68
        3.3.3 EHD Printing: Proposed Tasks 69
    3.4 Conclusions 71
4. EMG and EMG-FREE Control of a Powered Prosthetic Device 73

4.1 Multimodal Sensor Inputs for Physical Human-Machine Interface 73
4.1.1 Subjects 74
4.1.2 Experimental Protocol 74
4.1.3 Intra-socket Pressure Measurement 75
4.1.4 Data Acquisition 75
4.1.5 Correlation Analysis 76
4.1.6 Classification 76
4.1.7 Results 78
4.1.8 Correlation Analysis 79
4.1.9 Neural Network 81
4.1.10 Discussion 82
4.2 Heterogeneous Sensor Array for Control of Prosthetic Device 84
4.2.1 Methods 85
4.2.2 Materials 88
4.2.3 Results 93
4.3 Discussion 98
4.4 Control of a Powered Prosthetic via Pinch Gesture and Force Myography . 103
4.4.1 Contact Sensor Thimbles 103
4.4.2 Healthy Limb Socket and Prosthetic Device 104
4.4.3 Data Acquisition of Pressure Sensor Data 106
4.4.4 User Interface Algorithm 107
4.4.5 Experimental Evaluation with Human Subjects 108
4.4.6 Results 110
4.4.7 Usage Scenario Experiment 113
4.4.8 Discussion 113
4.5 Conclusions 117

5. Towards Optimal Placement of Accelerometers 119
  5.1 Introduction 119
  5.2 Noise Considerations during Accelerometer Scaling 120
  5.3 Simulation of Two-link Arm 122
    5.3.1 Kinematics 122
    5.3.2 Dynamics 124
  5.4 Simulation Study 124
    5.4.1 Noise 125
    5.4.2 Root Mean Squared Error 125
  5.5 Conclusions 129
6. Conclusion and Future Work 130
  6.1 Conclusion 130
    6.1.1 Measurements of Physical Interactions between Humans and Objects of Daily Living 130
    6.1.2 Wrist Velocity Classification for Human Intent Detection 131
    6.1.3 EMG and EMG-FREE Control of a Powered Prosthetic Device . . 131
    6.1.4 Towards Optimal Placement of Accelerometers on a two-link system 132
  6.2 Future Work 132
    6.2.1 Towards Optimal Placement of Accelerometers on a two-link system 132
    6.2.2 Development of a Powered Prosthetic Socket using a Heterogeneous Sensor Array 133
    6.2.3 Improvements to Intent Detection During Physical Human Robot Interaction Scenarios 133
7. Aggregated Cohort Data: Activities of Daily Living 134
REFERENCES 143

LIST OF ILLUSTRATIONS

Figure Page

1.1 Project Outline and organization for NRI Project, “Multi-modal sensor skin and garments for healthcare and home robots”. 4

2.1 Bones of the human hand. Phalanges: Distal - yellow, Intermediate - green, Proximal - blue. Forearm: Radius - purple, Ulna- Orange 13

2.2 a) Palmar (anterior view) of the anatomy of the Lower Arm Bones b) Superficial Muscles (*flexor:***a** & **b**, *extensor:* **c** of the Lower Arm 15

3.1 Sensorized Pressure Glove System and Sensor Locations a) Tekscan Versatek Pressure Sensor as worn by Subjects b) Piezoelectric Sensor Locations on Palm of Dominant Hand 25

3.2 Experimental setup and subjects during Grip Pressure and Joint Angle Measurement studies 26

3.3 Reflective Markers as placed on the Subjects during Experimentation. Marker locations seen in red, along with legend describing anatomical location . . . 27

3.4 Visualization of output from Tekscan System during experimental trial. Sensors are marked by anatomical location, as one were to look at the dorsal side of a subject’s hand: 1) distal phalanges 2) intermediary phalanges 3) proximal phalanges 4) metacarpal head 5) thenar and 6) hypothenar. 29

3.5 Maximum Detected Pressure - kPa. Representative Samples illustrating identified grip types 32

3.6 Subject performing three cylinder manipulations 39

3.7 Comparisons of a single subject performing lifting actions using different grip strategies 42
3.8 Cohort Fingertip and Palm Grip Wrist Joint Angle Flexion and Extension compared to Average Cohort Pressure. Wrist Angle and Deviation Ranges (■ - Maximum, ◆ - Minimum) Presented in Degrees. Pressure (solid green line) in kPa. 44
3.9 Cohort Fingertip and Palm Grip Wrist Deviation compared to Average Cohort Pressure. Wrist Angle and Deviation Ranges (■ - Maximum, ◆ - Minimum) Presented in Degrees. Pressure (solid green line) in kPa. 45
3.10 Linear Network Classifier 50
3.11 Fully Connected Multi-layer Perceptron 51
3.12 Cascade Connected Radial Basis Function Classifier 53
3.13 A subject wearing retro-reflective markers and interacting with a sensorized weighted cylinder during data collection 56
3.14 Visualization of data used in this work, including classification and validation methods, and samples rates. 59
3.15 A subject wearing retro-reflective markers and interacting with a sensorized weighted cylinder during data collection 60
3.16 Proposed control system using Human Intent as an input. $\dot{x}$ is the input velocity of the human user's wrist or hand, J is the robot Jacobian 64
3.17 The print path of a single EHD Printed sensor b) View of single sensor through electron microscope c) Aligned print nozzle and sensor above substrate. Images courtesy of [1,2] 68
3.18 Array of Sensors. ZIF Connections can be seen on the right of the figure. Image courtesy of [2] 69

3.19 a) Single packaged sensor b) Single sensor mounted on KUKA youBOT mobile manipulator. Images courtesy of [1,2] 69

3.20 Array of sensors mounted to object for use in pHRI experimentation and usage studies. Image courtesy of [1] 70

4.1 Subject wearing SEMG and pressure sensor housing on the anterior side of their dominant forearm 75

4.2 Signal flow chart illustrating data input vs output of the signal classifier. Inputs include Mean Absolute Value of SEMG, derivative of the Mean Absolute Value, and Absolute Value of the Pressure data. 78

4.3 Pressure Data as collected with the SEMG and piezo-resistive sensor housing in the Ideal, (a) and 2cm Medially Displaced Positions. (b) Voltage vs. Time. A voltage drop indicates force being applied to the pressure sensor. (c) Normalized Magnitude SEMG (blue line) and Pressure Data (red line) . 79

4.4 Output vs Input of the Trained networks. A magnitude rectified, Moving Average of the EMG data is seen in *'blue'*. Pressure data, as a voltage output, is in *'green'*. Output of the MLP network is in *'black'*. The MLP was trained using the data from c) 81

4.5 a) Subject wearing SEMG and FMG collocated sensors b) Subject wearing simulated prosthetic socket and collocated sensors 84

4.6 Arm positions used while gathering data while simulating arm positions found during activities of daily living. a) Arm 45 degrees shoulder flexion in the sagital plane (the hand approximately at waist-level) b) Arm 135 degrees of shoulder flexion in the sagittal plane (hand at approximately head-level) c) Arm out, away from the body (90 degrees abduction) d) Arm laterally across the body (adduction) with their elbow fully extended 87

4.7 Proof of Principle SEMG and colocated piezoresistive force sensor housing. a) Top and b) Side views. The SEMG sensor can be seen (dark grey), with the collocated force sensor (light grey) attached above it, but under the cantilever. 89

4.8 Confusion Matrices comparing Classifiers to Standing Data. Matrices a, c, e, g, used on SEMG data. Matrices b, d, f, h used SEMG and FMG data. a) Classifier 1-EMG_I b) Classifier 2-EMG&FMG_I c) Classifier 3-EMG_ISt d) Classifier 4-EMG&FMG_ISt e) Classifier 5-EMG_ISh f) Classifier 6EMG&FMG_ISh g) Classifier 7-EMG_IStSh h) Classifier 8-EMG&FMG_IStSh 95

4.9 Confusion Matrices comparing Classifiers to Socket Shift Data. Matrices a, c, e, g, used on SEMG data. Matrices b, d, f, h used SEMG and FMG data. a) Classifier 1-EMG_I b) Classifier 2-EMG&FMG_I c) Classifier 3-EMG_ISt d) Classifier 4-EMG&FMG_ISt e) Classifier 5-EMG_ISh f) Classifier 6EMG&FMG_ISh g) Classifier 7-EMG_IStSh h) Classifier 8-EMG&FMG_IStSh 96

4.10 Confusion Matrices comparing Classifiers to Fatigue Data. Matrices a, c, e, g, used on SEMG data. Matrices b, d, f, h used SEMG and FMG data. a) Classifier 1-EMG_I b) Classifier 2-EMG&FMG_I c) Classifier 3-EMG_ISt d) Classifier 4-EMG&FMG_ISt e) Classifier 5-EMG_ISh f) Classifier 6EMG&FMG_ISh g) Classifier 7-EMG_IStSh h) Classifier 8-EMG&FMG_IStSh 97

4.11 Confusion Matrix reporting classification results for radial and ulnar deviation of the hand a) 4 SEMG inputs b) SEMG and FMG inputs 98

4.12 CAD model illustrating Pressure Sensor Housings in Superior and Inferior positions on healthy-limb socket analog (rear view) 104

4.13 The experimental setup, including contact sensors, healthy limb socket, and prosthetic device. The subject can be seen performing a hand extension action with their right hand. 105

4.14 The prosthetic device in the fully open (left) and fully closed (right) positions. 107

4.15 Output of intra-socket force sensors during three grip strategies. Output from flexion motions presented here. Green areas correspond to times when both sensors detect values above threshold. 112

4.16 Prosthetic Device in each of the three closed grip configurations. Index Finger Point (Left) Lateral Grip (Middle) Modified Lateral Grip (Right) 112

5.1 Example of interdigitated accelerometer features. Seismic mass outlined in black 121

5.2 Output of Simulated Study of two-link system joint angle error. RMSE reported for two separate simulations as the number of accelerometers are increased at the end of each link. 126

5.3 Output of Simulated Study of two-link system joint angle error. RMSE vs Number of Sensors. RMSE reported for the four separate simulations of a) 1-4 accelerometers per link with a maximum SNR of 60dB, calculated via scaling, and 0 model uncertainty b) 1-4 accelerometers per link with 0 noise and up to 10% model uncertainty c) 1-4 accelerometers per link with SNR of 60dB and 0 model uncertainty d) 1-4 accelerometers per link with 0 noise and 0 model uncertainty. 128

LIST OF TABLES

Table Page

3.1 Maximum Values Across Cohort (kPa) by Sensor Segment per Action 34
3.2 Aggregated Cohort (Female) Data for action: 3lb Push Door - kPa 35
3.3 Aggregated Cohort (Male) Data for action: 3lb Push Door - kPa 35
3.4 Maximum Pressure Values over Cohort (kPa) by Sensor by Action 40
3.5 Maximum Pressure Values over Cohort (kPa) by Sensor by Action, Top: 3lb Cylinder Middle: 5lb Cylinder Bottom: 10lb Cylinder 41
3.6 Cohort Average and Standard Deviation (σ) for "Lift" Actions: Fingertip (FT), Whole-Hand (WH) 43
3.7 Confusion Matrix reporting classification and error rates for the linear classifier 56
3.8 Confusion Matrix reporting classification and error rates for the K-Nearest Neighbor classifier 56
3.9 Confusion Matrix reporting classification and error rates for the multi-layer perceptron classifier 57
3.10 Confusion Matrix reporting classification and error rates for the radial basis function classifier 57
3.11 Confusion Matrix reporting classification and error rates for the support vector machine 57
3.12 Confusion Matrix of Multi-layer Perceptron Classifier: Experimental Validation using Vicon System at 100Hz 62
3.13 Confusion Matrix of Radial Basis Function Classifier: Experimental Validation using Vicon System at 100Hz 62

3.14 PEDOT:PSS inks tested for EHD Printing Process 67
4.1 Experimental Data Included in Each Training Set for each Neural Network Classifier 93
4.2 Control signals according to sensor input. 108
4.3 Pinch Gesture and ForceMyography: Grip Selection Pattern 110
4.4 Pinch Gesture and ForceMyography: Usage Experiment 114
4.5 Pinch Gesture and ForceMyography: Statistical Measures 115
4.6 Pinch Gesture and ForceMyography: Usage Experiment 116
4.7 Pinch Gesture and ForceMyography: Statistical Measures 117
7.1 Aggregated Cohort (Female) Data for action: Door 6lb Pull - kPa 135
7.2 Aggregated Cohort (Male) Data for action: Door 6lb Pull - kPa 135
7.3 Aggregated Cohort (Female) Data for action: Door 6lb Push - kPa 136
7.4 Aggregated Cohort (Male) Data for action: Door 6lb Push - kPa 136
7.5 Aggregated Cohort (Female) Data for action: Door 11lb Pull - kPa 137
7.6 Aggregated Cohort (Male) Data for action: Door 11lb Pull - kPa 137
7.7 Aggregated Cohort (Female) Data for action: Door 11lb Push - kPa 138
7.8 Aggregated Cohort (Male) Data for action: Door 11lb Pull - kPa 138
7.9 Average Values over Cohort (kPa) by Sensor Segment per Action (Average: $\overline{x}$, Standard Deviation: σ) 139
7.10 Average Values over Cohort (kPa) by Sensor Segment per Action: 3lb Cylinder. Top: Finger Tip. Bottom: Whole Hand. (Average:$\overline{x}$, Standard Deviation: σ) 140
7.11 Average Values over Cohort (kPa) by Sensor Segment per Action: 5lb Cylinder. Top: Finger Tip. Bottom: Whole Hand. (Average:$\overline{x}$, Standard Deviation: σ) 141

7.12 Average Values over Cohort (kPa) by Sensor Segment per Action: 10lb Cylinder. Top: Finger Tip. Bottom: Whole Hand (Average:$\overline{x}$, Standard Deviation: σ) 142

CHAPTER 1

INTRODUCTION

Automated systems have progressed to begin allowing for Human-robot interaction and collaboration in the workplace and in rehabilitation settings. Seamless collaboration between robotics systems and users requires intuitive modes of interaction and systems with advanced sensing capabilities. Novel sensing modes, allowing for interaction between a human user and collaborating machine beyond the familiar text based input, steering wheel, or joystick will allow for improvements in task completion rates, efficiency, and safety[3–7]. This work focuses on sensors used during physical human-robot interaction, including applications within the fields of powered-prosthetic devices and rehabilitation robotics. Applications in the rehabilitation field include physical therapy for stroke patients, namely improving strength and coordination. Strength and coordination training seeks to address a patient's ability to perform tasks found in their daily lives, namely walking, opening and closing doors and cabinets and reaching for, grasping, and manipulating different objects. Rehabilitation devices include table-top two-degree of freedom robotic manipulators (an example being the MIME robot[8]). These systems allow a patient to grasp an end-effector and guides a device to defined locations as a means of improving strength and coordination. While they have proven to be effective, improvements can be made. Applications of the work presented here will allow for improvements to the control systems employed by these devices, the human-intent detection loops, as well as placement and type of sensors used by users to interact with the devices.

In support of this, the National Robotics Initiative project, "Multi-modal sensor skin and garments for healthcare and home robots" seeks to tackle challenges related to designing, fabricating, and integrating multimodal sensors as a means to promote physical-human robot interaction scenarios[9, 10]. These interaction scenarios include powered prosthetic and cooperative robotic, and rehabilitation devices.

Approximately 1 in 190 Americans are currently living with some form of upper-limb loss or amputation today[11]. An estimated additional 185,000 persons undergo an amputation annually. Of these, approximately 41,000 are upper-limb amputations. The first body-powered prosthetic devices were patented in 1857, with improvements reported in 1865 [12][13]. Widespread use of elastic bands to assist in passively holding the end-effector closed came about in 1912, but basic design of these body powered devices have not changed significantly since this time[14]. While an improvement over prior prosthetic devices, the end effectors provided only a single degree-of-freedom and are visually distracting and unpleasant. Powered prosthetic devices are in use in this segment of the amputee population but are seeing limited adoption rates due, in part, to low return on perceived effort by the user. That is to say that the powered prosthetic devices available today are considered heavy, slow to react, difficult to control, uncomfortable, prone to wear, and unsightly. Control algorithms employed by these devices are similarly underdeveloped or non-existent, and do not learn over time nor provide feedback to the user. Improvements in human-intent detection could provide a powered prosthetic user a net-benefit during everyday use of their devices as well as improve their ability to perform basic activities of daily life more readily. This work presents novel, heterogeneous sensor arrays and human-intent detection algorithms whose goal is to address these deficiencies.

Additionally, research towards optimization of the placement of sensors on co-robotic systems has begun. This will allow designers to efficiently place sensors that provide a system with proprioceptive data as well as external information input from a human user during interaction. Through the use of an external sensorized robotic skin, one could imagine a scenario where it could be possible to embue a system with this additional ability even if the robotic-system wasn't originally designed with these abilities.

1.1 Motivation

Man-machine cooperation is enabled by two-way communication between humans and robots. Components of this communication may include Physical Human-Robot Interaction (pHRI) via or pressure transducers, as well input from *non-standard sensors*, such as Surface Electro-Myography (SEMG) and accelerometers. These novel sensor modalities can improve human safety, facilitate learning and training of the robotics system as well as determine human intent during interaction. In this context, sensorized robotic skins that contain embedded force, infrared, and accelerometer sensors have been pursued by numerous researchers [15]. Determination of operating parameters for robotic skin, as well as optimal placement of sensors on the robot are ongoing research topics.

Fundamental studies and data analysis are being driven in an effort to improve collaboration between humans and robots. Traditional robotic systems are unable to safely cooperate in close proximity to human operators and require a safety perimeter around the robot's workcell [4]. Research is being driven with a goal of identifying methods of interaction between a human and robot and supplanting more traditional input and interface devices, keyboards and joysticks and mice, with intuitive devices to feed input in to intent classifiers and control systems.

Improving sensor combinations, placement, and identifying interaction methods is motivated by a need for safe and intuitive interaction between human and robot pairs in open environments. These interactions will not be limited to industrial settings but will include rehabilitation and home, personal, uses. In the context of the larger project[9], the work presented in this thesis is focused on quadrant 4 of Figure 1.1 and feeds information and tools for modeling human-sensor systems in quadrant 1 of Figure1.1 and human-intent models in quadrant two. This work provides fundamental research in to physical human-robot interaction scenarios and feeds information and tools to those researching topics working in quadrant one of Figure 1.1 and human-intent models in quadrant two.

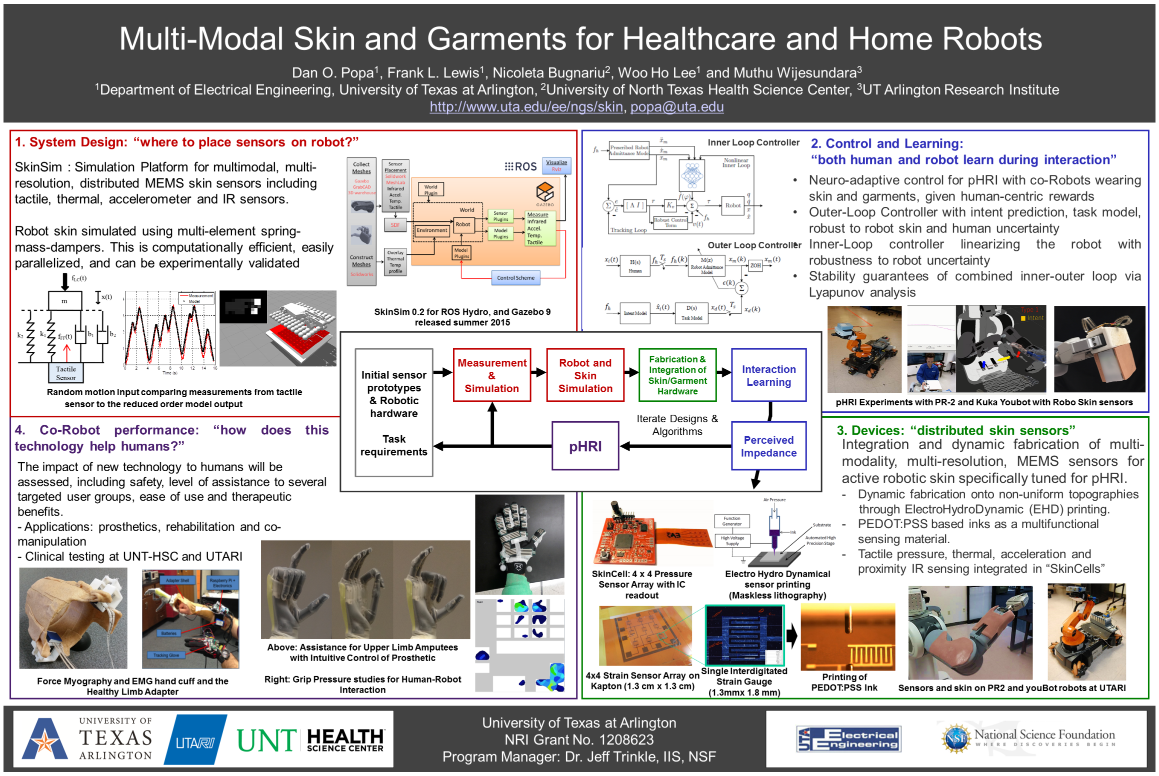

Multi-Modal Skin and Garments for Healthcare and Home Robots

Dan O. Popa[1], Frank L. Lewis[1], Nicoleta Bugnariu[2], Woo Ho Lee[1] and Muthu Wijesundara[3]
[1]Department of Electrical Engineering, University of Texas at Arlington, [2]University of North Texas Health Science Center, [3]UT Arlington Research Institute
http://www.uta.edu/ee/ngs/skin, popa@uta.edu

1. System Design: "where to place sensors on robot?"

SkinSim : Simulation Platform for multimodal, multi-resolution, distributed MEMS skin sensors including tactile, thermal, accelerometer and IR sensors.

Robot skin simulated using multi-element spring-mass-dampers. This is computationally efficient, easily parallelized, and can be experimentally validated

Random motion input comparing measurements from tactile sensor to the reduced order model output

SkinSim 0.2 for ROS Hydro, and Gazebo 9 released summer 2015

2. Control and Learning: "both human and robot learn during interaction"

- Neuro-adaptive control for pHRI with co-Robots wearing skin and garments, given human-centric rewards
- Outer-Loop Controller with intent prediction, task model, robust to robot skin and human uncertainty

Inner-Loop controller linearizing the robot with robustness to robot uncertainty

- Stability guarantees of combined inner-outer loop via Lyapunov analysis

pHRI Experiments with PR-2 and Kuka Youbot with Robo Skin sensors

Initial sensor prototypes & Robotic hardware

Task requirements

Measurement & Simulation

Robot and Skin Simulation

Fabrication & Integration of Skin/Garment Hardware

Interaction Learning

Iterate Designs & Algorithms

Perceived Impedance

pHRI

4. Co-Robot performance: "how does this technology help humans?"

The impact of new technology to humans will be assessed, including safety, level of assistance to several targeted user groups, ease of use and therapeutic benefits.
- Applications: prosthetics, rehabilitation and co-manipulation
- Clinical testing at UNT-HSC and UTARI

Force Myography and EMG hand cuff and the Healthy Limb Adapter

Above: Assistance for Upper Limb Amputees with Intuitive Control of Prosthetic

Right: Grip Pressure studies for Human-Robot Interaction

3. Devices: "distributed skin sensors"

Integration and dynamic fabrication of multi-modality, multi-resolution, MEMS sensors for active robotic skin specifically tuned for pHRI.
- Dynamic fabrication onto non-uniform topographies through ElectroHydroDynamic (EHD) printing.
- PEDOT:PSS based inks as a multifunctional sensing material.
- Tactile pressure, thermal, acceleration and proximity IR sensing integrated in "SkinCells"

SkinCell: 4 x 4 Pressure Sensor Array with IC readout

Electro Hydro Dynamical sensor printing (Maskless lithography)

4x4 Strain Sensor Array on Kapton (1.3 cm x 1.3 cm)

Single Interdigitated Strain Gauge (1.3mmx 1.8 mm)

Printing of PEDOT:PSS Ink

Sensors and skin on PR2 and youBot robots at UTARI

University of Texas at Arlington
NRI Grant No. 1208623
Program Manager: Dr. Jeff Trinkle, IIS, NSF

Figure 1.1: Project Outline and organization for NRI Project, "Multi-modal sensor skin and garments for healthcare and home robots".

1.2 Challenges

Applying human-robot interaction principles to powered-prosthetic systems require addressing certain challenges. *Robotic Sensors*: the sensors of robotic systems need to be able to extract data under non-ideal environments in order to extract meaningful data for control systems. These non-ideal environments can include contamination from human sweat, linear shifts in location or separation from the surface due to change in fit or atrophy, and degradation of signals due to fatigue. *Human Preference*: human users will interact with systems in subtle but significantly different ways, including different input forces and pressures, velocities, physical characteristics and intent. The system's controllers need to be aware of these changing preferences and parameters and be able to adapt.

1.3 Research Contribution

In this dissertation, studies of human-intent are presented, motivating the creation of tools for the control of powered prosthetic devices and improvement of physical human-robot interactions.

1. Clinical Studies of Human-Robot Interaction
    - A clinical study of human interactions with objects during activities of daily living is presented. This study reports wrist joint angle data as well as grip pressure data of human subjects. A representative population of ten volunteer subjects participated in this series of experiments during which a series of objects were manipulated. These objects were a weighted door and a weighted cylinder and are utilized as stand-ins for robot end-effectors and as a means to measure hand interaction pressures, velocities, and joint angles during physical human-robot interaction (pHRI) scenarios.
    - A clinical study correlating Surface Electromyography (SEMG) and Force Myography (FMG) is presented. Two subjects participated in this study, and a novel method is shown allowing control of a powered prosthetic device. Control of these devices is possible as means of activating certain predetermined grip patterns as well as directly controlling grip-types through pattern recognition algorithms.

2. Tools and Models for Human Intent and Sensor Placement Studies
    - A new human intent model based on classification of joint angle data, wrist velocity, and grip pressure data is proposed. It is predicted that wrist-angle and velocity during approach to a robotic manipulator is indicative of the user's desired direction and acceleration profiles of that manipulator during interaction. Grip-pressure is used as a means of continuing user-intent classification during periods of physical contact between the human and robot pair. Results indicate that sensors placed to correspond with the distal joints and palmar areas of the hand can be most effectively used to determine grip type when interacting with a robotic manipulator. Results and analysis can be found in Chapter 3.
    - A tool used to study the optimal placement of sensors on robotic and prosthetic devices is developed. This tool allowed researchers to determine prime positions for accelerometers and numbers of accelerometers to use to achieve a desired estimate of the system state. Estimation of sensor noise can be included in calculations based on the accelerometer's seismic mass.
3. A method for predicting human intent during object manipulation, based on wrist velocity prior to contact, is proposed. In conjunction with advanced control algorithms, such as neuro-adaptive control[16], a system would be able to automatically make changes to system impedance, gains, or reference trajectories and could improve human-robot interaction.

1.4 List of Publications

1. J. Sanford, R. Patterson, and D. Popa, "Concurrent SEMG and force myography classification during times of prosthetic socket shift and user fatigue," conditionally accepted to SAGE Journal of Rehabilitation and Assistive Technologies Engineering, July 2016

2. J. Sanford, K. Tyagi, S. Cremer, M. Manry, D. O. Popa, “Wrist Velocity Classification for Human Intent Prediction and Modeling,” under review IEEE Transactions on Human-Machine Systems

1.4.0.1 Proposed

1. J. Sanford, I. Wijayasinghe, and D. O. Popa, “Comparison of Accelerometry Integration Techniques for 3 Dimensional Manipulator Tracking and Control”, in preparation, International Journal on Advanced Robotics, Fall 2016

1.4.1 Conference Papers

1.4.1.1 Published

1. J. Sanford, C. Young, S. Cremer, D. O. Popa, N. Bugnariu, and R. Patterson, “Grip Pressure and Wrist Joint Angle Measurement during Activities of Daily Life,” *Applied Human Factors and Ergonomics (AHFE), 6th Annual International Conference on*, Las Vegas, Nevada, USA, 2015
2. J. Sanford, R. Patterson, and D. Popa, “Surface EMG and Intra-socket Force Measurement to Control a Prosthetic Device,” *Proceedings of SPIE Vol. 9494, 94940I*, Baltimore, Maryland, USA, 2015
3. J. Sanford, O. Yetkin, S. Cremer, D. and Popa, “A Novel EMG-Free Prosthetic Interface System Using Intra-Socket Force Measurement and Pinch Gestures,” *The 8th ACM International Conference on PErvasive Technologies Related to Assistive Environments*, Corfu, Greece, 2015
4. J. Sanford, C. Young, D. Popa, N. Bugnariu, and R. Patterson, “Grip pressure measurements during activities of daily life,” *Proc. SPIE 9116, Next-Generation Robots and Systems, 91160H*, Baltimore, Maryland, USA, 2014

5. J. Sanford, I. Ranatunga, and D. Popa, “Physical human-robot interaction with a mobile manipulator through pressure sensitive robot skin,” in *Proc. 6th Int. Conf. PErvasive Technol. Relat. to Assist. Environ. - PETRA 13*, New York, New York, USA: ACM Press, 2013, pp. 16
6. C. Nothnagle, J. R. Baptist, J. Sanford, W. H. Lee, D. O. Popa, and M. B. J. Wijesundara, “EHD Printing of PEDOT:PSS Inks for Fabricating Pressure and Strain Sensor Arrays on Flexible Substrates,” in *Proceedings of SPIE Vol. 9494, 94940I*, Baltimore, Maryland, USA, 2015
7. O. Yetkin, K. Wallace, J. Sanford, and D. O. Popa, “Control of a powered prosthetic device via a pinch gesture interface,” in *Proceedings of SPIE Vol. 9494, 94940I*, Baltimore, Maryland, USA, 2015

1.4.1.2 Patents

1. O. Yetkin, J. Sanford, D.O. Popa, K. Wallace, F. Mirza, R. Karulkar, S.K. Das, J.R. Baptist, J.P. Carpenter*“SYSTEMS AND METHODS FOR CONTROLLING DEVICES”* 2016, U.S. Provisional Patent Application Serial No. 62/323,592

1.4.1.3 Other Contributions

1. I. Wijayasinghe, J. Sanford, D. Popa, “Towards Optimal Accelerometer Placement on a Robot Arm”, CASE: 12th Conference on Automation Science and Engineering, 2016
2. O. Yetkin, J. Sanford, F. Mirza, R. Karulkar, S. K. Das, and D. O. Popa, “Control of a Powered Prosthetic Hand via a Tracked Glove,” in *Journal of Medical Devices, Transactions of the ASME, Vol. 9, No. 2, 020920, 01.06.2015*, Minneapolis, Minnesota, USA 2015

3. O. Yetkin, J. Sanford, K. Wallace, and D. O. Popa, “Control of a Powered Prosthetic Device via a Pinch Gesture Interface,” *The Annual Celebration of Excellence by Students (ACES) symposium*, Arlington, Texas, USA, 2015
4. R. Patterson, J. Sanford, C. Young, D. Popa, and N. Bugnariu, “Functional Task Analysis for Human-Machine Performance Limits,” San Antonio, Texas, USA 2014
5. O. Yetkin, K. Wallace, F. Mirza, R. Karulkar, J. R. Baptist, C. Mont, J. Sanford, D. O. Popa, and M. Romero-Ortega, “Blink Controlled Brain Computer Interface Using EEG,” San Antonio, Texas, USA 2014

1.5 Dissertation Organization

Chapter 2 presents previous work found and reports results from the Literature. In Chapter 3, results of physical Human-Robot Interaction studies are reported and applications to Intent Classification and Sensorized Robotic Skin are discussed. Applications of a novel combination of heterogeneous sensors and intent classifier are reported in Chapter 4. Chapter 5 discusses placement of accelerometers for optimal sensor readings. Concluding thoughts, along with future work can be found in Chapter 6.

CHAPTER 2

LITERATURE SURVEY

The objective of this chapter is to present background and prior work regarding human-robot interaction, define anatomical terms, and provide information on current sensor and processing capabilities. Information regarding how future generations of robots will need to interact with people in open workspaces is presented. These robots will not be segregated from their users and will collaborate on shared tasks. Collaborative robots may include rehabilitation devices as well as powered prosthetic devices that are worn by users. As a result, communication between users and their collaborative-robots will need to be intuitive and less constrained. One method of determining a user's desired input will be through the use of direct, physical interaction through sensorized electronic skin covering the robot. The challenges of designing, integrating and use of robotic skins will be guided by the work presented below and studies of multi-modal sensor systems in pHRI situations.

2.1 Physical Human-Robot Interaction

2.1.1 Sensorized Robotic Skin

Successful collaborative task completion relies on effective communication and the ability to work towards a common goal. Human-machine pairs, or dyads, able to communicate have been found to be able to work efficiently during shared tasks[17]. Limited and well defined scenarios have allowed for the use of natural language as a communication method [18, 19]. Work in visual recognition systems has begun to allow for gesture recognition from hand/arm motion or facial expressions within defined scenarios as well[20–24].

While research is ongoing, these studies all require limited work areas and limited input methods.

Physical Human-Robot Interaction (pHRI) has also been investigated [7, 25] as a method of direct physical communication. While Kanda's method required a user to interact with the end effector, Rajruangrabin implemented an Extended Kalman Filter to fuse surface mounted force sensor data with joint data. It was shown that the location of interaction was only limited to the placement of the surface mounted sensor[7].

Sensorized artificial skin for use in pHRI, in commercial and research settings, is currently being pursued. Stretchable sensing fabric including embedded piezo-electric sensors, [26, 27] and epitaxially layered conducting polymer and carbon-filled rubber [28] has been shown. Thin film bendable polyimide sensing arrays [5] have also been shown to be possible. Flexible, non-flat capacitive touch sensor array surfaces have been produced [29–32]. Further information regarding specific flexible arrays of sensors used in the work presented here can be found in Chapter 3.

Previous work completed by Li and Ge [33] discuss physical interaction between a human and a manipulator with unknown dynamics. An adaptive impedance controller was proposed in conjunction with a neural network to collaborate with a human user. Force input, measured at the manipulator by a force-torque sensor, was classified by the neural network and was seen as the primary intent input into the intent detection classifier. Li and Ge found that a reduction in human-applied torque was recorded when using this method, using only "interaction force, position, and velocity" of the human-collaborator[33]. This method requires direct interaction with the end-effector and does not include data prior to contact.

2.1.2 Rehabilitation Robotics

Rehabilitation aides have been developed, making use of robotic systems. Focusing on stroke-rehabilitation of the upper limbs, significant improvements of each subject's reaching speed and range, as well as motion accuracy have been reported[34–38]. These measures have been compared to patients receiving only the standard physical therapy treatments. While different force input methods are used by each system, all systems require forces be applied at only a single point, transducer, or grip location. This limits the functional tasks that can be exercised during therapy. While some of the systems are technically able to move in six degrees of freedom, using a PUMA-560 robot manipulator as the base system, results are only shared for planar movements [37].

2.1.3 Anatomy of Human Hand

Discussion of the human hand requires definition of certain anatomical terms. The radius and ulna attach to the hand via the wrist joint. The radius bone is closest to the thumb joint of the hand. The human wrist is a complicated joint consisting of 8 carpal bones that articulate with each other and with the radius and ulna to provide hand flexion/extension and radial/ulnar deviation and can be modeled as having 2 degrees of freedom. Forearm rotation (pronation/supination) allow the hand to rotate and is a single degree of freedom axis of rotation located from the ulnar head (distally) to the radial head (proximally at the elbow) [39,40].

The human hand consists of 27 bones; 8 bones in the wrist and 19 in the fingers. Each finger contains three bones, save the thumb with two, and are named starting closest to the bones of the metacarpals. This naming proceeds as *proximal*, *intermediate* (excepting the thumb), and *distal phalanges*. The "palmar" side of the hand is the anterior portion of the hand. The *thenar* and *hypothenar* muscle groups activate the thumb and pinky fingers, respectively [39].

Figure 2.1 illustrates the major bones of the human arm and hand. *Distal phalanges* are highlighted in yellow, *intermediate* in green, and *proximal* in blue. The *radius* and *ulna* can be seen in purple and orange, respectively.

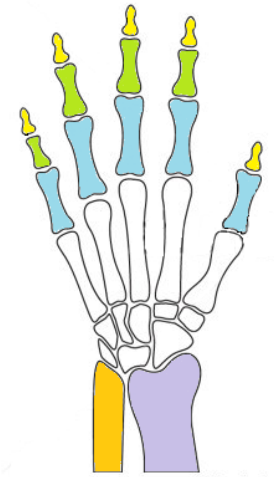

Figure 2.1: Bones of the human hand. Phalanges: Distal - yellow, Intermediate - green, Proximal - blue. Forearm: Radius - purple, Ulna- Orange

2.1.4 Grip Pressure and pHRI

Previous studies have made note of recorded pressures as applied by a user's hand as part of experiments in activities of daily living (ADL). Singh's work sensorized only the distal, thumb, middle and fore-finger pads [41]. Lee reported forces in relation to the cylinders of differing diameters although hand pressure profile data is not reported[42]. Although more detailed information is not available, rehabilitation systems used to assist in physical therapy and rehabilitation have been reported as being under development[43,44].

The normal range of motion of the human wrist has been reported while more recent studies in the literature have focused on the upper extremity joint angles[45]. These include pediatric range of motion studies [46], range-of-motion studies during ADL [47], and [48], as well as other examples.

2.2 Surface Electro-Myography and Force-Myography

Surface Electro-Myography (SEMG), a measure of the electric field generated by activated muscles at the surface of the skin, has been used as a control input both for prosthetic devices and robotic control for rehabilitation applications. A brief discussion of the anatomy of the human arm is included prior to discussing SEMG, as well as other methods of determining voluntary muscle activation.

2.2.1 Anatomy of Human Forearm

Discussions of powered prosthetic devices requires knowledge of the anatomical structures of the human forearm. The humerus bone of the arm inserts at the shoulder and is joined to the radius and ulna at the elbow joint. The radius and ulna attach to the hand via a joint at the wrist. The radius bone is closest to the thumb joint of the hand. “Trans-radial amputation” is defined as, an amputation of the radius or ulna bones occurring below, more distally or “further from” , the elbow. The human shoulder joint is a three degree of freedom joint (DOF), the elbow a one-DOF joint, the forearm a one-DOF joint, and the human wrist a two DOF joint. This is a matter of considering wrist rotation as occurring at the elbow, the insertion point of the radius bone of the forearm to the humerus, instead of at the wrist. [39][40] In Figure 2.2(a), the *radius* bone can be seen in purple, the *ulna* in orange, and the *humerus* in grey. In Figure 2.2(b), the *flexor carpi radialis* and the *flexor carpi ulnarius* can be seen, **a** and **b** respectively, and the three *extensor carpi* muscles can be seen, labeled as **c** For the purposes of this thesis, these muscles are grouped together and referred to simply as *flexor carpi* and *extensor carpi*. This grouping is necessary due to the relatively gross resolution of surface EMG sensors as compared to the size of muscles bundles in forearm.

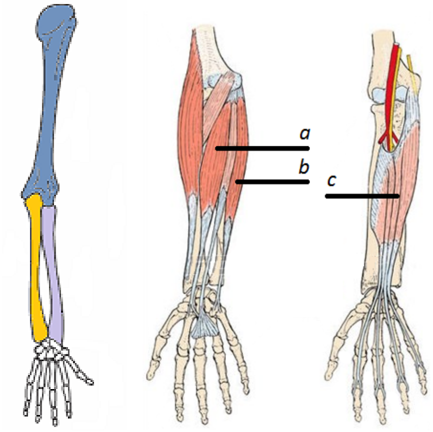

(a) (b)

Figure 2.2: a) Palmar (anterior view) of the anatomy of the Lower Arm Bones b) Superficial Muscles (*flexor:***a** & **b**, *extensor:* **c** of the Lower Arm

2.2.2 EMG Data Acquisition

Prosthetic sockets interfaced with surface myoelectric sensors allow users to control multi-function powered prosthetic devices. Surface myoelectric sensors (surface-EMG or SEMG) detect electrical activity of a user's remaining limb's muscles during activation[49]. Limited control of multi-degree of freedom upper-limb prosthetic devices has been shown to be possible allowing the return of some lost functionality to a user[50]. Upper limb, arm, forearm, and hand, prosthetic users are able to successfully operate multi-degree of freedom devices which include wrist rotation and dexterous digits and thumbs. Human-machine interaction research is under way to improve communication between a subject and their powered prosthetic device. While current devices boast multiple degrees of freedom and improved dexterity levels that allow a user to open doors, pick up bottles and glasses, and apply forces strong enough to carry bags of groceries, interaction with these devices produces fewer movement capabilities than a fully able bodied person and limit a user's functionality outside of the clinical setting[51].

Current state-of-art SEMG sensors allow amputees to control powered prosthetic or robotic devices. These sensors determine muscle activation in a user's residual limb by sensing electrical potential change [49]. It has been extensively reported that amputees have regained some lost functionality through the use of multiple degrees of freedom (DOF) upper-limb prosthetic[50]. After the initial learning curve to use the prosthetic, some users report being able to successfully operate robotic hands which include dexterous digits and thumb motion as well as wrist rotation. Although current powered prosthetic devices provide sufficient dexterity to open doors, grasp glasses and bottles, and carry grocery bags[51], use of these devices continues to be limited outside of the clinical laboratory. Research is underway to address human-robot interaction challenges and improve control of these devices.

Many prosthetic devices offer users control over only a single DOF, thus requiring the user to switch between multiple modes thereby reducing operational speed and increasing task completion length. An example of such a task used in clinical settings is to move a number of small foam balls between two boxes, as described in [50, 52] or [53]. In this case it was reported that the time needed to choose the desired action of the powered prosthetic device, and switch between degrees of freedom, comprises a significant portion of the overall duration of the task [54]. For a multi-DOF prosthetic device, it can be a tedious switching burden to control one-DOF-at-a-time. To improve usability, Pilarski, *et, al.*[54] showed that automatic DOF switching could be learned by a control system using an Actor Critic Model with data collected from a SEMG system. This method predicts which DOF a user is likely to control next through a reinforcement learning algorithm. Improvements in simulated tasks of daily life were reported, in particular task completion times were reduced by approximately 14%[54]. In this study, however, the user was only allowed to quickly move between the relatively gross movements of the elbow and wrist and was only able to successfully function with two DOFs selected at any given time.

Therefore, it is of considerable interest to expand this work to finer and more dexterous movements. However, practical limitations of SEMG sensing technology have often been cited as major challenges for generalizing this approach to SEMG arrays. These limitations include noise and signal degradation over time depending on linear distances along the skin surface above the muscle to be sensed [55–57], and differences between limb poses during classification and training data sets[58]. User fatigue and sweat, perspiration within the socket, can also cause a degraded EMG signal[59–61]. A method to compensate for signal losses due to sweat was studied by Tomasini[62]. In Tomasini's study the EMG sensors used a subject's skin as a common ground. This is still true in modern EMG sensors. This shared ground was highly variable and caused ground-loops; compensation was found to be possible.

2.2.3 Force Myography

Force myography (FMG) has also been reported as a control input. Volumetric changes of the forearm are detected as forces along the surface of the users skin in this method, also referred to as Residual Kinetic Imaging Imaging (RKI), described by Craelius, et al [63–65]. Phillips describes a device containing 32 pressure sensors was used by two transradial amputees to operate a simulated prosthetic hand and operate three separate simulated fingers using only the change in surface forces as detected at the interface of the residuum (the residual amputated limb) and socket[65]. More recently, classification of eight hand motion classes was reported by Radman calling the technique Muscle Pressure Mapping (MPM)[66, 67]. 126 pressure sensors embedded in a simulated prosthetic socket were used. In addition to control of a prosthetic hand, socket fit and grip force prediction have also been verified using intrasocket pressure[68, 69].

2.2.4 Signal Classification

Classification and acquisition of EMG data is highly variable and subject to noise due to linear distances along the surface of the skin above the sensed muscle [55, 56] as well as limb position [58]. User fatigue throughout the day, and perspiration, can also cause degraded device performance. Seeking to improve on classification of EMG signals, research is ongoing in areas including Neural Networks[70, 71], Gaussian Mixture Models[72, 73], and other techniques and have all produced small, but not insignificant, incremental gains in performance[74–77]. However, these studies have only focused on improvements to the algorithms within laboratory settings, not for functional ADL tasks.

Only a small number of studies have considered fusing sensor input modalities as part of the control system. Accelerometers have been used during grip classification along with the more common EMG signal [78]. Grip type information was extracted from time-domain features combined with linear discriminant analysis while the subject's arm was in one of several configurations; neutral resting, raised overhead, stretched to the side, etc[78]. This allowed the classifier to consider the shift of the subject's prosthetic socket as the subject performed simulated ADL. Fougner showed promising results when integrating force sensors with surface EMG to address the issue of force induced artifacts when predicting grip-pressure and showed promising results[79]. More recently, a single accelerometer was integrated with 16 EMG sensors, first mentioned in [80] and later in [81]. The focus of the study was, in general, mobile robot control signals, *ie* “stop”, “turn”, “go”. However, it was shown to be possible to map specific gestures to the motions of an actuated hand [81]. Prosthetic control applications were not explored or discussed. Radmand, et al [67] wrote on the suitability of integrating accelerometer data with EMG data. This study reported that modified training methods, described as “dynamic training”, was necessary [67]. This method minimized the otherwise lengthy amount of time required to allow for training in a wide variety of possibly produced arm positions, which is otherwise clinically impractical.

2.3 Importance of Sensor Placement

A proliferation of inexpensive, small but effective sensors has allowed for research in to large, heterogeneous arrays of sensing devices. This has had the effect of allowing designers to ask questions and seek optimal placement of sensors to provide the maximum information possible. As sizing of individual features is reduced, a balance must also be sought between noise, data integrity, and scaling effects as footprint size shrinks.

2.3.1 Joint-estimation from Acceleration Data

Industrial robot joint-estimation for manipulators has also been reported[82–85]. Wang[86] utilized a 9-axis IMU, along with Extended Kalman Filtering, and reported an RMS error of about 1.5°. Wang made use of an Extended Kalman Filter to fuse accelerometer and gyro-scope data, along with experimental tuning, to achieve an improved estimation accuracy. RMS Error was used as measurement of this improvement.

2.3.2 Human Pose Estimation

Previous work has shown that it is possible to determine state information of two-link systems based on accelerometer data and knowledge of joint-angle limits[87]. The rehabilitation and biomedical fields have found use for these techniques and are being applied in research settings. In [88], Chen’s goal was to map, and validate, human motion using purpose built inertial-measurement units (IMU). Validation of this technique is done using a motion capture system and is applied to walking studies of patients with Parkinsons disease. In a similar fashion, [89] is able to recover lower-limb joint-angles but did not consider relative position. Validation of a novel three-axis sensor, IMU, magnetometer, and gyroscope, was undertaken by Jonsdottir[90] through experimentation. A subject's knee-joint-angle was estimated using the three-axis sensor and compared to video and force-plate data. Lin[91], in a 20 subject study, reported a method providing low joint-angle error through the use of an IMU placed on each limb-segment of the lower body and defined joint-angle limits. An Extended Kalman Filter (EKF) was utilized for state estimation[91]. Seel reported a similar technique in [92] and used three IMU's and joint-angle constraints to compare the IMU's to position and angle data found from reflective markers. Dong, *et al*, and Willemsen before, introduced a method of extracting knee joint-angle data with out integration or filtering[93, 94]. A calibration step was need, as well as IMU positions on the lower leg, as well as a minimum of two IMU's per link. Choudhury, and separately El-Gohary, extracted joint-angle and position data from the human shoulder using IMU's and Extended Kalman Filtering as a way to estimate state-variables of two-link system[95, 96]. Vargas reports a simplified calibration procedure for gait-monitoring, as an alternative to camera based motion capture systems, using IMU's but optimal placement of the sensors is not discussed[97]. Work by Kamalizonouzi[98] states that optimal placement of three accelerometers on a patient's body, in order to detect epileptic seizures, is found. While optimal placement is claimed, noise sources outside of model uncertainties are not considered nor are position values for the limbs calculated. Work presented below considers control system input data in relation the number, size, and placement of sensors.

2.3.3 Noise Modeling

Work has also occurred to model and simulate sensors, including the noise inherent in measurement [99]. Engesser discusses optimization of accelerometers, with the goals of identifying miniaturization limits based on the theoretical noise spectral density, including mechano-thermal, electro-thermal or Johnson noise, and 1/f noise[100, 101]. Levinzon includes an estimate of the amplifier circuit's noise and discussed overall noise of an accelerometer in terms of the Quality Factor[102].

2.3.4 Gesture Recognition through Signal Classification

Further discussion of recent work regarding the active research area of data processing and classification can be found in the literature. Radial Basis Functions are discussed in depth by Tyagi[103, 104]. Dynamic Time Warping considerations, including the need or lack-there-of for signal interpolation, is presented by Rakthanmanon and Keogh[105]. Discussion of the family of K-nearest neighbor classifiers can be found in[106–109].

Recognition of natural human gestures as inputs to machine systems has been studied and reported in the literature. Gribovskaya's work shows promising results for teaching desired actions to robotic manipulators, namely learning the non-linear dynamics of a motion through demonstration[110]. Gaussian Mixture Models (GMM) and Dynamic Motion Primitives (DMP) were used to classify the provided motions off-line, but it should be noted that perturbations in training motions were handled well and all motions were repeated "live". Yanik made use of the *growing neural gas* algorithm for gesture recognition during a rehabilitation scenario[111]. Sanna used a Microsoft Kinect RGB-depth camera to provide directional cues to a quad-rotor through gestures and body positioning. Telemetry data was provided to the system externally from the quadrotor platform itself, external cameras tracked the drone, and navigation in a known indoor environment was possible[20]. Earlier examples of gesture recognition can be found by Chao in 2003[112]. This work accomplishes gesture recognition, making use of edge-detection and template matching. Although not continuous, single gestures were made one at a time, this work did outline basic limitations of gesture recognition systems for use in teleoperation systems including issues with lighting, simplified backgrounds and uniformity of distance from the camera. While the Microsoft Kinect, and driver software, have attempted to address many of these issues, lighting and distance specifically, they are an ongoing research problem. Extensive work has been done making use of the ChaLearn Gesture Dataset, a dataset of 54,000 gestures from a set of 20 categories[113–117]. This work reports results regarding recognition and annotation of recorded sign-language gestures for use in automated dictionary creation and did not make use of real-world distance measures, using relative pixel locations during training. Complex, continuous gestures were not addressed but Dynamic Time Warping (DTW) was used for similarity measurements[115]. Neverova employed deep-learning techniques as well as random data-channel drops to improve classification of the ChaLearn 2014 data set[118].

Neto has addressed the problem of "continuous-gesture detection", that is to say, determining which motions made by a user are a gesture versus which are not a control gesture[119]. Neto uses two separate artificial neural network (ANN) Classifiers. One ANN detects which movements are "not-a-gesture" and the other ANN determines which are "communicative" or "control gestures". In this example, a data-glove is used, as compared to visual image detection, but boasts over a 99% accuracy for a library of 10 gestures. Expanding the gesture detection system's vocabulary to 30 gestures reduces accuracy by only approximately 3%, to 96% accurate[119]. Assad also made use of a physical interface, using electromography (EMG) and an inertial measurement unit (IMU)[80, 81]. Both support vector machine and radial basis function classifiers were implemented and provided users directional control over a mobile ground platform. This physical sensing method avoids some of the issues mentioned above but requires a user to wear an interface device. Applications beyond the control of mobile platforms and teleoperation, including powered prosthetic control. Various classifiers have been used, including multi-layer perceptrons neural networks (MLP)[70, 71] and Gaussian mixture models (GMM)[72–77]. Practical discussions and considerations for fusing multimodal sensing data during powered prosthetic control and signal analysis applications can be found in [67, 78, 120].

CHAPTER 3

Measurements of Interactions between Humans and Objects of Daily Living

The objective of this chapter is to present fundamental research regarding human grip-pressure and wrist joint-angles during activities of daily living. Classification methods are explored and discussed utilizing pre-contact data as a means to facilitate physical human-robot interaction (pHRI). Further work regarding a novel system for human intent detection is also shown.

This chapter is organized as follows: Section 3.1 discusses clinical studies and presents data regarding grip pressure and joint angle identification. Section 3.3 presents preliminary findings regarding the design and production of strain and pressure sensors on flexible substrates. Then Section 3.2 is a presentation of findings and results of intent classification during simulated activities of daily living. Finally, Section 3.4 summarizes results.

3.1 Experimental Determination of Grip-Pressure and Joint-Angle Measurements during Interaction and Activities of Daily Living

In this section, physical Human-Robot Interaction is explored through experimental studies. Determination of human-grip pressure and wrist joint-angle are discussed as they pertain to the design of robotic skin. Discussion of new pHRI learning and control algorithms to determine human intent and for insight in to practical considerations of heterogeneous sensorized robotic skin is presented.

A series of clinical studies were conducted to address the general problem of human intent identification and provide insight in to the design of multi-modal sensorized robotic skin. These studies sought to simulate human-robot interaction by exploring activities of daily living (ADL) using common environmental objects. Subjects interacted with a weighted door and weighted cylinders while standing and seated at a table.

3.1.1 Subjects

A total of ten volunteers agreed to assist with this study. All subjects were between the ages of 23 and 51 years of age, with an average age of 30 years of age. Five males and five females participated in the study. All subjects were right-hand dominant and used their dominant hand throughout this experiment. While hand use was not specifically controlled as a variable in this study, all subjects used their dominant hand, their right hand, during experimentation. All subjects gave written consent after being informed of the test procedure, which was approved by the local ethics review committee (UNTHSC IRB 2011-161).

3.1.2 Sensor Setup and Data Acquisition

A Tekscan VersaTek Grip Measurement System collected pressure magnitude data sampled at 50 Hz. The VersaTek system consisted of 18 separate “sensels”, or sensorized tiles, containing an array of piezo-resistive sensors. The VersaTek system was attached to a leather glove, using adhesive cellophane tape, and worn by the user. Figure 3.1(a) shows the system on the hand. Figure 3.1(b) highlights the Distal sensors (blue), Thenar eminence or Thenar sensors (yellow), and Hypothenar eminence or Hypothenar sensors (purple). These sensors were connected to a computer housing Tekscan software via a cat-5 cable to USB to a proprietary data-acquisition system[30]. Sensors in the Metacarpal Heads, Proximal and Intermediary phalangeal joints are not shown in Figure 3.1(b) but can be seen in 3.1(a). A Hewlett-Packard 1.7 GHz computer, running Microsoft Windows 7 64-bit operating system and software provided by Tekscan, *Grip Research ver. 6.80-21*, is used to collect and analyze all data. The sensors were calibrated and conditioned, as instructed in literature provided by Tekscan, prior to each subject’s use.

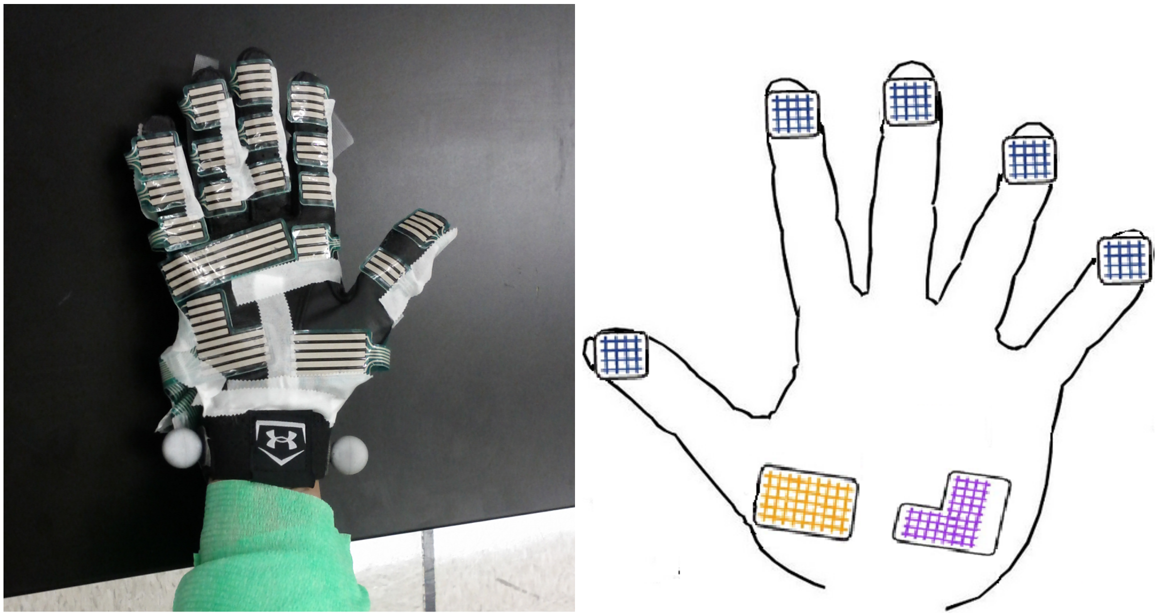

(a) (b)

Figure 3.1: Sensorized Pressure Glove System and Sensor Locations a) Tekscan Versatek Pressure Sensor as worn by Subjects b) Piezoelectric Sensor Locations on Palm of Dominant Hand

Recordings from the Tekscan VersaTek system were exported to .CSV file for analysis. A Matlab, R2012a version 7.14.0.739, script was written to import these .CSV files, parse and read them in to the Matlab work-space. This script allows a user to define which .CSV file to import data from, choose which "sensels" to report data on, and returns information about the Maximum Pressure recorded during each of the below described actions. This script also allows a user to define a threshold and return the number of data samples above that threshold. Subjects interacted with a door mounted on a steel frame and attached to a treadmill and a weighted cylinder. The door is attached to the steel frame using two bi-directional hinges, Model CL3029-6. The door itself weighs approximately 7.35 kg, is 1.08 meters high, .9144 meters wide and 0.03175 thick. A cardboard cylinder 0.21 meters long and 0.0762 meters in diameter was securely attached to the door with carriage bolts. Figure 3.2(a) shows the door used in experimentation along with a subject, seen in the start position for this experiment 3.2(b). During interactions with the weighted cylinder, all subjects were comfortably seated in a chair, in front of a table. The weighted cylinders were placed on top of the table, at the start position. Figure 3.2(c) below shows a subject, illustrating the experimental setup.

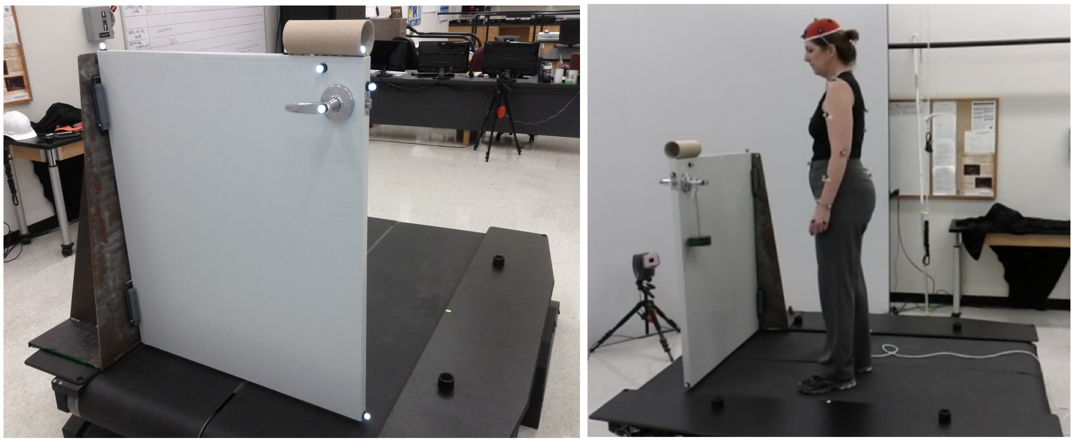

(a) Weighted Door System

(b) Subject wearing reflective markers and Tekscan system seen standing by weighted door system

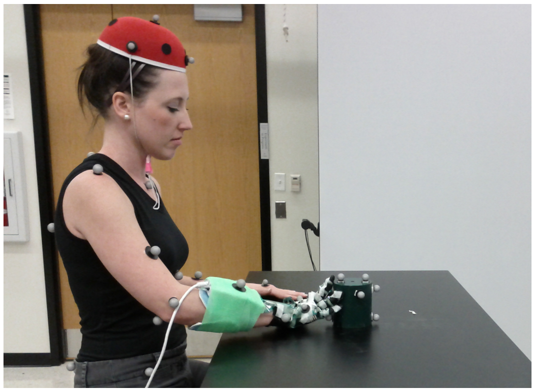

(c) Subject wearing reflective markers and Tekscan system seen seated at table with weighted cylinder

Figure 3.2: Experimental setup and subjects during Grip Pressure and Joint Angle Measurement studies

Motion data was collected with twelve infrared cameras at a rate of 120 Hz through Cortex software version 5.0.1.1496 (Motion Analysis Corp, Santa Rosa, CA). Thirty-three reflective markers were placed on the subject. Only a single marker was used for position detection with respect to the door. Reflective markers were placed on the door as seen in Figure 3.2(a). Seven reflective markers were placed on the cylinder as seen in Figure 3.2(c). Positions of all reflective markers placed on the subjects can be seen in Figure 3.3. A .trc file containing the 3D coordinates of each marker was then imported into Matlab for post-analysis.

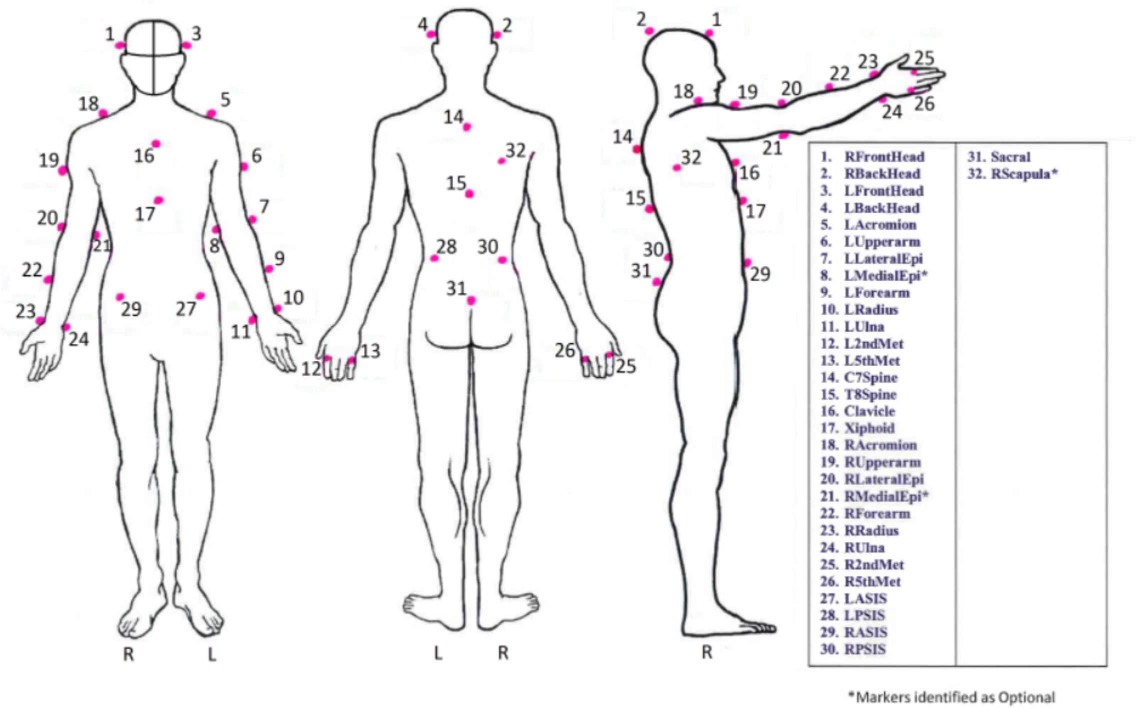

Figure 3.3: Reflective Markers as placed on the Subjects during Experimentation. Marker locations seen in red, along with legend describing anatomical location

3.1.3 Identification of Grip-Pressure During Manipulation of a Weighted Door

Prior to experimentation, basic instruction regarding tasks to be performed were described to the subjects. However, precise hand or arm configurations were not defined or prescribed to the subjects.

Six separate actions were performed by each subject during the course of this study. These actions included opening a weighted door, both by pulling the door towards the subject and by pushing the door away from the subject. Each action′s starting and ending positions were defined and made known to the subjects prior to starting the experiment. No instruction was given to the subjects in regards to the speed necessary to complete each action. Each subject returned to a "ready" position when the task was completed and a test administrator manually notified the subject when to begin the next motion. The pushing and pulling door actions were all completed using the dominant hand. The subjects performed each action at least five times.

The motions performed by each subject were as follows; pull door towards them, and push door away from them. Each action was completed using objects with three different weights. 3 lb., 6 lb., and 11 lb weights were added to the door for this experiment. The door/ weight system totaled 8.71 kg (85.42 Newtons), 10.07 kg (98.75 Newtons), and 12.34 kg (121.01 Newtons) for each of the three respective actions. The weight tasks were randomized to remove any effect of order on the resultant motion. The first five subjects performed actions using the lowest weight first, incrementing weight to medium and then the heaviest weight last. The last five subjects performed actions using the heaviest weight first and then decremented the weight to use the medium and then lowest weight last.

3.1.3.1 Results

Data were collected during a series of experimental sessions. Grip-pressure data were recorded over the course of this experiment and refers to the pressure applied by the palm and fingers of each subject's hand during interactions with the cylinder attached to the weight-door-cylinder system. This data was then exported from the proprietary Tekscan software and extracted from .CSV format as described above. Tables included below report the maximum pressure values recorded over the entire cohort for each sensel during each action performed and represent data from both male and female subjects. Data was sampled continuously but pressure data only corresponds to the time when contact is made between the hand and the door-mounted-cylinder.

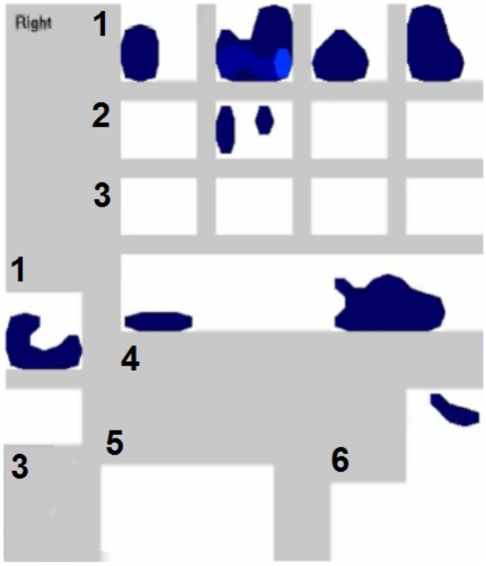

Figure 3.4: Visualization of output from Tekscan System during experimental trial. Sensors are marked by anatomical location, as one were to look at the dorsal side of a subject's hand: 1) distal phalanges 2) intermediary phalanges 3) proximal phalanges 4) metacarpal head 5) thenar and 6) hypothenar.

Data were collected over the entire surface, meaning for the entire sensorized area of the palm. See Figure 3.4. A heat map for a single sample of data illustrates the detected pressures applied by the palmar side of each subject's hand to the cylinder mounted on the door during a single trial of the experiment. While these heat maps are illustrative of an individual's grip throughout a particular trial, Figures 3.5(a)- 3.5(d) show representative grip strategies as seen during these same experimental sessions. The data shown in Figures 3.5(a)- 3.5(d) are plots of the *maximum detected pressure per action, over the entire trial, per sensel*. That is to say that for each opening or closing action of the door, the maximum detected pressure applied at each sensel location on the subject's palm was recorded.

Through comparison of the maximum detected pressures over the palm by sensor region, anatomical location, it can be seen that the sensors located on the intermediary and proximal joint locations of the fingers and metacarpal heads detected relatively small pressure values as compared to those of the fingertip distal and palm regions. Over all grip strategy was therefore categorized using only the distal and palmar sensels. Figure 3.5(a) shows data from a single individual, including intermediary and proximal joint data. Figure 3.5(b) shows data from this same individual, for the same trial, removing intermediary and proximal joint data. Grip strategy for the entire cohort was determined in this manner, allowing for clarification of the grip strategies employed by each individual within the cohort.

Subject 8, Figure 3.5(a) and 3.5(b), is an example of a "Palm Only" grip. Examples of "Fingertip Only" and "Fingertip and Palm" can be seen in Figures 3.5(c)- 3.5(d), respectively.

Three grip strategies were identified for the cohort. Two subjects employed a "Palm" strategy, four subjects employed a "Finger-tips only" strategy, and four subjects were seen to use a combination of "Both" the finger-tips and the palm while interacting with the cylinder mounted on the door-system. No significant gender bias was seen across the cohort and each subject's preferred strategy seems to stay constant throughout the experiment. Future studies may provide further insight in to ratios of grip strategies across the population as no conclusions should be drawn from these data other to say that an individual's grip strategy seems to remain constant for a particular action.

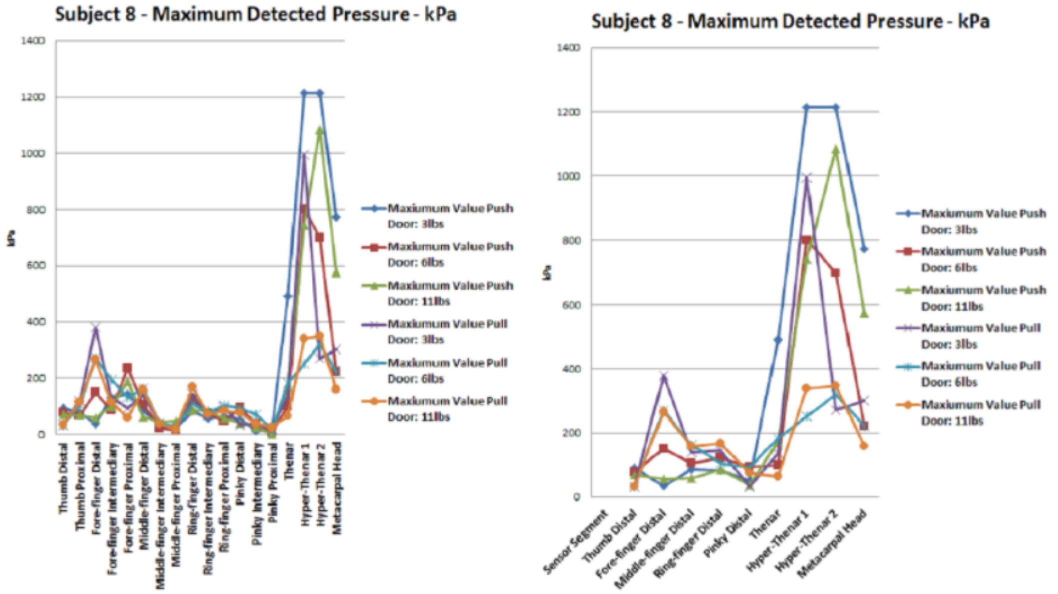

(a) Subject 8 including data from all sensorized regions of palm

(b) Subject 8 output including data from only the Distal sensors, a "Palm Only" Grip

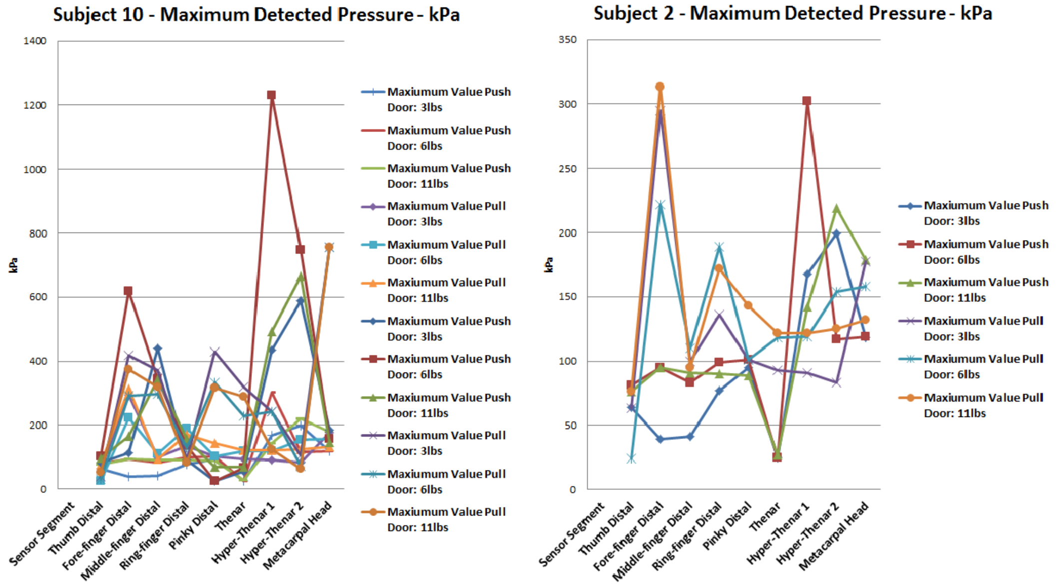

(c) Subject 10 including data from all sensorized regions of hand, a "Fingertip Only" Grip

(d) Subject 2 including data from all sensorized regions of hand, a "Fingertip and Palm" Grip

Figure 3.5: Maximum Detected Pressure - kPa. Representative Samples illustrating identified grip types

It should be noted that data from two subjects were discarded from analysis as they were found to be more than two standard deviations below the cohort mean for particular actions. After evaluation of the pressure data, it is believed that that individual subject's interactions with the door-mounted-cylinder occurred outside of the operating area of the Tekscan Gripper system's sensors. Namely, on an unsensorized area of the palm.

A table reporting the maximum pressure values across the cohort, by sensor segment, by action can be seen in Table 3.1 . Tables 3.2- 3.3 report cohort data by gender. A note should be made regarding the "SUM" reported in the tables. This "SUM" value has no physical meaning and should only be used when making a general comparison between overall trend data and total applied pressure by each subject. Entries for "Hypothenar 1" and "Hypothenar 2" are in reference to the physical sensel locations on the subject's hands. Each of these areas are described in Figure 3.4. These data provided guidance when considering performance parameters of the sensor arrays reported in 3.3.

Table 3.1: Maximum Values Across Cohort (kPa) by Sensor Segment per Action

	Push Door: 3lbs	**Pull Door: 3lbs**	**Push Door: 6lbs**	**Pull Door: 6lbs**	**Push Door: 11lbs**	**Pull Door: 11lbs**
Sensor Segment	**Max Values**	**Max Values**	**Max Values**	**Max Values**	**Max Values**	**Max Values**
Thumb Distal	159	131	210	151	340	355
Proximal	82	119	330	102	310	167
Fore-finger Distal	295	482	619	307	430	373
Intermediary	272	196	145	505	208	316
Proximal	215	112	236	129	186	108
Middle-finger Distal	439	370	344	296	344	318
Intermediary	161	209	152	178	126	170
Proximal	178	244	196	257	191	187
Ring-finger Distal	330	215	400	290	519	282
Intermediary	163	117	92	136	146	129
Proximal	171	139	199	298	180	197
Pinky-finger Distal	415	429	274	334	198	317
Intermediary	125	420	167	386	110	292
Proximal	161	240	214	456	214	180
Thenar	582	319	456	228	582	301
HyperThenar 1	1214	995	1230	252	743	1096
HyperThenar 2	1214	271	747	319	1086	348
Metacarpal Head	774	755	329	755	576	755

Table 3.2: Aggregated Cohort (Female) Data for action: 3lb Push Door - kPa

Push Door: 3lbs

	Subject 1	**Subject 2**	**Subject 3**	**Subject 5**	**Subject 7**
Thumb Distal	159	64	97	71	94
Proximal	29	5	51	82	60
Distal	122	39	35	43	43
Intermediary	21	42	14	16	29
Proximal	14	56	18	14	16
Middle-finger Distal	89	41	67	36	139
Intermediary	18	28	17	14	19
Proximal	26	22	13	15	12
Ring-finger Distal	330	77	66	51	287
Intermediary	163	34	13	13	64
Proximal	171	33	25	16	74
Pinky Distal	415	95	60	13	103
Intermediary	89	113	125	18	27
Proximal	161	48	94	10	54
Thenar	48	25	16	582	32
HyperThenar 1	157	168	79	81	294
HyperThenar 2	118	199	12	30	249
Metacarpal Head	35	118	182	120	219
Sum	**2165**	**1207**	**984**	**1225**	**1815**

Table 3.3: Aggregated Cohort (Male) Data for action: 3lb Push Door - kPa

Push Door: 3lbs

	Subject 6	**Subject 8**	**Subject 10**	**Subject 11**	**Subject 12**
Thumb Distal	53	93	84	115	122
Proximal	57	77	14	70	54
Distal	18	36	114	43	295
Intermediary	9	129	272	40	104
Proximal	6	143	215	40	48
Middle-finger Distal	56	87	439	42	76
Intermediary	13	28	161	25	67
Proximal	9	15	178	18	25
Ring-finger Distal	28	83	92	100	126
Intermediary	22	54	52	78	99
Proximal	9	63	63	83	50
Pinky Distal	82	50	26	40	50
Intermediary	20	14	103	51	34
Proximal	4	21	103	23	13
Thenar	3	491	56	69	14
HyperThenar 1	26	1214	434	280	193
HyperThenar 2	34	1214	588	194	169
Metacarpal Head	9	774	184	77	176
Sum	**458**	**4586**	**3178**	**1388**	**1715**

Tables reporting Aggregated Maximum Values for the remaining trials can be found in Appendix 7.

Disregarding Proximal and Intermediary joint pressure data was done due to the relatively low contribution by these joint's data when compared to that over the entire hand and over the entire cohort. The number and density of sensors has practical implications for future pHRI scenarios and systems. Sensorized robotic skin with lower performance metrics than what is otherwise possible from the capabilities of state-of-the-art systems can be considered, with appropriate safety-factor to ensure proper operating range.

3.1.3.2 Discussion

The task in this experiment was designed to model interaction with a robot that has a cylindrical arm or end-effector. Others have reported similar results in the literature, making use of different systems and experimental protocols. Singh[41] reported on a custom system for use in grip measurement in upper limb rehabilitation exercises. A patient would interact with common objects such as a coffee cup, bottle, and water glass, while being monitored by a physiotherapist. Tekscan sensors, as well as other off the shelf components, were used in this application, although specific model numbers are not mentioned. The distal fore and middle finger pads and the distal thumb pad were sensorized. Force information data was reported for healthy subjects although the object's weights used in this experiment were not reported. From their writing though, it is surmissed that in Singh's study, subjects lifted much lighter objects from a table top than those found here. The heaviest object, the bottle filled with 400mL of water, was only a fraction of the weighted-door system's weight.

Singh's system was reported to have sensors only on the Distal thumb, middle and fore-fingers. The sensor system used in this study had a total of 18 sensing areas covering a much larger interaction area. Lee [42] employed the use of a "TeckStorm, Inc. Force

Sensing Resistor Sensor”. Lee’s study had a goal of determining the relationship between handle diameter and force distribution. Cylinders of various length and diameter were held aloft for a short, but unreported, time period. While the weight of the cylinder was not noted, this system employed 28 sensors placed over the entire hand in a similar fashion to the Tekscan system’s placement in this study.

Singh’s maximum reported force at the distal fore-finger of approximately 0.70 kgf converts to approximately 96 kPa, if a Flexiforce A201 sensor assumed. While lower than the maximum pressures reported on in our study, this value is not significantly lower than the values reported on by subjects preferring a ”finger tip only” grip strategy when interacting with the weighted-door system at the lower added weight. It should also be noted that in Lee, the maximum force reported by Lee was 11.5 N. Assuming a similar sensing area as to that in Singh, the maximum reported pressure was 161 kPa. Again, well within values seen during this study even though the function, or task, in this study was different. However, one limitation in the current study is that opening a door with a cylinder mounted on top was used for the task and this only uses a single degree of freedom nor does it model interacting with a door handle.

3.1.4 Identification of Grip-Pressure and Joint Angle During Manipulation of a Weighted Cylinder

Before experimentation, volunteers were given basic instruction and informed of the tasks to be performed. Precise hand and arm configuration instructions were not given, however. During the course of this study, the subjects performed six separate actions. These actions included lifting a weighted cylinder off of a table top. All actions were performed while seated comfortably in a chair. Subjects were instructed on the starting positions for each action prior to the start of the experiment and instructed to return to a “ready” position when the task was completed. A test administrator manually prompted each subject as to the start of the next motion. Volunteers were not given instruction in regards to the speed required to complete each prescribed action. The lifting motions were all performed using the dominant hand. The subjects performed the actions at least five times.

The motions performed by each volunteer were; lift a 3lbs. (1.361kg) cylinder above a table surface, lift a 5lbs. (2.268kg) cylinder above a table surface, and lift a 10lbs. (4.536kg) cylinder above a table surface (13.347, 22.241, and 44.483 Newtons, respectively). During this “lifting” action, the subjects were instructed to lift the cylinder to a comfortable height using either their “fingertips” or “Whole-Hand” depending on the action. No further instructions regarding the required height or speed of the lifting motion was given to the subject. The weight tasks were randomized amongst the volunteer population to remove any effect of order on the resultant motions. The first five subjects performed actions using the lowest weighted cylinder first, increasing to the medium weight, and then using the heaviest weight last. The last five subjects performed the required actions using the highest weighted cylinder first, middle weight, and then lightest weight last. Figures 3.6(a)- 3.6(c)illustrate a subject performing the three basic motions of “pushing a cylinder across a surface”, “pulling a cylinder across a surface”, and “lifting a cylinder above a surface”.

3.1.4.1 Results

Continuing work discussed above, data were collected during a series of experimental sessions. Grip-pressure data were recorded over the course of this experiment and refers to the pressure applied by the palm and fingers of each subject’s hand during interactions with the cylinder attached to the weight-door-cylinder system. This data was then exported from the proprietary Tekscan software and extracted from .CSV format as described above. Tables included below report the maximum pressure values recorded over the entire cohort for each sensel during each action performed and represent data from both male and female

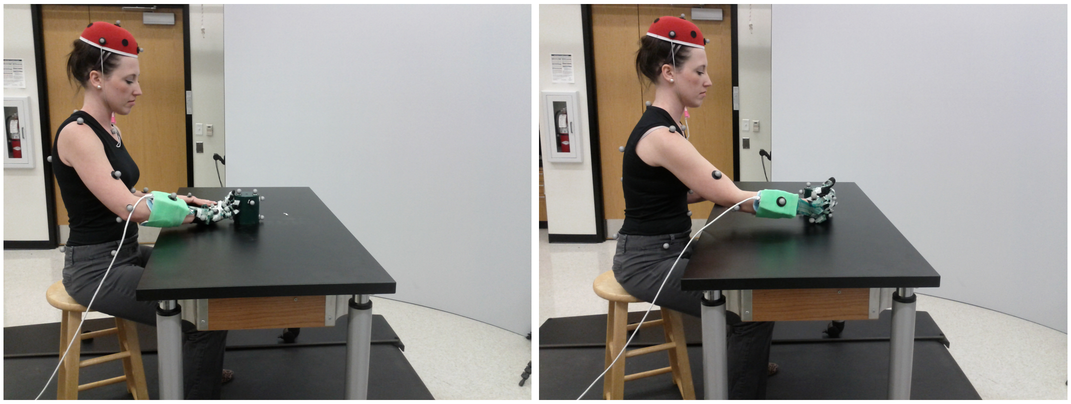

(a) Pushing a weighted cylinder (b) Pulling a weighted cylinder

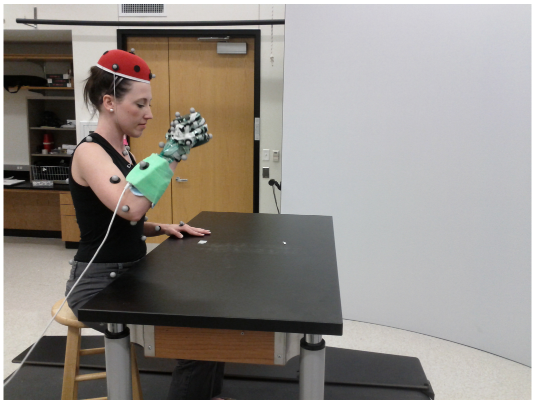

(c) Lifting a weighted cylinder

Figure 3.6: Subject performing three cylinder manipulations

subjects. Data was sampled continuously but pressure data only corresponds to the time when contact is made between the hand and the cylinder. door-mounted-cylinder. Wrist Joint-angle measurements were determined using the Cortex reflective marker system described above.

The information in Table 3.5 reports the cohort's Aggregated Maximum pressure values. These tables report the Maximum pressure values for the entire cohort, for each sensel during the performed actions. Pressure data was recorded during each action. Data for the Proximal and Intermediary Sensels were excluded from final analysis due to their relatively small contribution as compared to the Distal and Palmar sensels. The separate entries in 3.4

for “Hypothenar 1” and “Hypothenar 2” are in reference to the physical “sensel” locations on the subject’s hands. “Hypothenar 2” and “Hypothenar 1” are the yellow and purple highlighted sections in Figure 3.1(b). Entries for the summation of the pressure values are included at the bottom of each table. This summation should only be used as a method to view general trends amongst the cohort. For the “10lb Fingertip Only Lift” action, only a total of eight data points are included. Two of the five female subjects were unable to lift the 10lb cylinder using only their fingertips. These incomplete actions are not included in the comparison for Maximum Pressure nor for the Average Cohort Pressure Data used in later sections. The “3lb Lift”, “5lb Lift”, and “10lb Lift Whole-Hand” actions contain data for the entire cohort. Representative Maximum Pressure data for a subject is shown in Figures 3.7(a) and 3.7(b).

Table 3.4: Maximum Pressure Values over Cohort (kPa) by Sensor by Action

	3lb Lift		**5lb Lift**		**10lb Lift**	
	Fingertip	**Whole-Hand**	**Fingertip**	**Whole-Hand**	**Fingertip**	**Whole-Hand**
Thumb Distal	345	325.00	474	459	874	1004
Fore-finger Distal	218	271.00	622	352	454	344
Middle-finger Distal	344	265.00	809	474	335	1109
Ring-finger Distal	311	331.00	781	311	247	370
Pinky Distal	255	214.00	364	197	300	403
Thenar	65	256.00	64	306	109	347
Hypothenar 1	152	468.00	381	791	222	294
Hypothenar 2	138	584.00	143	304	910	1230
SUM	**1828.00**	**2714.00**	**3638.00**	**3194.00**	**3451.00**	**5101.00**

Joint-Angle data was recorded as described above in Section 3.1.2. Average joint-angles during an action-cycle were determined. An action-cycle is defined as a subject starting from rest, contacting the object, moving the object in the defined action, ceasing

Table 3.5: Maximum Pressure Values over Cohort (kPa) by Sensor by Action, Top: 3lb Cylinder Middle: 5lb Cylinder Bottom: 10lb Cylinder

	Push	**Pull**	**Lift**	**Push**	**Pull**	**Lift**
	Finger Tip Grip			**Whole-Hand Grip**		
Thumb Distal	385	285.00	345	420.00	267	325.00
Fore-finger Distal	328	187.00	218	246.00	193	271.00
Middle-finger Distal	322	378.00	344	378.00	278	265.00
Ring-finger Distal	115	246.00	311	140.00	351	331.00
Pinky Distal	232	197.00	255	292.00	317	214.00
Thenar	65	98.00	65	210.00	225	256.00
Hypothenar 1	186	234.00	152	256.00	299	468.00
Hypothenar 2	298	489.00	138	311.00	777	584.00
SUM	**1931.00**	**2114.00**	**1828.00**	**2253.00**	**2707.00**	**2714.00**

	Push	**Pull**	**Lift**	**Push**	**Pull**	**Lift**
	Finger Tip Grip			**Whole-Hand Grip**		
Thumb Distal	979	559	474	534	325	459
Fore-finger Distal	265	293	622	208	257	352
Middle-finger Distal	322	548	809	274	287	474
Ring-finger Distal	265	341	781	232	489	311
Pinky Distal	328	300	364	249	197	197
Thenar	91	73	64	210	227	306
Hypothenar 1	224	536	381	264	243	791
Hypothenar 2	731	307	143	143	189	304
SUM	**3205.00**	**2957.00**	**3638.00**	**2114.00**	**2214.00**	**3194.00**

	Push	**Pull**	**Lift**	**Push**	**Pull**	**Lift**
	Finger Tip			**Whole-Hand**		
Thumb Distal	874	365	395	499	295	1004
Fore-finger Distal	454	897	1270	721	437	344
Middle-finger Distal	335	827	1109	444	613	1109
Ring-finger Distal	247	260	255	341	440	370
Pinky Distal	300	387	600	292	317	403
Thenar	109	65	73	79	181	347
Hypothenar 1	222	87	105	149	246	294
Hypothenar 2	910	225	133	233	535	1230
SUM	**3451.00**	**3113.00**	**3940.00**	**2758.00**	**3064.00**	**5101.00**

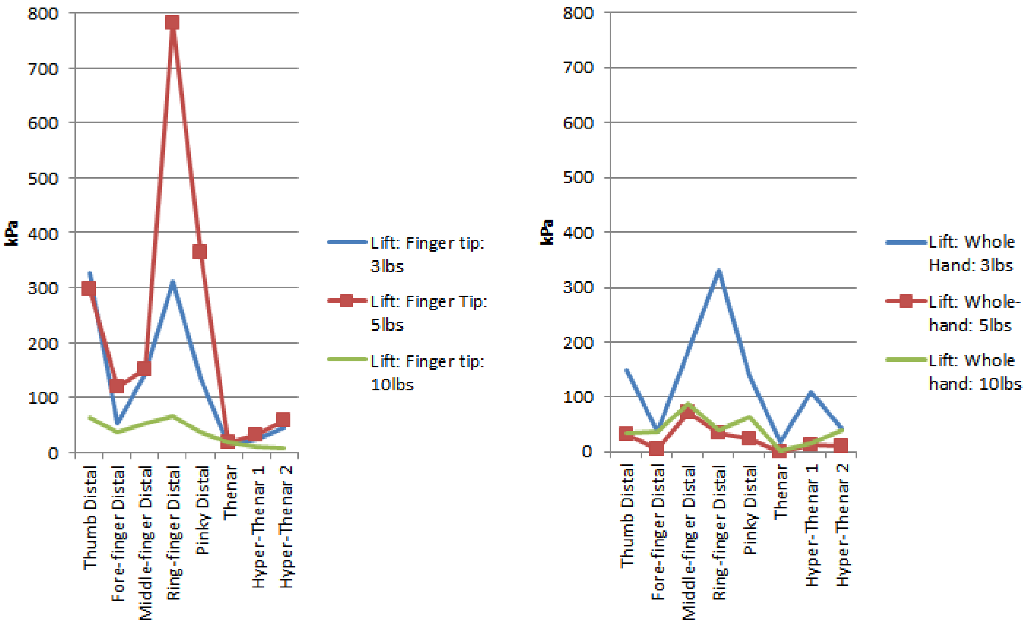

(a) (b)

Figure 3.7: Comparisons of a single subject performing lifting actions using different grip strategies

contact, and returning to the rest position. The average joint-angle during each action-cycle was found by averaging the 10 joint-angle samples prior to the time-index for the determined Maximum pressure, the joint-angle at the time-index of the determined Maximum pressure, and the 10 joint-angle samples occurring after the time-index for the determined Maximum pressure. A positive wrist angle is representative of a wrist extension action. A positive wrist deviation value is representative of a wrist radial deviation. Figures 3.8(a)-3.9(c) illustrate the cohort's wrist joint-angle and joint-deviation ranges and average at Maximum pressure of each "sensel" for the the "3lb Lift Fingertip", "5lb Lift Fingertip", and "10lb Lift Fingertip" actions. Figures 3.8(d)-3.9(f) report data for the "Lift Whole-Hand" actions. That is to say, the data shown in Figures 3.8(a)-3.9(c) is for actions where the subjects were instructed to only use their fingertips while manipulating the cylinder. In Figures 3.8(d)-3.9(f), the subjects were allowed to use their "Whole-Hand" to grasp

Table 3.6: Cohort Average and Standard Deviation (σ) for "Lift" Actions: Fingertip (FT), Whole-Hand (WH)

	3lb FT Average	σ	**3lb WH Average**	σ	**5lb FT Average**	σ	**5lb WH Average**	σ	**10lb FT Average**	σ	**10lb WH Average**	σ
Thumb Distal	209.3	112.9	134.3	85.1	182.8	132.1	130.9	131.5	151.2	109.4	284.1	284.1
Fore-finger Distal	132.2	69.7	112.9	90.9	206.9	204.9	111.7	112.8	337.8	411.3	103.1	103.1
Middle-finger Distal	141.9	90.5	118.7	72.3	203.5	218.8	142.9	126.5	229.5	314.9	311.2	311.2
Ring-finger Distal	157.7	81.2	150.0	91.6	214.2	220.7	152.6	106.9	156.1	74.9	130.9	130.9
Pinky Distal	109.0	63.9	85.3	67.4	129.8	109.2	66.7	58.8	169.1	165.7	116.8	116.8
Thenar	38.1	20.0	53.6	73.3	26.5	20.9	64.6	95.1	31.2	24.5	101.6	101.6
Hypothenar 1	39.8	42.7	126.0	133.2	55.6	115.4	170.5	247.6	34.6	35.4	97.2	97.2
Hypothenar 2	52.0	36.1	114.3	172.7	46.1	45.6	82.0	103.9	42.9	42.4	379.3	379.3
SUM	**880.0**		**895.1**		**1065.4**		**921.9**		**1152.4**		**1524.1**	

the cylinder. This study reports on average wrist angles. Shoulder and elbow angles are excluded, at this time, because of the variability due to each subject's posture and arm path during each action.

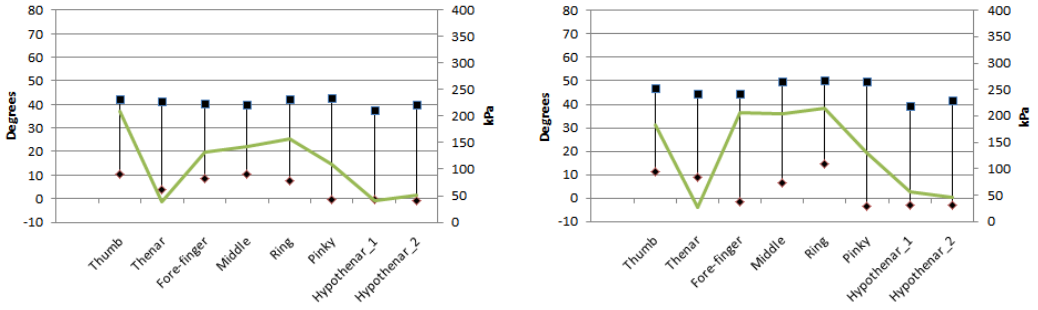

(a) 3lb Lift: Fingertip Wrist Angle

(b) 5lb Lift: Fingertip Wrist Angle

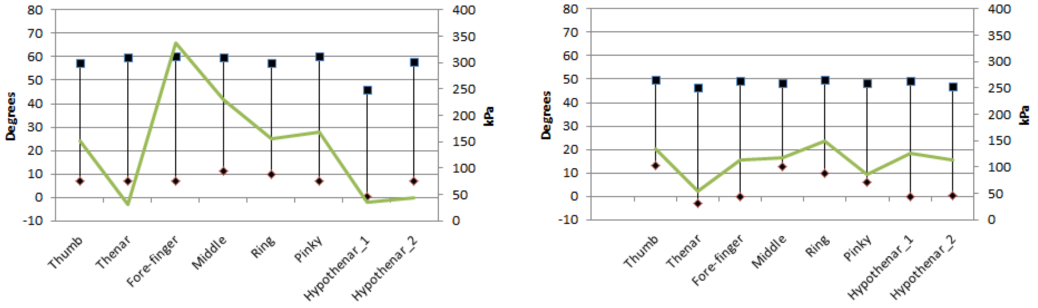

(c) 10lb Lift: Fingertip Wrist Angle

(d) 3lb Lift: Palm Wrist Angle

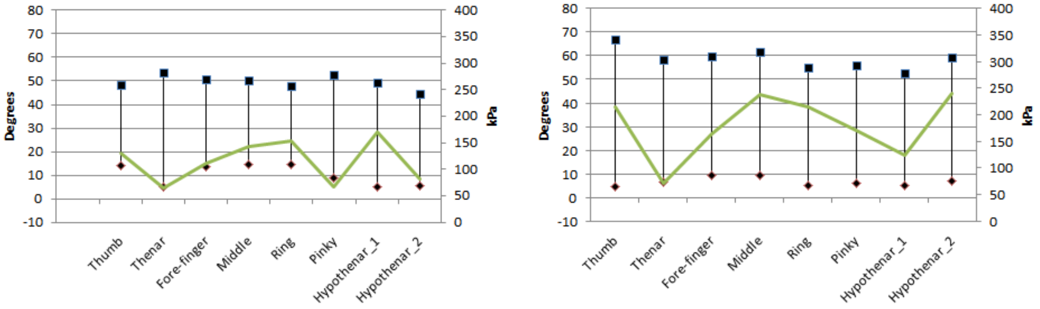

(e) 5lb Lift: Palm Wrist Angle

(f) 10lb Lift: Palm Wrist Angle

Figure 3.8: Cohort Fingertip and Palm Grip Wrist Joint Angle Flexion and Extension compared to Average Cohort Pressure. Wrist Angle and Deviation Ranges (■ - Maximum, ◆ - Minimum) Presented in Degrees. Pressure (solid green line) in kPa.

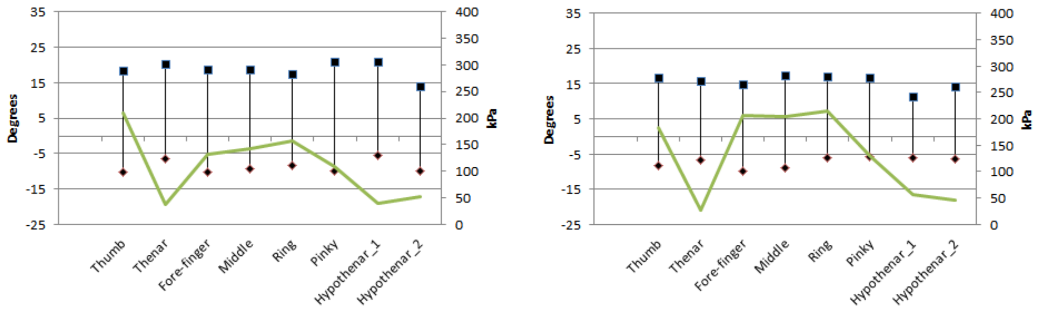

(a) 3lb Lift: Fingertip Wrist Deviation

(b) 5lb Lift: Fingertip Wrist Deviation

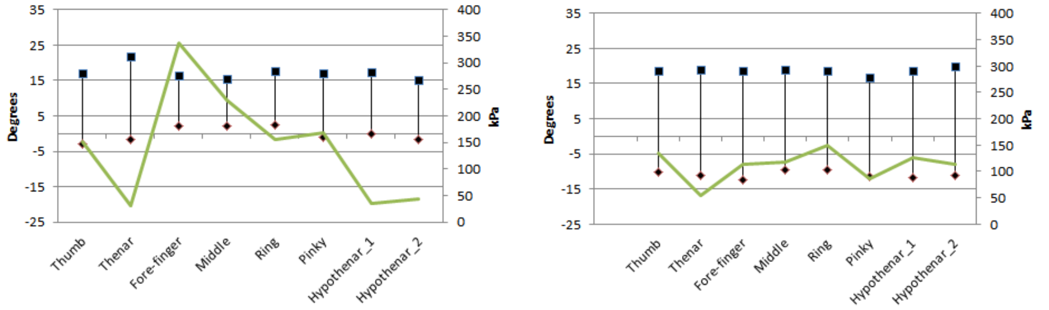

(c) 10lb Lift: Fingertip Wrist Deviation

(d) 3lb Lift: Palm Wrist Deviation

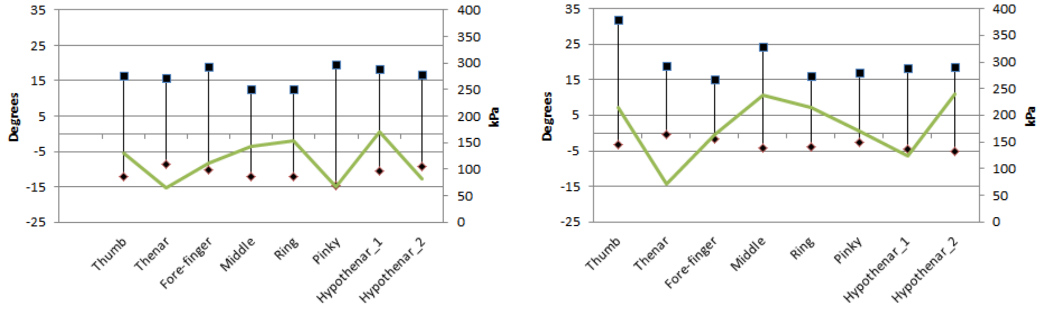

(e) 5lb Lift: Palm Wrist Deviation

(f) 10lb Lift: Palm Wrist Deviation

Figure 3.9: Cohort Fingertip and Palm Grip Wrist Deviation compared to Average Cohort Pressure. Wrist Angle and Deviation Ranges (■ - Maximum, ◆ - Minimum) Presented in Degrees. Pressure (solid green line) in kPa.

3.1.4.2 Discussion

Subjects in this study performed actions chosen to represent interactions with a model robotic end-effector. Average Grip Pressure data is presented for each action and weighted cylinder along with wrist joint-angle and wrist joint-deviation during the interaction. Table 3.4 shows Maximum pressure data in kPa while Figures 3.8(a)-3.9(f) present wrist joint-angle and wrist deviation-angles, along with Average Cohort pressure data. This Average Cohort pressure data and joint-angles and joint-deviations are from both male and female subjects and have the potential to provide insight in to human intent during pHRI scenarios. Wrist angles during the Palm Grip types were higher, and had higher ranges, as compared to the same action with the Fingertip Grip Strategy. Wrist Deviation Angles followed a similar trend. But, specific measurements during the 10lb Lift: Palm experiment did show higher maximum wrist deviation angles than those for the 5lb and 3lb Lift: Palm actions. However, the over all range of motion for the 10lb Lift: Palm wrist deviation is generally decreasing by comparison. During actions requiring lifting of increased loads, a general increasing wrist extension angle trend was seen across the data. As the weight of the cylinder increased participants had to adopt a different strategy to perform each task. When the weight was small, it was easily supported using the flexor muscles of the wrist and hand. When the weight became larger than the flexor muscles could support, the subjects changed the position of the cylinder (changing wrist position to less wrist ulnar deviation and more extension) in space so the extra weight was supported by the palm and bones of the forearm.

As mentioned in Section 3.1.3, the intermediary and proximal joint data, along with metacarpal head data, can be disregarded during grip identification due to the comparative importance of the distal, thenar and hypothenar pressure components of the grips used by each subject. This practice is continued here. That study, including Table 3.4, shows a general increasing trend in detected pressure as the weight of the manipulated object increased. This was as expected. The method of summing the detected pressure for the reported sensors was used to make these comparisons. This summation has no real world analogue, but does allow for trends to be viewed. Care should be taken to only use this method to view overall cohort information. Table 3.6 reports the average pressure and standard deviation across the cohort. Variability between subjects in applied grip pressure, joint-angle, and wrist join deviation was seen amongst the data.

3.2 Wrist Velocity Classification for Human Intent Detection

In this paper we study means to improve interaction and safety between humans and co-robotic systems. To this end, wrist velocity profile data was gathered through a camera-based motion capture system and analyzed during activities of daily living. These actions were chosen to emulate motions which could be made during interaction with mobile manipulator or robotic end-effector, and included approaching, grasping, and moving a cylindrical object. Classification results of data collected during experimentation was compared to provide guidance for implementation on a real system. Wrist velocity data were collected during simulated activities of daily living, these data were classified using several classification methods found in the literature. We compared results obtained using a basic linear classifier, with excellent computational complexity, suited for real-time implementation, with those obtained using increasingly complex schemes. A linear classifier performed well when compared against more complex schemes and classifying the simplified gestures found in this data set. This insight has led the authors to consider non-linear classifiers when considering more complex gestures. This work will be used as a framework for more complex interaction systems and will provide guidance for future work. Validation of the approach occurred as well as implementation and testing on a real system, using off-the-shelf components and the Robot Operating System (ROS), tracking and classifying movements made by users.

This section is organized as follows: an overview and theoretical discussion of the various classification methods compared for further implementation can be found in Section 3.2.1. A description of the experiment whose data is used for classification and training is found in Section 3.2.2, with initial results found in Section 3.2.2.3. Implementation on a real system, and a validation experiment including results are described in Section 3.2.3. Discussion, concluding remarks and future work follow in Sections 4.3 and 3.4.

3.2.1 Classification Methods

Data were classified using multiple linear and non-linear classification techniques found in the literature. Background theory is presented below along with notation and definitions used throughout this work. Data were initially classified using a *linear classifier*. Next, variations of classifiers based on *least square minimization* techniques were applied to the data set. These more advanced methods included a *multi-layer perceptron*, *radial basis function*, *support vector machine*, and a *k-nearest neighbor* classifier.

In the training data $(\mathbf{x_p}, \mathbf{t_p})$, the p^{th} input vector $\mathbf{x_p}$ is of dimension N and the desired p^{th} output vector $\mathbf{t_p}$ has dimension M. Here $t_p(i) = \delta(i - i_c)$ where i_c denotes the correct class number. To include the bias, let the input vector be augmented by an extra element x_pN+1) = 1, so $\mathbf{x_p} = [x_p(1), x_p(2), \cdots, x_p(N+1)]^T$. The pattern number p varies from 1 to N_v. Computationally cumbersome, dependent features are a major bottleneck for a classification decision. Often the useful information lies in the lower dimensions of a high dimensional data. In the present work, we prune the features using OLS by transforming them into independent orthonormal basis functions thereby removing any feature that has a non zero projection in the orthonormal space. This technique helps us to uncover the lower dimensional manifold with far fewer number of features containing useful information. A more detail explanation of this particular feature pruning method can be found in[121].

3.2.1.1 Linear Classifier

Given the input training data, the weights **W** are connected from output to the input layer. We have a sigmoid activation function to the output layer. Therefore, the net function $\mathbf{n_p}$ for the output layer is

$$\mathbf{y_p} = \mathbf{f}(\mathbf{W} \cdot \mathbf{x_p}) \tag{3.1}$$

Here $f(.)$ is the sigmoidal activation function so that the desired output are constrained in the range [0,1]. We have taken mean square error (MSE) as the error criterion to train the classifiers as below:

$$E = \frac{1}{N_v} \sum_{p=1}^{N_v} \sum_{m=1}^{M} [t_p(m) - y_p(m)]^2 \tag{3.2}$$

Here $\mathbf{y_p}$ is the output of the classifier. As for the training algorithm, we use Hessian and gradient information for the weight changes to solve the following equation using the weight change as follows

$$\mathbf{W} \leftarrow (\mathbf{W} + \mathbf{e}) \tag{3.3}$$

Here **e** is a vector obtained after solving the following equation using the orthogonal least square method.

$$\mathbf{H_i} \cdot \mathbf{e} = \mathbf{g_i} \tag{3.4}$$

Here the Hessian matrix and the gradient vector are:

$$\begin{aligned} g_i(m) &= \frac{2}{N_v} \sum_{p=1}^{N_v} [t_p(i) - y_p(i)] y_p^{'}(i) x_p(m) \\ h_i(m,u) &= \frac{2}{N_v} \sum_{p=1}^{N_v} \frac{\partial y_p(i)}{\partial w(i,m)} \frac{\partial y_p(i)}{\partial w(i,u)} \end{aligned} \tag{3.5}$$

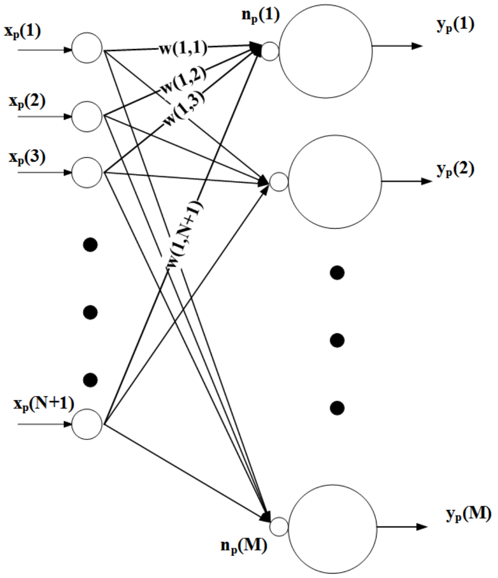

Figure 3.10: Linear Network Classifier

3.2.1.2 K-Nearest Neighbor Classifier

In a nearest neighbor classifier (NNC) [122], we have K_i example vectors from the i^{th} class. Letting $\mathbf{m_{ik}}$ denote the k^{th} example vector from the i^{th} class, where k is between 1 and K_i. We state $\mathbf{d}(\mathbf{x}, \mathbf{m_{ik}})$ as the distance between the input feature vector $\mathbf{x}$ to $\mathbf{m_{ik}}$. The squared distance (Euclidean) is

$$\mathbf{d}(\mathbf{x}, \mathbf{m_{ik}}) = \sum_{n=1}^{N} (\mathbf{x}(\mathbf{n}) - \mathbf{m_{ik}}(\mathbf{n}))^2 \tag{3.6}$$

The i^{th} class discriminant and estimated class are as

$$d_i(x) = min(d(\mathbf{x}, \mathbf{m_{ik}})) \tag{3.7}$$

for k ∈ $[1, K_i]$ and

$$i_c^{'}(x) = \underbrace{argmin}_{i}(\mathbf{d}(\mathbf{x}, \mathbf{m_{ik}})) \tag{3.8}$$

In the k-nearest neighbor classifier, we find the k closest example $\mathbf{m_{jm}}$. The class seen most in these k examples vectors is the class decision. Further explanation can be found in [122].

3.2.1.3 Multi-layer Perceptron

In a cascade connected Multi-layer perceptron (MLP) as shown in Figure 3.11. The input weights are $w(k, n)$, and connect the n^{th} input to the k^{th} hidden unit. The bypass weights $w_{oi}(m, n)$ connect the output to the inputs. Output weights, $w_{oh}(m, k)$, connect the k^{th} hidden unit's activation, $O_p(k)$, to the m^{th} output, $y_p(m)$. This output, $y_p(m)$, has a linear activation. The number of hidden units is denoted by, N_h. In order to handle the thresholds in the input and hidden layers, the input vectors and hidden unit outputs are augmented by an extra element $x_p(N + 1)$ and $O_p(N_h + 1)$ to be 1. The vector $\mathbf{n_p}$ is the hidden units activation and $\mathbf{O_p}$ is the hidden units outputs. Now $\mathbf{y_p}$ can be written as

$$\begin{aligned} \mathbf{y_p} = \mathbf{W_{oh}} \cdot \mathbf{O_p} \quad \textit{Here} \quad \mathbf{O_p} &= \mathbf{f}(\mathbf{n_p}) \\ \textit{and} \quad \mathbf{n_p} &= \mathbf{W} \cdot \mathbf{x_p} \end{aligned} \tag{3.9}$$

where $f(\cdot)$ is the sigmoidal activation function. In order to train an MLP, the mean squared reconstruction error must be minimized between the desired and the actual outputs. See equation 3.2.

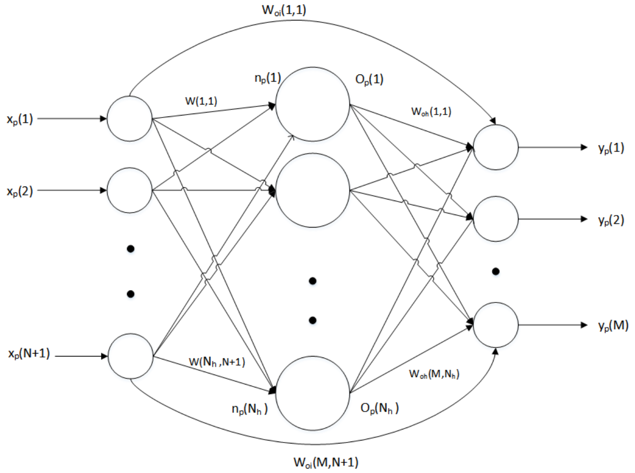

Figure 3.11: Fully Connected Multi-layer Perceptron

3.2.1.4 Radial Basis Function Network

We restrict ourselves to a three-layer cascade connected case for an RBF, without the loss of generality, with non-linear activation functions. The structure of the RBF is shown in Figure 3.12. The inputs are directly connected to a single hidden layer with N_h hidden nodes. It should be noted here that N_h is the determining factor not only computational complextity but also for the performance of the network. For the k^{th} hidden unit, m_k (k=1, $2 \ldots N_h$) denotes the mean vector of the k^{th} cluster. m_k is also known as the kernel vector or center vector.

Let the N-dimensional vector **c** store coefficients for the distance measure (DM). Let $\sigma(n)$ represent the standard deviation of input x(n). Then c(n) is initialized as:

$$c(n) = \frac{\sigma^2(n)}{\sum_{m=1}^{N} \frac{1}{\sigma^2(m)}} \tag{3.10}$$

For the p^{th} training pattern, the k^th hidden unit net function is:

$$net_p(k) = \sum_{n=1}^{N} c(n) \cdot (x_p(n) - m_k(n))^2 \tag{3.11}$$

Here, m_k (n) is the n^{th} element of $\mathbf{m_k}$ corresponding to the n^{th} input unit. In Figure 3.12, the dotted lines between input and hidden units signify that instead of weighted sum/Gaussian activations, each hidden unit output, $O_p(k)$, is obtained by calculating the *closeness* of the input $\mathbf{x_p}$ to $\mathbf{m_k}$ associated with the k^{th} hidden unit. In this case, the k^{th} hidden unit output $O_p(k)$ is calculated as a Gaussian basis function, for the p^{th} pattern:

$$O_p(k) = e^{-\beta(k) net_p(k)} \tag{3.12}$$

where $\beta(k)$ is the spread parameter defined as the inverse of the width of the k^{th} hidden unit Gaussian function with mean vector m_k. The mean vector m_k and spread parameter $\beta(k)$ are conventional function parameters of an RBF measured using equation 3.2.

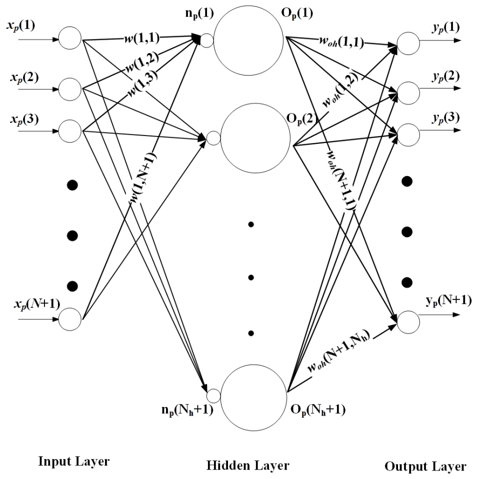

Figure 3.12: Cascade Connected Radial Basis Function Classifier

3.2.1.5 Support Vector Machine

The support vector machine is the most well-known kernel method for solving pattern recognition problems. For a binary classification problem, support vector machines have one output but two classes. The scalar output y_p is calculated as:

$$y_p = w^T \cdot X_p - b \tag{3.13}$$

the weight vector **w** is $N_s v$ by 1 and b is a bias. The basis vector X_p is N_{sv} by 1, and $1 \leq p \leq N_{sv}$. Assuming support vectors are made of the first N_{sv} patterns, X_P is then a support vector of dimension N_{sv}. The vector X_P is generated from the N by 1 input vector x_p as before in the MLP, but uses a differing activation function.

The support vectors are a subset of the basis vectors X_P for which y_p=t_p. A support vector machine's goal is to find a particular hyperplane a maximized margin of separation. The dual form for the constrained opimization of a support vector is Based on the

Karush-Kuhn-Tucker theorem[123]. Given the training data ($\mathbf{x_p}, \mathbf{t_p}$), p=1,2, $\cdots$, N_v, use the Lagrange multipliers α_p which maximize the output

$$y_p = \sum_{p=1}^{N_v} \sum_{k=1}^{N_v} \alpha_p \alpha_k t_p t_k K(x_p, x) \tag{3.14}$$

where K(x_p,x_k)=X_p(k) = exp($-\left\|x_p - x_k\right\|^2 / 2\sigma_k^2$) is the kernel function X_p(k) where m_k=x_k. C is a parameter that is positive and user-specified. Examples of types of support vector machines commonly found in the literature are polynomial learning machines and the radial-basis-function network.

3.2.2 Experiment and Data Collection

Initial experiments were conducted collecting human data during approach to grasp and manipulate cylindrical objects. Cylinder Lift, Push, and Pull manipulations were performed. Three tasks and three weights were manipulated by 10 human subjects. Results show that the profile of the velocity of the wrist during approach is different depending of the task. Wrist velocity data is classified using several techniques described in Section 3.2.1. An additional verification and validation experiment is described in Section 3.2.3, below.

3.2.2.1 Methods

This study builds on data collected during prior human-robot interaction studies [124], [125]. Ten volunteer subjects between the ages of 23 and 51 years of age used their dominant hands to interact with weighted cylinders as part of the initial data collection portion of this study. The average age was 30 years old. All subjects provided written consent upon explanation of the test procedure (UNTHSC IRB 2011-161).

Prior to starting data collection, instructions explaining the required tasks were given to the volunteer subjects. However, detailed hand or arm configurations to use during manipulation tasks were not given. The subjects performed the actions while manipulating a weighted cylinder. These actions included lifting a weighted cylinder off of a table top and pushing or pulling a weighted cylinder along the surface of the table. The volunteers were seated during all actions. For each of the pulling or pushing actions, the starting and ending positions were marked using cellophane tape on the table top. For all lifting actions, the subjects were given a starting position and instructed to lift the weighted cylinders to a "comfortable height". The volunteers were not instructed to complete any action within a certain time period and all returned to a "ready" position after completing each task. In depth explanation of experimental procedures, including detail about the performed tasks and weighted cylinders, can be found in previous works[124, 125].

3.2.2.2 Data Collection

Each of the volunteers were sensorized with a series of thirty-three retro-reflective markers. Twelve infrared cameras recorded motion of these markers in the experimental space. This data was collected at a rate of 120 Hz through Cortex software version 5.0.1.1496 (Motion Analysis Corp, Santa Rosa, CA). For this experiment, only the data collected for the volunteer's dominant hand's wrist velocity was used. Each of the weighted cylinders were sensorized using seven reflective markers placed at demonstrative locations on the surface. See Figure 3.13. Data was exported to Matlab for initial pot-analysis and then to a series of classification algorithms for further testing.

3.2.2.3 Classification Results

This section reports results of the linear classifier used to classify data collected during the experiment described in Sec. 3.2.2.2. This experiment gathered wrist-velocity data during simulated co-manipulation tasks between a human and a robotic manipulator. The subjects performed lifting, pushing, and pulling motions of a weighted cylinder.

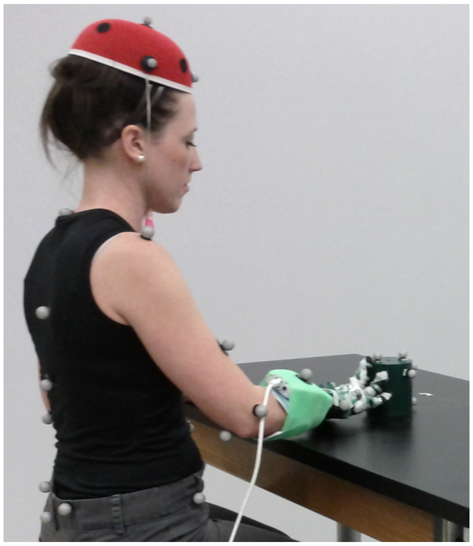

Figure 3.13: A subject wearing retro-reflective markers and interacting with a sensorized weighted cylinder during data collection

LC: Predicted class			
Actual class	Push	Pull	Lift
Push	27	2	4
Pull	2	31	1
Lift	0	2	31

Table 3.7: Confusion Matrix reporting classification and error rates for the linear classifier

K-NN: Predicted class			
Actual class	Push	Pull	Lift
Push	30	2	1
Pull	2	30	2
Lift	1	3	29

Table 3.8: Confusion Matrix reporting classification and error rates for the K-Nearest Neighbor classifier

MLP: Predicted class			
Actual class	Push	Pull	Lift
Push	28	2	3
Pull	2	31	1
Lift	0	2	31

Table 3.9: Confusion Matrix reporting classification and error rates for the multi-layer perceptron classifier

RBF: Predicted class			
Actual class	Push	Pull	Lift
Push	28	2	3
Pull	2	31	1
Lift	2	2	29

Table 3.10: Confusion Matrix reporting classification and error rates for the radial basis function classifier

Five different classification schemes were considered and compared as part of this study. These include both linear and non-linear classifiers. The methods compared are the *linear classifier*, *multi-layer perceptron*, *radial basis function*, *support vector machine*, and the *K-nearest neighbor classifier*. Results from each of these methods are presented here with further discussion following in Section 4.3.

Each of the five classifiers took a total of 100 patterns as input, with 33 patterns from the Push and Lift cohort movements and 34 from the Pull movements made by the

SVM: Predicted class			
Actual class	Push	Pull	Lift
Push	28	1	4
Pull	4	28	2
Lift	1	2	30

Table 3.11: Confusion Matrix reporting classification and error rates for the support vector machine

cohort. The *columns* of each table represent the predicted class, either Push, Pull, or Lift, by each classifier. The *rows* of each table represent the actual movement as performed by each subject. The intersection of each row and column represents the actual number of classified patterns and should not be read as a percentage. Mis-classifications occurred. The trace of the confusion matrices represent the probability of correct classification.

Table 3.7 reports the average performance data for a linear classifier when applied to this data set. The mis-classification error percentage for the linear classifier is 11.18%. Table 3.8 reports the performance data for a K-Nearest Neighbor classifier when applied to this data set. The mis-classification error percentage for the K-nearest neighbor classifier is 11%. Table 3.9 reports the performance data for a multi-layer perceptron when applied to this data set. The mis-classification error percentage for the multi-layer perceptron classifier is 10%. Table 3.10 reports the performance data for a radial basis function when applied to this data set. The mis-classification error percentage for the radial basis function classifier is 11%. Table 3.11 reports the performance data for a support vector machine when applied to this data set. The mis-classification error percentage for the support vector machine classifier is 14%.

3.2.3 Experimental Validation

In order to validate classifier performance for use in real systems, it was necessary to determine the minimum sampling rate required in order to obtain usable classification data. Experimental data was then gathered using a separate motion capture system, with configurable sampling rates, and an off-the-shelf depth camera system. This theoretical determination, and then experimental validation, gave insight in to minimum system requirements for future implementations of human-robot interaction systems. The aim of this validation work is to determine the necessary sampling rate needed in order to classify human-intent using a linear classifier. A linear classifier was chosen, owing to its ease of implementation and as a means to produce a base-line classification system for later comparison. Figure 3.14 provides a visual explanation of the data, classification and validation methods used in this work.

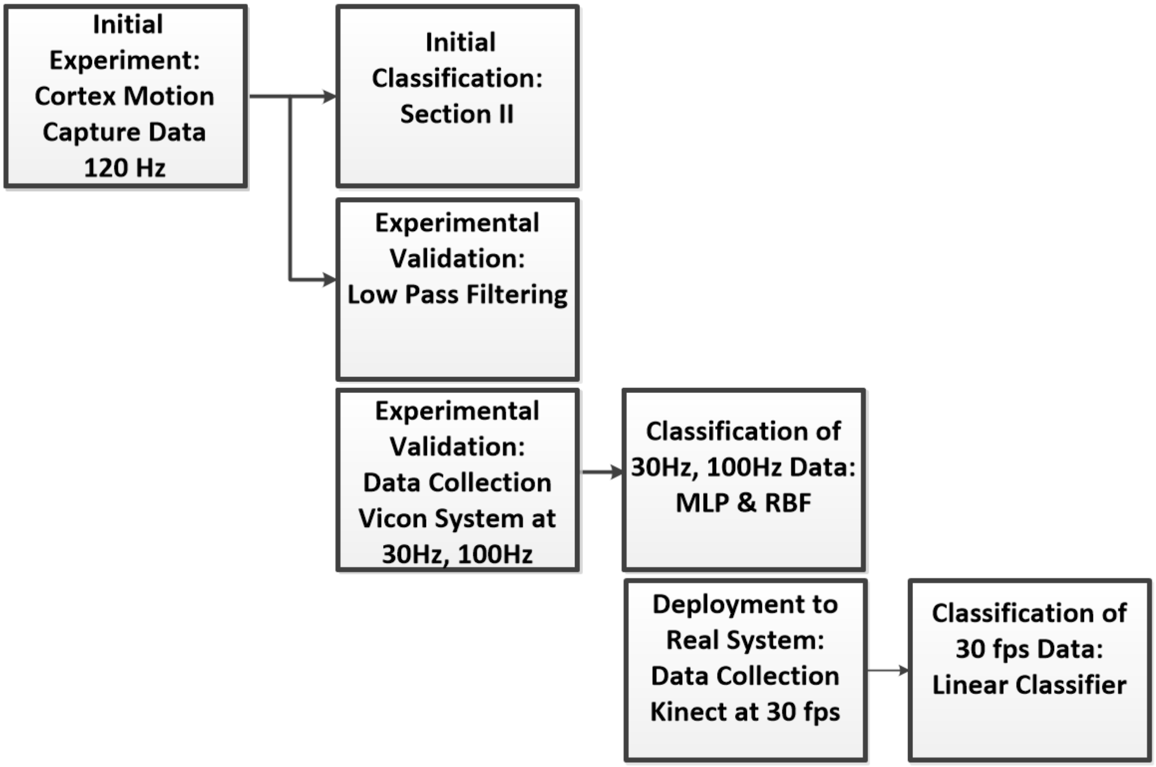

Figure 3.14: Visualization of data used in this work, including classification and validation methods, and samples rates.

3.2.3.1 Setup of Experiment Validation

An equiripple FIR low-pass filter with 15Hz cut-off frequency was applied to all data gathered during the initial clinical experiments. The proposed hypothesis, that a linear classifier trained using low-pass filtered data to remove information gathered at a higher sampling rate than 30Hz would not include relevant information for a linear classifier to perform adequately for a real system. This filtering was repeated for low-pass filters of

5Hz Cut-off, 30Hz, and 50Hz. In all, classifiers testing data filtered of frequencies above 10, 30, 60, and 100Hz occurred. Results of classification of data after low-pass filtering occurred are presented below in Section 3.2.3.2.

A Vicon motion capture system with 16 infrared cameras in a stacked square configuration, 8 cameras in a square stacked above another 8 camera square, was used. This system ran Vicon Tracker 3.2 software on a Windows 7, I5, 3.4GHz base-station. Push, pull, and lift motions were repeated, using a single weight and for 5 repetitions of each motion, similar to the manner described above in Section 3.2.2. Motions were repeated in order to gather data at 30Hz and also using a sampling rate of 100Hz. The subject and a weighted bottle were covered in four and three retro-reflective markers, respectively. Figure 3.15show the experimental setup using the Vicon system. A *multi-layer perceptron network* and *radial basis function classifier* were used to classify these data sets. The results of this validation experiment can be found in Section 3.2.3.2.

A linear classifier, as described in Section 3.2.1, was deployed to a real system and tested for use during a co-manipulation task. A single user performed push, pull, and lift tasks using a Microsoft Kinect RGB-depth camera[126] and weighted cylinder similar to that used in the clinical experimentation described previously. Custom classification software was created to interface with available ROS (Robot Operating System)[127] hand tracking

Figure 3.15: A subject wearing retro-reflective markers and interacting with a sensorized weighted cylinder during data collection

nodes. This software was deployed to and run on an Intel i7-4770 3.40GHz computer with 16GB of RAM, running the Ubuntu 12.04 LTS operating system and ROS Hydro software. Classification of motions occurred as the user manipulated a weighted cylinder and are presented in Section 3.2.3.2.

3.2.3.2 Results of Experimental Validation

A low-pass filter was applied to experimental data gathered in a clinical setting to determine minimum hardware sampling rates for human-intent classification. Further data was gathered in order to validate findings and deployment to a real system occurred.

Results of classification error of experimentally gathered data (Section 3.2.2) after low-pass filters have been applied at different cut-off frequencies is given below. A low-pass filter of 5Hz cut-off frequency produces error classification rates of 66.73%. Error rates of 33.37%, 28.48%, and 18.52% can be seen for data passed through low-pass filters of 15Hz, 30Hz, and 50Hz respectively. These error rates would coincide with frame capture or sample rates of 30Hz, 60Hz, and 100Hz of real or theoretical systems. It can be seen that error rates are reduced as the cut-off frequency increases.

Two classification methods were applied to data gathered during simulated co-manipulation tasks and motions found in daily living while using a motion capture system for data collection. A *multi-layer perceptron network* and *radial basis function classifier* were trained using methods previously described in Section 3.2.1. Data was gathered using the Vicon Motion Capture system and five subjects at 30Hz and 100Hz. A Kinect's best effort sampling rate is 30Hz and this capture rate was used as the determining factor for the lower sampling rate. Nine motions from each subject were classified and analyzed, three motions each of the push, pull, and lift actions, similar to those described above in Section 3.2.2. Initial analysis showed error classification rates of approximately 60% for both the *multi-layer perceptron network* and *radial basis function classifier* when applied to data gathered at 30Hz. No further analysis of this data was done at this time. Results of testing and classification of data gathered at 100Hz can be seen in Table 3.12 and 3.13.

MLP: Predicted class			
Actual class	Push	Pull	Lift
Push	28	2	3
Pull	3	29	2
Lift	0	2	31

Table 3.12: Confusion Matrix of Multi-layer Perceptron Classifier: Experimental Validation using Vicon System at 100Hz

RBF: Predicted class			
Actual class	Push	Pull	Lift
Push	28	3	3
Pull	2	30	3
Lift	1	2	28

Table 3.13: Confusion Matrix of Radial Basis Function Classifier: Experimental Validation using Vicon System at 100Hz

A linear classifier was deployed and used to classify user intent on a real system. A Microsoft Kinect was used to capture motion data and this data was then processed using custom software written for use in ROS. Results of a perceptual study showed approximately a 60% error rate, roughly two-thirds of all motions classified using the linear classifier were misclassified.

3.2.4 Discussion

Clinical data gathered from a cohort of ten subjects were used for initial classifier fitness evaluation. This data included velocity profile information for simplified motions found in activities of daily living as well as potential co-manipulation tasks in human-robot pairs. This particular experimental data set includes motion in only a single axis and the performance of the presented linear classifier suggests that the presented velocity profiles are essentially linear. It is assumed that as more complicated co-manipulation tasks are presented and attempted, non-linear classifier will be necessary, such as the presented radial basis function.

All weight matrices for classifiers made use of batch mode training prior to experimentation and analysis. The data was divided in to training and validation data sets, 70% for training and 15% each for testing and validation. This was repeated ten times. That is to say that data presented in Sections 3.2.2.3 and 3.2.3.2, the confusion matrices, were obtained using ten-fold validation. Future work will include unsupervised learning and adaptive control techniques in order that more complex tasks and gestures can be used by a user.

Except for the K-Nearest Neighbor classifier, all of the other classifiers use a validation dataset to tune the necessary hyper-parameters. Later once the hyper-parameters are known, the validation and training datasets are fused to perform testing. Since there are no class imbalances, we train by randomly providing patterns from each of the different classes as seen described by LeCun[128]. In order to test classifier baseline performance, we start by using a linear classifier due to ease of implementation and ease of use. Since the data is not entirely linear, we then open the problem to the non-linear classifier family with different degrees of results in different environmental and subject constraints. the multi-layer perceptron and radial basis function network are robust classifiers. All classifiers were custom designed and custom written to apply to this problem, and therefor tailored to suit its particular requirements. It is interesting to note that because the RBF uses an unsupervised clustering step, it has a relatively slower training time compared to the MLP. But, the RBF and MLP seem to perform equally as well as each other.

This work is meant to supplement other over-arcing goals within the field of human-robot interaction systems. Output from the classification systems described in this work are being considered for use as a human intent input to the control block diagram seen in Figure 3.16. Others have reported positive findings for intent detection during physical contact between a user and a sensorized robotic end effector[129] and [33]. Ge, *et al* describe a method to estimate the human user's intent based on the measured interaction forces provided between the user and the end effector, position of those forces and velocity at the interaction point. The adaptive impedance controllers described by Li provide estimates of the target impedance model for the intended motion. Both of these works require physical contact between the user and the end effector. The work described here is meant to precede physical contact and be used as an additional input to future control systems. An alternate approach to improving human action recognition made use of inertial sensors worn by the user[130]. Although hand gestures were not specifically tested, the described method shows promise. Chen, *et al* fused the two data types, depth and accelerometery, and made use of classification methods similar to those described above.

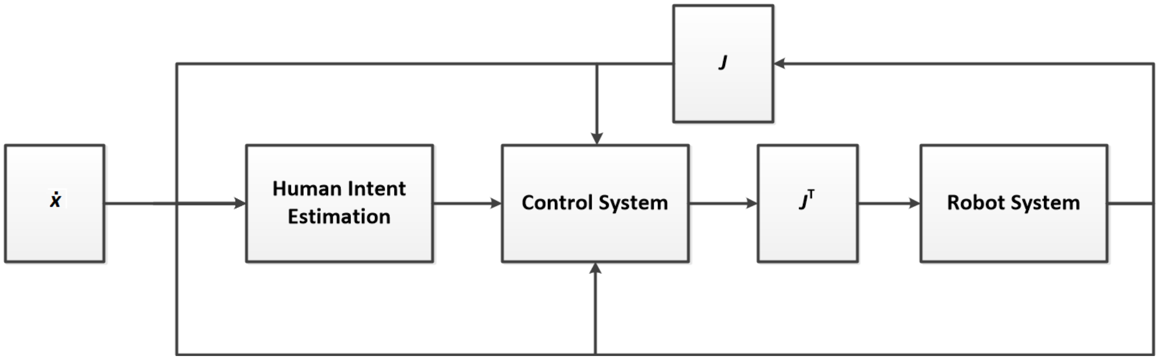

Figure 3.16: Proposed control system using Human Intent as an input. $\dot{x}$ is the input velocity of the human user's wrist or hand, J is the robot Jacobian

Validation was necessary to ensure that classification of intent using velocity profiles of a human hand during motions found in daily life is feasible. Highly accurate motion capture systems were able to classify human motion, in to one of three motions, with a high precision and making use of a linear classifier. Fast sampling rates, data sampled at 120Hz, in ideal conditions, favorable lighting, with low sampling noise, with a large subject pool, and a relatively large cache of training data, attributed to the high performance of this simplified method. Classification of each motion occurred off-line, after data had been gathered, and processed. Within the confines of this clinical experiment, it was shown that a linear classifier performed approximately as well as other, more advanced classification methods.

During cross validation, it was determined that sampling rates of approximately 100Hz would be necessary. In order to have enough data for use in the proposed methods, faster sampling rates are needed than are available in off the shelf RGB-depth camera systems. This is due to the relatively small difference in action as seen by each classifier, occurring only during the last moments of each motion and only lasting several hundredths-of-a-second. There are fewer informational features available on which to base a classification decision than is necessary. This hypothesis, that current hardware capturing at only 30 frames-per-second would have poor classification results, was tested in simulation, using a motion capture system with configurable sample rate, low noise, and using a real system. Additionally, the real system performed worse than expected, and it is thought that the processing cycles needed to perform the frame transformation calculations and other matrix algebra added computational burden. That is to say that on a non-real-time system, processing time is a very real performance concern to take in to account.

That data classified using higher frame-capture rates, data from the initial experiment (Section 3.2.2) and data gathered using the Vicon system, at 120Hz and 100hz produced acceptable results. This is despite differences in the training data frame rate (120Hz) and the testing data frame rate (100Hz) and shows the robustness of this technique. This leads us to believe that it will be possible to use these methods for human-robot interaction tasks, if limited to a particular physical location. Interaction in a more mobile or portable environment is not possible using this method at this time.

Future work will require the need for complex and continuous gesture recognition, including determination of actions or non-actions, ie “not a gesture”, as well as a robust online classifier. Although the results from deployment to a real system were poorer than hoped, the framework developed for proof of concept testing with the linear classifier, depth camera system, and ROS will be instrumental in future human-robot interaction systems within our lab.

3.3 Pressure Sensors

Guidance regarding performance parameters of pressure sensitive robotic skin was taken from experimental results described in Sections 3.1.3 and 3.1.4. Size and layout of the sensorized area were determined in order to provide adequate pressure resolution based on the preferred grip strategies of the clinical cohort. That is to say that maximum and minimum pressure limits, as well as minimum sensor radius and distance, were designed to allow a user to interact with a device but were not designed to perform beyond human capabilities.

3.3.1 EHD Printed Senors

Several printable inks were characterized in search of suitable composition and output characteristics. Ink can be deposited directly on to Kapton film, a flexible substrate, for testing. However, through experimentation, it was found that patterning features on to a substrate layer of Chromium and Gold allows for improved functionality. These layers are on the order of approximately 300nm on top of a Kapton layer approximately 100μm thick. Three different inks were tested using the robotic printing system and the ink material weight ratios are described below in Table 3.14. An array of sensors were produced as a means to study physical human-robot interaction. This array was produced using the EHD Printing Method (ElectroHydroDynamic) and making use of PEDOT:PSS inks. EHD printing makes use of a technique to directly deposit piezo-resistive material directly on a substrate utilizing a high-speed, high-precision three degree of freedom print-head.

A number of inks were produced and characterized, making use of PEDOT:PSS inks and their inherent piezo-resistive properties. In order to tailor sensor response with printability using the EHD process, optimizing the ink characteristics was necessary. PEDOT:PSS paste was dissolved in NMP, N-Methyl-2-Pyrrolidone to obtain the desired low viscosity and low surface tension of the ink to allow for printing. A table showing the three most promising ink mixtures is shown in 3.14.

Table 3.14: PEDOT:PSS inks tested for EHD Printing Process

Ink #	PEDOT:PSS 5% SPI	PVP (29K MW)	NMP	Nafion
1	10g	NA	20g	NA
2	10g	0.625g	20g	NA
3	10g	0.625g	20g	5g

Inks were prepared and tested by Next Generation Systems Group, University of Texas - Arlington students and University of Texas - Arlington Research Institute (UTARI) staff. EHD printing was completed at UTARI using a custom configured robotic dispensing system. A series of controllable stages allow for a printing nozzle to be positioned above a substrate. This printing process is automated, making use of the mask layout of the sensor array and a microscope camera. Calibration and performance of this system can be found in [2]

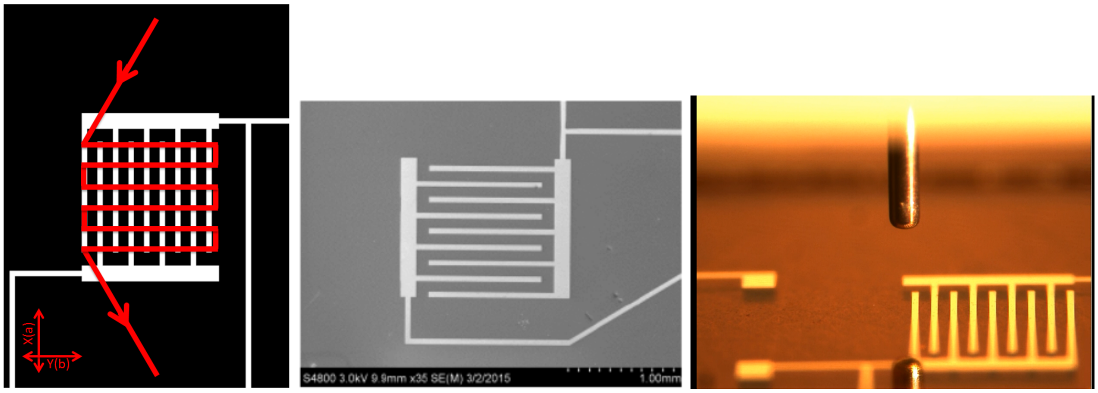

(a) (b) (c)

Figure 3.17: The print path of a single EHD Printed sensor b) View of single sensor through electron microscope c) Aligned print nozzle and sensor above substrate. Images courtesy of [1, 2]

3.3.2 EHD Senor Array

A series of proof-of-concept designs were completed and iterative changes resulted in completion of a 4x4 sensor array, including 16 taxels. Figure 3.17(a) illustrates printing path of a single sensor within the sensor array and 3.17(b) shows an electron micrograph of a single interdigitated sensor. Figure 3.17(c) shows an alternate view of an individual sensor, from the microscope camera, and also shows the EHD printer's dispensing needle. The sensor and print nozzle are aligned in this figure. Current arrays make use of a zero-insertion-force connector (ZIF) to connect to supporting electronics. While allowing for quick exchange of arrays, are cost effective, and provide a simple interface, further iterations will address inherent sizing limitations for large arrays. These connection traces can be seen in Figure 3.18.

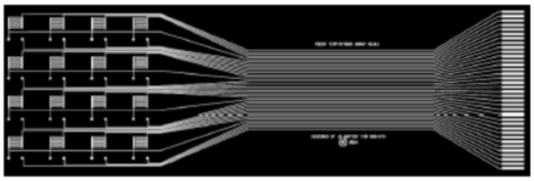

Figure 3.18: Array of Sensors. ZIF Connections can be seen on the right of the figure. Image courtesy of [2]

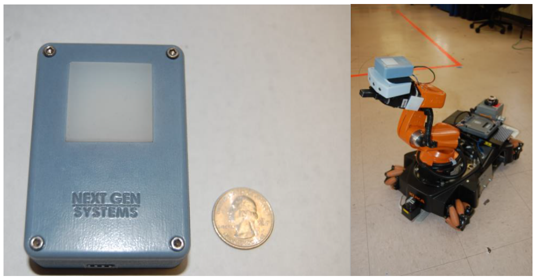

Figure 3.19: a) Single packaged sensor b) Single sensor mounted on KUKA youBOT mobile manipulator. Images courtesy of [1, 2]

Proof of principle devices have been created in order to test the supporting electronics and available interaction modalities. Figure 3.19 shows a single sensor, within in a protective housing, mounted on a Kuka youBOT robotic manipulator. This device allows a user to interact directly with the youBOT via touch.

3.3.3 EHD Printing: Proposed Tasks

An array including sensors beyond the 4x4 design is under completion. The array of sensors is currently being designed to allow for coverage of a “sensorized can”, see Figure 3.20. The sensors currently in use by ThruMode Matrix Arrays [131] are allowing for experiments to begin and testing of supporting electronics. Goals include replacing this array with one made and designed using specifications gained through study of results from previous experiments.

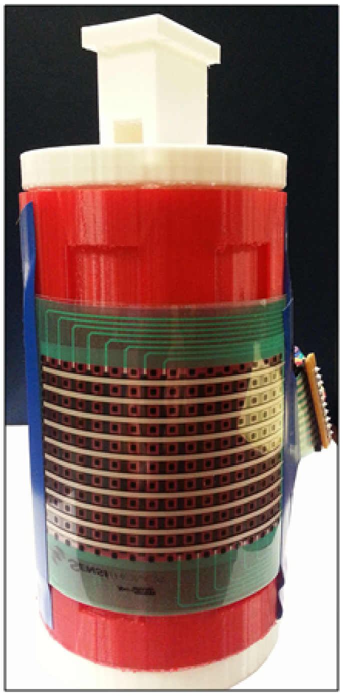

Figure 3.20: Array of sensors mounted to object for use in pHRI experimentation and usage studies. Image courtesy of [1]

Sensors are currently printed on substrate. Individual sensors are inter-connected via patterned traces and fabricated using standard lithographic processes. Research is continuing with an eventual goal to create a completely ”mask-less” production process including EHD printed sensors on top of printed traces on a flexible substrate. Creation and characterization of metallic, printable inks will need to be completed. Experiments regarding maximum deflection of the flexible substrate will also occur. The maximum curvature that the substrate can undergo, with printed sensors, and the sensors still return a viable signal is not known at this time. Experiments are planned to learn these performance limits.

3.4 Conclusions

The reported clinical studies aimed to understand human interaction with objects found in daily life. A total of 10 subjects interacted with a weighted door and weighted cylinder using their dominant hands. Amongst the subjects, three main grip types were identified; those using mostly the fingertips, those using mostly the palm and those using a combination of both the palm and hand. Maximum interaction pressures occurred at either the finger tips (Distal joints) or the palmar area (Thenar or Hypothenar) and not at the Proximal or Intermediary joints. Grip pressure and joint-angle data were collected. During interaction experiments with a weighted cylinder, maximum and average interaction pressures, as well as average joint-angles during maximum applied pressure, were determined. Through experimental design, grasping strategies for objects included palm and fingertip only grips. Generally, palm grips had higher joint angle values, while higher weight required more support from the bones of the palm and forearm necessitating users to adjust wrist angles. Additionally, manipulating a 10 lb. weight was close to the lifting limit of some subjects.

This information provided valuable insight regarding the pressures and pattern of interaction of the human hand with a simulated robot arm. This data also provided guidance to assist with production and design of EHD printed sensor arrays and verifying and updating human intent models through the use of novel applications of classification algorithms. Future research is under way to improve sensor fabrication processes. A continuing goal is to fabricate a completely “mask-less” array including EHD printed sensors on top of printed traces on a flexible substrate. Creation and characterization of metallic, printable inks will need to be completed.

The proof of concept system described in Section 3.2 will allow improved co-manipulation tasks between a user and a robotic manipulator system through improved user intent-detection prior to contact between the user and the manipulator. Current motions are limited to a single axis, in the x-plane. Training of classifiers occurred using data gathered from clinical experimentation and a cohort of subjects performing motions-of-daily-living. The nearly linear motions used in this experiment were chosen as a means for initial study of various classification methods and it was shown that a linear classifier performed as well, if not better than, several non-linear classification methods found in the literature. Further simulation and testing verified the need for increased frame-rate-capture over and above off the shelf depth cameras. Three classifiers, a linear classifier, a multi-layer perceptron and a radial basis function classifier were deployed for further study, experimentation, and validation. The radial basis function was chosen due to its known strengths in function approximation of non-linear systems, as a consideration for future work. It was shown that for the motions chosen for further study classification in this work, the “push”, “pull”, and “lift” motions, that the multi-layer perceptron and radial basis function methods produced acceptable results. When deploying a linear classifier for use in a real system with an RGB-depth camera, classification performance results were as expected when considering simulation and study. Future systems, and those involved in practical systems for use beyond the laboratory, will require free motions in three dimensions and most likely require pairing with a physical-human robot interaction system. Depth cameras with frame rates approaching 100Hz will be needed. Systems with lower sampling rates give a major performance hit and are a bottleneck for implementation in practical mobile systems. These results will guide future implementations, control systems, and human intent detectors involving interactions between a mobile manipulator and human user.

CHAPTER 4

EMG and EMG-FREE Control of a Powered Prosthetic Device

The objective of this chapter is to present work regarding a novel combination of sensors, prosthetic socket, and control algorithm for use as a physical human-machine interface. This system, for use by powered prosthetic users with limited dexterity are able to control a system with additional inputs and added robustness to mitigate poor performance. The system gains are automatically adjusted throughout the day to improve functionality loss due to user fatigue.

This chapter is organized as follows: Section 4.1 describes a study investigating the feasibility of using Force Myography as an additional input to a powered prosthetic device along with SEMG. Then Section 4.4 reports a proof of concept extension, allowing Force Myography as the driving signal in grip choice during use of a robotic hand. Section 4.2 outlines experiments which expand work done using SEMG and FMG. Finally, Section 4.5 summarizes results and offers concluding thoughts.

4.1 Multimodal Sensor Inputs for Physical Human-Machine Interface

A study was conducted to investigate heterogeneous sensor arrays for use in pHRI and its applications to control of a powered prosthetic device. Force Myography (FMG) and more traditional surface electromyography (sEMG) were chosen for inputs and in combination with a neural network, were able to detect socket shift as would be seen during regular use by a trans-radial amputee.

4.1.1 Subjects

A right hand dominant, 34 year old male subject was recruited during this proof of concept experiment. The subject provided written consent to testing after being informed of the testing procedure. The test procedure was approved by the local ethics review committee through National Science Foundation NRI Grant #IIS-1208623.

4.1.2 Experimental Protocol

During the initial experimentation, a single surface electromyography sensor (SEMG) was attached to a healthy-limbed subject's dominant side forearm in such a way as to isolate activity of the subject's extensor carpi ulnaris. A piezo-electric force sensor was attached directly above, and in contact with, the SEMG sensor housing. Please see Figure 4.1. This sensor placement is referred to as the "ideal position". The subject was seated comfortably in a chair with their arm resting on the chair's arm rest during experimentation. The subject was instructed to extend their wrist five times, returning to a neutral position after each motion. Following these initial motions, the SEMG-force sensor housing was moved away from the "ideal position".

The sensor housing was moved to simulate the shifting of a prosthetic socket as experienced by a user during daily life and as a way to simulate muscle fatigue. During this experiment, the sensor housing was moved into four alternate positions, offset from the initial, ideal position, by 1 cm. The four locations are referred to here as "lateral", rotated towards the thumb, "medial", rotated towards the pinky or small finger, "proximal", shifted towards the elbow, and "distal", shifted towards the user's hand. The experiments were repeated, moving the sensors and sensor housing 2 cm from the "ideal position". Extension motions were repeated five times, as described above, in each of the offset positions. Data and further discussion of the results are presented below in the 4.2.3 and 4.3 sections, respectively. Data collection methods and descriptions of materials are presented in the 4.4.5 section below.

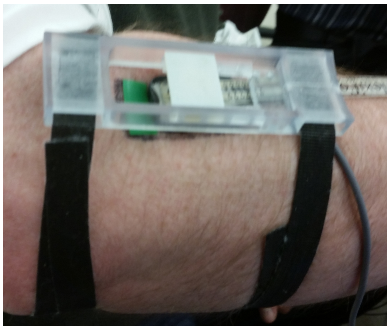

Figure 4.1: Subject wearing SEMG and pressure sensor housing on the anterior side of their dominant forearm

4.1.3 Intra-socket Pressure Measurement

The extensor carpi ulnaris muscle belly of the forearm was identified on the subject, located on the posterior of the subject's dominant forearm. SEMG sensors were placed in optimal locations on the subject's forearm for signal detection. These points were marked and custom designed sensor housings were created, as seen in Figure 4.1. These housings secured piezo-resistive force sensors, for interaction detection, above the SEMG sensors. As the subject extended their hand, the wrist extensor muscles changed in volume. This volume change was detected as a force applied to the inside of the sensor housing and was detected by the piezo-resistive force sensor. Further discussion of the sensors, and data acquisition, is discussed in the section labeled *Data Acquisition*.

4.1.4 Data Acquisition

Surface EMG data was collected at 1200 Hz using a Bagnoli 16 EMG DS-160 system by Delsys and a National Instruments USB 6218 DAQ connected to a Dell Precision t5600 Microsoft Windows 7 64-bit 2.0 GHz computer. Cortex software v5.3.2.1545 (Motion

Analysis Corp, Santa Rosa, CA) running on this machine processed the data and output time-series data in CSV format. A single Delsys wired-SEMG sensor was used in initial experimentation. An ultrathin FlexiForce ® A201 model piezo-resistor (thickness - 0.208 mm; active sensing area 0.713cm^2; force sensitivity range 20g - 2200kg; response time 5-20μ sec; linearity - $< \pm 5$ %) [30] was used to detect intra-socket pressure. A voltage divider circuit was created, incorporating the Flexiforce sensor, and the output of this circuit was read into a National Instruments myRIO device which performed data acquisition at 100 Hz. A custom VI program was created and run concurrently on the myRIO device and a connected Acer 2.5 GHz laptop running Windows 8.1 software and National Instruments LabVIEW 2014. This VI saved the recorded pressure data, output as a voltage difference, to a CSV formatted file for offline data processing.

4.1.5 Correlation Analysis

Signal correlation analysis between the SEMG and pressure signals were conducted using the in-built Matlab function, “corr”. This function calculates the linear correlation coefficient. Correlation calculation was conducted using the data from the“ideal” SEMG and pressure sensor location, saved as two vectors of time-series data. Correlation analysis was conducted for all SEMG and pressure signal pairs and a negative correlation was expected.

4.1.6 Classification

Data was classified using a multi-layer perceptron (MLP) as designed in the Neural-Network Toolbox available in Matlab. MLP inputs included SEMG data parameters introduced by Hudgins, *et., al* along-side the readings from the piezo-electric pressure sensor [132]. Namely, these included the moving average of the absolute value of the SEMG signal or mean absolute value, the derivative of the absolute value of the SEMG data or the slope, and the absolute value of the pressure data. The vector of SEMG data is denoted s(t) and the vector of pressure data is denoted p(t) in the formulas below. The moving average of the absolute value of the SEMG signal is called CMA. The Moving Average window size is denoted, ω_1, and a *central moving average* calculation was performed. During calculation, a difference over a window of size ω_2 (seen in Equation 4.5 was used in place of the derivative of the absolute value of the SEMG data. The moving difference window Training occurred using 70% of the sampled data with validation and testing split evenly amongst the remaining 30%.

$$\hat{s}_t = |s_t| \tag{4.1}$$

$$CMA_{\hat{s}_t} = \frac{1}{\omega_1}\hat{s}_{(t-\omega_1)} + \frac{1}{\omega_1}\hat{s}_{(t-\omega_1-1)} + \frac{1}{\omega_1}\hat{s}_{(t-\omega_1-2)} + \ldots + \frac{1}{\omega_1}\hat{s}_{(t)} + \tag{4.2}$$

$$+ \ldots + \frac{1}{\omega_1}\hat{s}_{(t+\omega_1-2)} + \frac{1}{\omega_1}\hat{s}_{(t+\omega_1-1)} + \frac{1}{\omega_1}\hat{s}_{(t+\omega_1)} \tag{4.3}$$

$$\mu_1 = CMA_{\hat{s}_t} \tag{4.4}$$

$$diff(CMA_{\hat{s}_t}) = CMA_{\hat{s}_t} - CMA_{\hat{s}_{(t-\omega_2)}} \tag{4.5}$$

$$\mu_2 = diff(CMA_{\hat{s}_t}) \tag{4.6}$$

$$\hat{p}_t = |p_t| \tag{4.7}$$

$$\mu_3 = \hat{p}_t \tag{4.8}$$

Algorithmically, signals were to be classified when the moving average of the SEMG data was above signal noise and beneath a certain threshold, the slope over a defined window was positive, and the pressure data was below a certain threshold. A hidden layer size of four neurons was used for training. Data was input to the Neural Network Toolbox and training occurred ten times with no significant improvement in the resulting network. Weights and bias values were updated using the *scaled conjugate gradient* method. Further discussion of these thresholds and the performance of the trained network can be found below. Figure 4.2 illustrates the signal classifier.

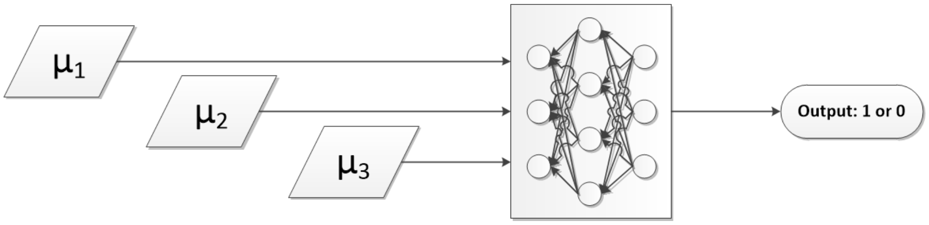

Figure 4.2: Signal flow chart illustrating data input vs output of the signal classifier. Inputs include Mean Absolute Value of SEMG, derivative of the Mean Absolute Value, and Absolute Value of the Pressure data.

4.1.7 Results

EMG and pressure data were collected during experimentation. Surface EMG data was sampled at 1200 Hz using the Delsys data acquisition hardware and software described above. Pressure data, from the piezo-resistive sensor, was collected as a reading of voltage change during sampling. That is to say, as pressure increased on the pressure sensor, resistance in the circuit increased and voltage decreased. This drop in voltage can be seen in Figure 4.3(a). Pressure data was sampled at 100 Hz.

Output of the actions occurring during the “ideal”, “1cm medially displaced”, and “2cm medially displaced” of the sensor housing can be seen in Figures 4.3(a) and 4.3(b). Magnitude data for the “ideal” sensor position can be seen in Figure 4.3(c).

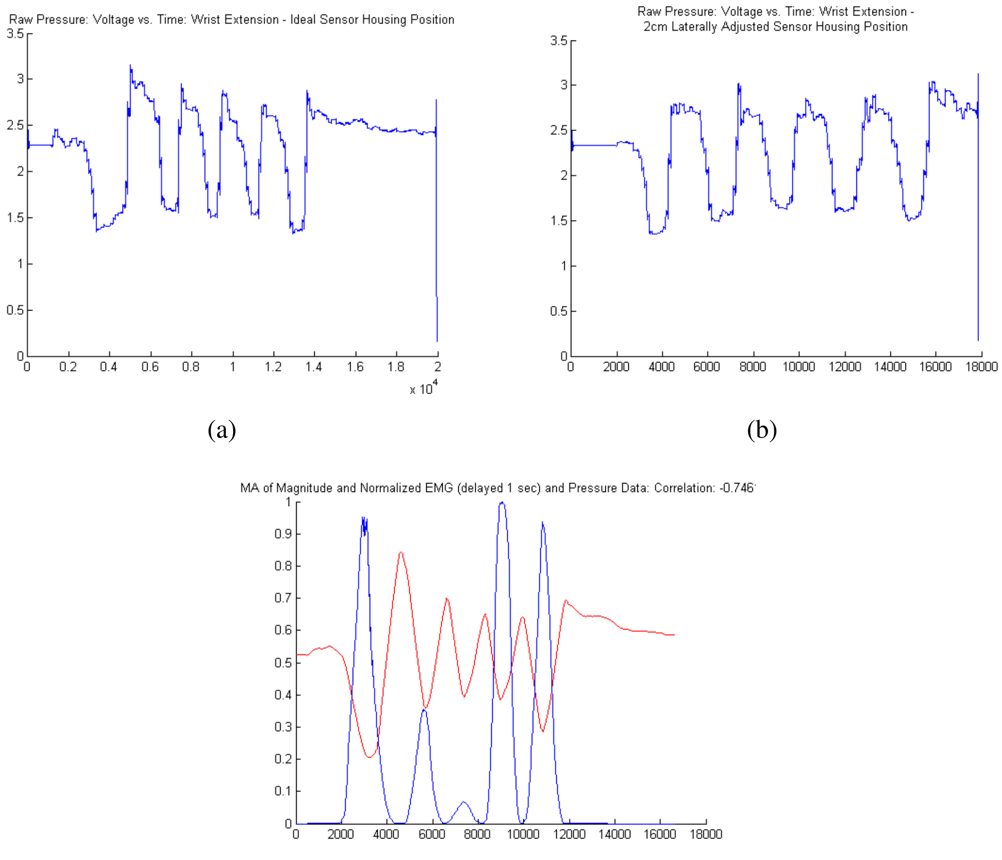

(a)

(b)

(c)

Figure 4.3: Pressure Data as collected with the SEMG and piezo-resistive sensor housing in the Ideal, (a) and 2cm Medially Displaced Positions. (b) Voltage vs. Time. A voltage drop indicates force being applied to the pressure sensor. (c) Normalized Magnitude SEMG (blue line) and Pressure Data (red line)

4.1.8 Correlation Analysis

A fourth order Butterworth filter was designed and applied to the SEMG data with frequency ranges between 10 and 500Hz. Then, for ease with initial time-domain analysis, pressure data was up-sampled to 1.2 kHz. Resampling in this way allowed for correlation using statistical analysis techniques. Data was input in to the “corr()” function, from the Matlab 2013a Statistical Analysis Toolbox, in vector form. Differences in vector lengths between SEMG and pressure data required post-pending empty rows to the EMG data.

Analysis required that correlated signals be of equal lengths. This resulted in the flatline at zero, at the end of the SEMG data, seen in the figures reporting on the post-processed data above. A negative correlation between SEMG and pressure data was expected. Data collected during the experiment at the initial, ideal position, was found to have a correlation coefficient of approximately -0.74, a moderate negative correlation. Data for the "1cm Medial" and "2cm Medial" displacements are reported as -0.78 and -0.47, respectively. This drop in correlation value as distance is increased from the ideal position was expected. The further from the "ideal" sensor location, the lower the SEMG signal's amplitude would be. But, the pressure sensor's readings should have stayed roughly equivalent.

It should be noted that during experimentation, the systems in use required manually starting recording of the SEMG and pressure data. While both systems recorded data concurrently, the beginning of the recording for each signal was at a slightly different time. It was initially thought that this inherent delay would affect performance. This is the reason the correlation coefficient was calculated. It was found that manually delaying the SEMG, by pre-pending data of zero magnitude, did not significantly affect the correlation coefficient. This means that the signals are still correlated and can be used to train a neural network. The start and stop of the signals relative to each other would still affect the training algorithm, however. Correlation did improve as the moving average window used to smooth the SEMG data was increased and got worse as the amplitude of the SEMG signal decreased with distance from the "ideal" location. A moving average window of 256ms was used after empirically studying the effect of the window size on the SEMG short term signal fidelity as it related to the correlation coefficient. This relatively short moving average window has also been used in [78].

4.1.9 Neural Network

An MLP of hidden layer size four was used to train and then test collected data. Figures 4.4(a) - 4.4(c) show representative outputs from a trained MLP network, ie. data from the "ideal" and "1cm medially displaced" and "2cm medially displaced" extension actions. Output from the network, in black, represents a correctly detected, degraded signal. Time is seen on the x-axis, reported in milliseconds. Root Mean Square Error (RMSE) for this network is reported as 0.021 at epoch 64.

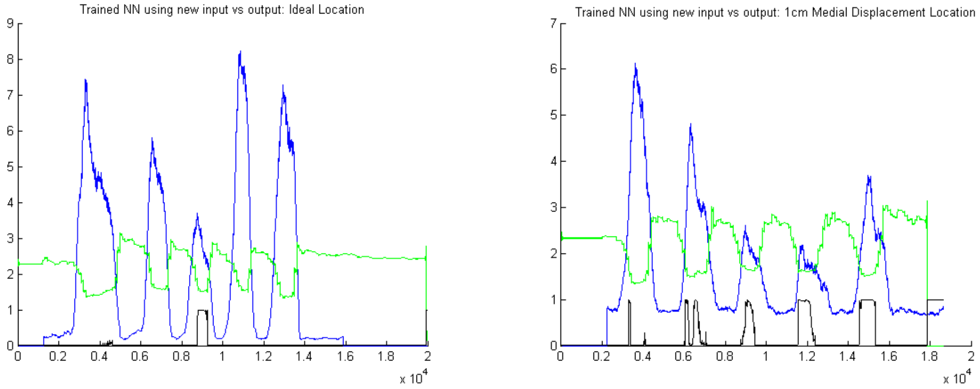

(a) Ideal location

(b) 1cm Lateral Displacement

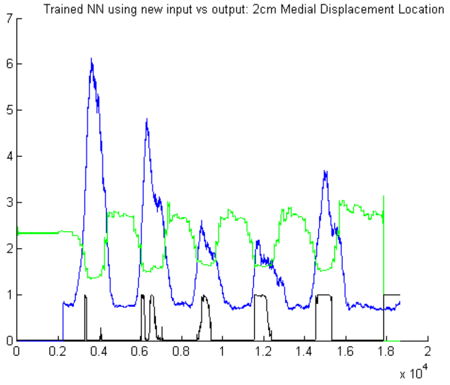

(c) 2cm Lateral Displacement

Figure 4.4: Output vs Input of the Trained networks. A magnitude rectified, Moving Average of the EMG data is seen in *'blue'*. Pressure data, as a voltage output, is in *'green'*. Output of the MLP network is in *'black'*. The MLP was trained using the data from c)

4.1.10 Discussion

A healthy-limbed subject, with limited SEMG controlled prosthetic device experience, was used during this proof of concept experiment. This relative inexperience may have resulted in the varied SEMG signal magnitude during testing. Also, due to limited testing time, focus was paid to signal degradation identification due to SEMG displacement issues. It is hypothesized that similar techniques can be used for signal degradation identification, due to user fatigue, in future work. Normalized data was not used during training of the neural network as one of the desired outcomes of the system was to determine when SEMG data decreased in signal strength or was otherwise degraded. However, scaling of the SEMG data did occur. Accuracy of the trained network improved when all signals were of the same order of magnitude. Therefor, SEMG signal magnitude was reduced by an order of three, divided by 1000, prior to input to the MLP. Similar calculations occurred for the slope data. Hudgins' previously mentioned work suggested the use of four patterns to represent the myoelectric signal; mean absolute value, mean absolute value slope, zero crossings, and slope sign changes [132]. Only two of these, mean absolute value, or moving average, and mean absolute value slope, were used as inputs to the MLP. Sufficiently successful classification occurred but further improvement may be possible by including these additional parameters. Positive slope values were chosen for inclusion as it was thought it more desirable to classify a leading edge of a potential signal rather than a falling edge. That is to say, a potentially degraded signal should be detected as a user increases muscle output rather than as the muscle is relaxed. The lower threshold above noise of "50" and upper threshold values of "4000" for SEMG and "2" for pressure data were chosen empirically. These thresholds will need to be tuned to an individual user as SEMG magnitude and deflection forces will vary from user to user.

Significant overshoot and hysteresis of the piezo-electric sensor occurred during the relaxation phase of the subject's motions. Future work should take these effects in to account during sensor selection as sensor drift was seen towards the end of experimentation.

An MLP with hidden-layer of size four, four hidden-layer neurons, was chosen. Initial testing of the trained networks began with hidden-layers of size three, progressing incrementally to networks with hidden-layers of size 10. Additional testing occurred at networks including 25, 50 and 100 hidden-layer neurons. No significant improvement was seen past a hidden-layer consisting of four neurons. Training of the network occurred using the data acquired during actions detected by the sensors displaced medially by 2cm from the ideal location. This particular training set included both "positive" and "negative" training examples whereas the "ideal" case only included data exceeding the SEMG amplitude threshold. Classification of data from the displaced sensors did occur and was considered successful. Future experiments will need to include more than five flexion or extension actions in order to ensure sufficient training examples are available.

Dynamic Time Warping (DTW) analysis, a method of correlating two normalized, periodic signals, was also conducted. DTW has been used in the past to measure similarity of temporal signals.[23] Analysis was carried out using an "inverted" pressure signal in order to overcome the negative correlation of the two signals. This method was eventually abandoned because the pressure and EMG data, while temporal signals, were sufficiently a-periodic to cause an unacceptably large DTW correlation coefficient. That is to say that the calculated normalized moving-mean of the SEMG data and the normalized pressure data's maximum and minimum values were incorrectly correlated using the DTW algorithm. It is thought that this occurred because of the relatively high variation of the SEMG signal within small time steps. Sufficiently smoothing the SEMG data for DTW analysis caused loss of information relative to the pressure signal.

Fougner's multi-modal SEMG and intra-socket force measurements focused on improving device controlability through the cancellation of induced signals due to external forces acting on a prosthetic socket. These forces could be from a user interacting with objects throughout their daily lives [79]. Consideration is not taken as to signal degradation due to fatigue or sensor movement. A combination of the two systems may offer further improvements to controllability of a prosthetic device. Manual recalibration of SEMG driven prosthetic systems is still required at this time. It is thought that notification of degraded signal quality will improve function, and reduce user frustration.

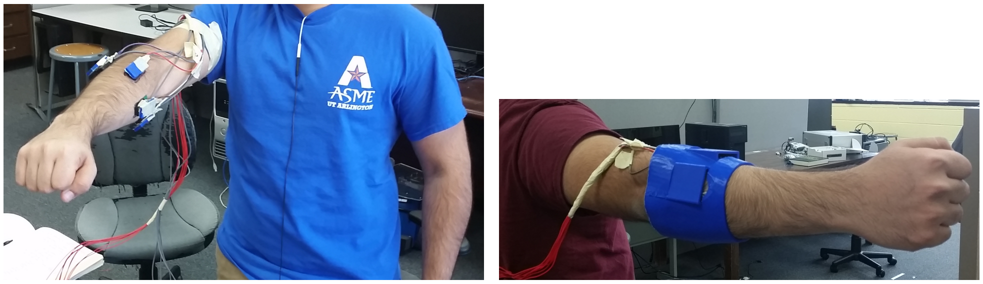
(a)

(b)

Figure 4.5: a) Subject wearing SEMG and FMG collocated sensors b) Subject wearing simulated prosthetic socket and collocated sensors

4.2 Heterogeneous Sensor Array for Control of Prosthetic Device

This section details expanded studies of SEMG and FMG data fusion described in Section 4.1. A simplified multilayer perceptron feedforward neural network was utilized to classify data gathered during experimentation with four SEMG and four FMG collocated sensors as a user performs flexion and extension motions of their dominant wrist. Results show that classification results can be improved by at least 3% for most cases, 8% when classifying radial and ulnar deviation, and 35% when a socket is shifted due to normal activities of daily living.

4.2.1 Methods

Flexion and extension actions were made by a subject and data was recorded via SEMG sensors, FMG sensors, and custom data acquisition hardware. Placement of the SEMG sensors in “ideal” locations on the flexor and extensor muscle bodies was determined by a physical therapist in order to achieve high quality EMG data. The socket and SEMG-FMG sensor pair was then manually moved to “non-ideal” locations 1cm and 2cm away from the previously determined “ideal” location as measured along the surface of the subject’s skin in each of the four cardinal directions. The flexion and extension movements were then repeated, data was collected, and a signal classification schema built. Results and discussion of the classification of this data are seen below.

4.2.1.1 Experimental Protocol

Experimental data from a single right hand dominant, healthy-limbed twenty-four year old male subject is reported. The subject was informed of the test procedures, which were approved by the local ethics review committee (UNTHSC IRB 2011-161), and written consent was given by the test subject. The sensor housing was specifically fabricated for the individual subject using 3D scanning of their forearm and 3D printing.

A series of four movements and arm configurations were utilized to gather data used during this experiment. These movements included flexion and extension of the wrist with the sensors in both “ideal” and “non-ideal” locations relative to the muscle bodies, as the subject’s arm was held in different arm positions found during activities of daily living, and while the subject’s arm was fatigued. Radial and ulnar deviation data was also collected as the sensors were in an “ideal location” as determined by a physical therapist. Four SEMG sensors were attached to the subject’s dominant forearm in order to isolate activity of the subject’s flexor and extensor carpi radialis and ulnaris muscles in order to gather this data.

Four sensor housings containing a piezo-electric force sensor in contact with the surface of the SEMG sensor were contained within a simulated socket described below in Sections 4.2.2.1 and 4.2.2.2. The sensor placement referenced here as the "ideal position" can be seen in Figures 4.5(a) and 4.5(b). All SEMG sensors were initially aligned to the muscle body during initial placement.

4.2.1.2 Simulating socket shift

The first data set gathered was meant to test the effects of socket shift on classifier performance. The subject sat in a chair and rested their dominant arm on the chair's arm rest in a comfortable position. The subject extended their wrist at least 10 times and returned to a neutral, resting position after each hand motion. Next, the subject was instructed to flex their wrist at least 10 times, returning to a neutral, resting position as before. After collecting data of these initial movements, the SEMG-FMG sensors and housing were rotated or shifted away from this "ideal position".

By moving the sensor housing, we simulated the shifting of a user's prosthetic socket during activities of daily life. The sensor housing was relocated from the ideal position by 1 cm. Repositioning of the sensor housings occurred in four directions referred to as "lateral",towards the radius, "medial", towards the ulna, "proximal", or shifted towards the elbow, and "distal", or shifted towards the user's hand. This process was then repeated, offsetting the sensors and sensor housing 2 cm from the "ideal position". All sensor housings were rotated or shifted in the same direction. The subject repeated extension and flexion motions at least 10 times each, in each of the eight offset positions.

4.2.1.3 Simulating arm positions during activities of daily living

Additionally, the subject repeated flexion and extension motions, with sensors in the ideal sensor locations, in several arm configurations while standing. These arm configurations included positioning the shoulder laterally across the body (adduction), 90 degrees abduction, 135 degrees of shoulder flexion in the sagittal plane , ie. with the hand at approximately head-level, and 45 degrees shoulder flexion in the sagittal plane, ie. with the hand approximately waist-level. Figure 4.6(a)- 4.6(d) illustrates the basic arm positions used to during experimentation while the subject was standing.

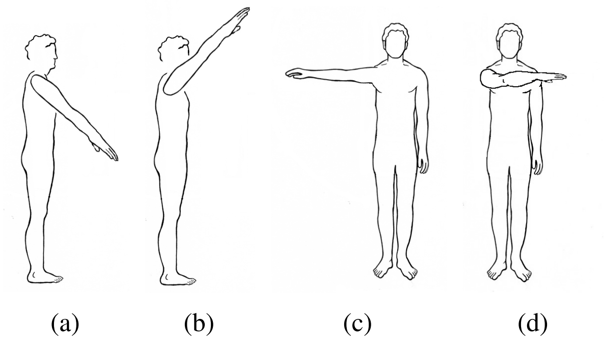

Figure 4.6: Arm positions used while gathering data while simulating arm positions found during activities of daily living. a) Arm 45 degrees shoulder flexion in the sagital plane (the hand approximately at waist-level) b) Arm 135 degrees of shoulder flexion in the sagittal plane (hand at approximately head-level) c) Arm out, away from the body (90 degrees abduction) d) Arm laterally across the body (adduction) with their elbow fully extended

4.2.1.4 SEMG and FMG while fatigued

The subject was seated comfortably in a chair as described before in the in Section 4.2.1.2. The subject sat, rested their arm in a comfortable position and positioned their hand in a neutral position. The socket and sensor housing was placed in the “ideal” location on the arm above the forearm muscles. In order to create forearm muscle fatigue, the subject was then instructed to apply their maximum force to a sensorized-rectangular piece of plastic with their dominant hand in a “key pinch” grip. A single piezeoresistive sensor was mounted between this piece of plastic and a solid surface with cellophane tape.

An initial reading of applied force was taken. Following this initial reading, the subject squeezed a rubber ball covered in felt, ie. a tennis ball, ten times at a frequency of 60bpm. The metronome was used to provide auditory cues for a consistent squeeze rate. The subject then squeezed the sensorized-rectangular piece of plastic as before. This procedure of squeezing a tennis ball and immediately providing a force output measurement was repeated until the subject's output force measurement was 80% of the initial reading. All readings were taken with the socket in the "ideal position" as defined above.

4.2.1.5 Recording Radial and Ulnar Deviation of the hand

The subject was seated comfortably in a chair as described before in the in Section 4.2.1.2. The subject sat, rested their arm in a comfortable position and positioned their hand in a neutral position with their thumb pointing "up". The socket and sensor housing was placed in the "ideal" location on the arm above the forearm muscles. The subject was instructed to deviate their wrist and hand in the ulnar direction, towards the "pinky" finger, repeating this motion at least 10 times. The subject was instructed to return their hand to a neutral, resting position after each motion. The subject was then instructed to deviate their hand in the radial direction, towards the thumb 10 times, returning to a resting neutral position following each motion.

These movements are meant to capture data of the hand performing a simulated "hammering" or "dart throwing" motion, an activity common during daily life.

4.2.2 Materials

For this study we have prototyped a heterogeneous sensory input system to control a powered prosthetic device based around four SEMG sensors and four colocated piezoresistive force sensors. Activation of a desired control input is via excitation of the user's forearm muscles and the resulting increased intra-socket force and electromyograhpic signal.

4.2.2.1 Socket and Sensor Housings

Initial work correlating surface EMG and intra-socket pressure made use of a simplified sensor housing was described in [120] which can be seen in Figures 4.7(a) and 4.7(b). This setup allowed a single surface EMG and single pressure sensor to be co-located above the subject's forearm muscle, and easily relocated as part of that previous work. An expanded system, including housings for an opposing pair of pressure sensors was demonstrated in [133]. This system continued to make use of piezo-resistive force sensors, using two opposing Flexiforce A201 sensors. This system allowed a user access to two input modalities, flexion and extension of their dominant hand, by sensing changes of intra-socket pressure in a simulated prosthetic socket. Figures 4.5(a) and 4.5(b) illustrate basic placement of the sensors above the muscle bodies activated during gross flexion and extension movements of the subject's dominant hand.

The system used in this work expands on previous prototypes and includes four Delsys Bagnoli EMG sensors (Nattick, Massachusetts) and four collocated with FlexiForce A201 model piezo-resistive force sensors. These sensors were positioned over the extensor and

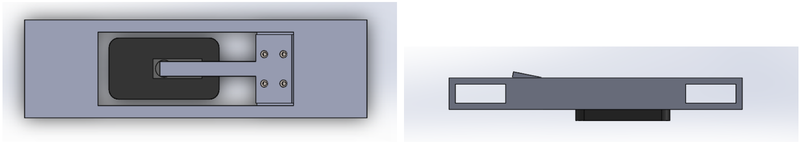
(a) (b)

Figure 4.7: Proof of Principle SEMG and colocated piezoresistive force sensor housing. a) Top and b) Side views. The SEMG sensor can be seen (dark grey), with the collocated force sensor (light grey) attached above it, but under the cantilever.

flexor muscles of the forearm as mentioned in Sections 4.1.2. Sampling of EMG data occurred at 2.4kHz. The four FMG sensors were mounted above the EMG sensors, in contact with the surface of the EMG sensors and the sensor housing. Figure 4.5(a) illustrates the placement of one of the four pairs of EMG and Force sensors.

Prior to creation of the sensor housings, four EMG sensors were placed above the flexor and extensor muscles of the subject's dominant forearm. These locations were marked on the subject's skin. A three dimensional model of the subject's dominant arm was then created, using a 3DMD Flex4 [134] three dimensional scanning system to provide a scan of the subject's arm and CAD software. A custom socket was created from this model and sensor housings were created above the marked EMG sensor locations. The socket was 3-D printed using ABS plastic.

4.2.2.2 Data Acquisition

A Delsys Bagnoli EMG system, National Instruments DAQ, a custom circuit including an Arduino Micro and LabVIEW program were used to gather data for this work. The Delsys Bagnoli 16 channel EMG system was directly connected to an NI (National Instruments) USB-6210 DAQ for EMG data acquisition. A custom voltage divider circuit was created to gather pressure data from the four piezoresistive sensors, making use of an Arduino Micro micro-controller. This voltage divider circuit was also connected to the NI USB-6210 DAQ. In conjunction to the mentioned hardware, a custom LabVIEW VI program was written. This program allows users to start and stop data gathering, change data sampling rates, view data in real-time in a graphical display, and output data to TDMS file formats. These TDMS files are later processed and classified and are described in 4.2.2.3.

4.2.2.3 Classification Algorithm

A custom Matlab program was created to process the gathered data, classify that data using a feed-forward neural network, and determine the motion of the subject's hand. Data acquired using the system described in 4.2.2.2 was converted from TDMS file format to CSV for processing.

Then, EMG and FMG data was classified using the Matlab Neural-Network Toolbox in a multi-layer perceptron feed-forward configuration. SEMG parameters described by Hudgins, *et., al* are used as network inputs along with piezo-resistive pressure sensor data[132]. These inputs to the network were the moving average of the absolute value of the SEMG signal, the derivative of the absolute value of the SEMG data, and the absolute value of the pressure data. The time vectors of SEMG data and pressure data are denoted as r_t and p_t respectively. $\hat{r}_t$ is defined as the magnitude of the time vector of SEMG data, as seen in Equation 4.1, above. The Central Moving Average of the absolute value of the SEMG signal is referred to as *CMA* and has window size denoted, ω_1. A *central moving average* computation was performed shown, in Equation 4.2, as described above in Section 4.1.6. However, instead of Equation 4.7, a Central Moving Average and slope calculation occurred for the pressure data, shown in Equation 4.9.

$$\mu_3 = slope(MA_{\hat{p}_t}) = MA_{p_t} - MA_{p(t-\omega_2)} \tag{4.9}$$

70% of the sampled moving difference window data was used as training input, testing and validation evenly split between the remaining 30%. All data was subdivided in to these groups, training, testing, and validation randomly.

Data were classified for an action when the SEMG moving average was above signal noise, the slope was positive over a moving window, and pressure data showed a positive value over a moving window. The SEMG noise-threshold was found by multiplying the CMA value by 1.5 (for SEMG). Hidden layer sizes of 1-10, 50, 100, and 1000 were tested. A 10 neuron hidden layer size was chosen and used for training as significant improvements to classification error rate percentages were not seen beyond this value. A more detailed explanation of this process can be found in previous work, [120], along with sample SEMG and FMG data and wave-forms. Training was repeated until no significant improvement in the network weights or outputs was seen, approximately ten times. The *scaled conjugate gradient* method was used to update weights and bias values[135].

Data were classified using one of the eight trained multi-layer perceptron, feed-forward neural network classifiers. Four of these classifiers included training data solely consisting of EMG data. Separately, four neural networks were trained considering each SEMG-FMG pair, for a total of eight inputs and two outputs with the result of determining if an action had occurred. Separately, two networks were trained to classify wrist deviation, one using SEMG data only and one using both SEMG and FMG data.

Training data for the first eight networks consisted of data while the subject was seated and the socket and sensors were in the "ideal" position, while the subject was standing and the socket was in the "ideal" position, and while the subject was seated and the socket had been shifted. Descriptions of these data sets can be found in Section 4.2.1.2. Training of the two additional networks, as part of the data set described in Section 4.2.1.5, occurred while the subject was seated and the socket was placed in the "ideal" position. Data from the data set described in Section 4.2.1.4, while the subject was fatigued, was not included in any training set. Discussion of this exclusion can be found below. A table describing which data are included in each of the eight data sets used to train the classifiers can be seen in Table 4.1. Column labels can be described as: EMG, FMG, "ideal" socket position, various arm positions while standing, and "shifted" socket positions. The "shifted socket" data were included in a single training set and classifier. For clarity during discussion below, the classifiers will be referred to by a short-hand, concatenating the names of the data sets used to train the networks. For example, *Classifier 1* will be referred to as “EMG_I”, ie. “EMG data while the socket is in the “ideal” position” (Classifier 2-EMG&FMG_I, Classifier 3-EMG_ISt, Classifier 8-EMG&FMG_IStSh etc.).

Table 4.1: Experimental Data Included in Each Training Set for each Neural Network Classifier

	Sensors		**Socket/ Arm Position**		
	EMG	**FMG**	**ideal**	**standing**	**shifted**
Classifier 1	**X**		**X**		
Classifier 2	**X**	**X**	**X**		
Classifier 3	**X**		**X**	**X**	
Classifier 4	**X**	**X**	**X**	**X**	
Classifier 5	**X**		**X**		**X**
Classifier 6	**X**	**X**	**X**		**X**
Classifier 7	**X**		**X**	**X**	**X**
Classifier 8	**X**	**X**	**X**	**X**	**X**

4.2.3 Results

Eight different classifiers were trained. The first two classifiers were trained using only data collected while the socket was in the “ideal” position and the subject was seated. These classifiers are used as a base or control to compare against. The first of the two control classifiers included only data from the EMG sensors. The second control classifier included EMG and FMG data. A table describing the data included in each training data set can be seen in Table 4.1. Data sets 1 and 2, as labeled in the above mentioned table, are the control data sets. All eight networks were tested against data while the socket was in the “ideal” position while the subject was seated, against shifted socket data, against data gathered while the subject was standing, and against data gathered during times of subject fatigue. Comparisons were also made between classifiers not including pressure data and those that included intrasocket pressure data. Final results of classification of data during times of fatigue are reported. However, no data from trials during times of fatigue were included in training data. Separately, two networks were trained to classify radial and ulnar deviation of the hand while the simulated socket was in the "ideal" position and the subject was seated.

Figures 4.8(a)- 4.11(b) show the results of classification, presented as confusion matrices. The *main diagonals indicate the percentages of "correct" classification* for flexion and extension, radial or ulnar deviation, or "no action". *Off-diagonal values show the percentages of mis-classifications*. Data is presented as averages of flexion and extension classification data over the entire experiment, for each classifier. The entire matrix will sum to approximately 100%, due to rounding of significant digits. An additional discussion of confusion matrices can be found in [135] and [136].

4.2.3.1 Performance against Arm Positions during Activities of Daily Living

This section reports results of the eight neural networks when classifying data described in Sec. 4.2.1.3. The movements made by the subject simulated arm positions during activities of daily living. The subject performed wrist flexion and extension motions while their dominant arm was in the four positions as seen in Fig. 4.6(b)- 4.6(d). Figures 4.8(a)- 4.8(h) report the average performance data for each classifier, for each data set.

4.2.3.2 Performance against Socket Shift

Figures 4.9(a)- 4.9(h) report results of the eight neural networks when classifying data described in Sec. 4.2.1.2. This experiment simulated socket shift as experienced when a prosthetic socket moves due to socket-pull-out or poor socket fit. The subject performed wrist flexion and extension motions while their dominant arm was resting on an arm rest.

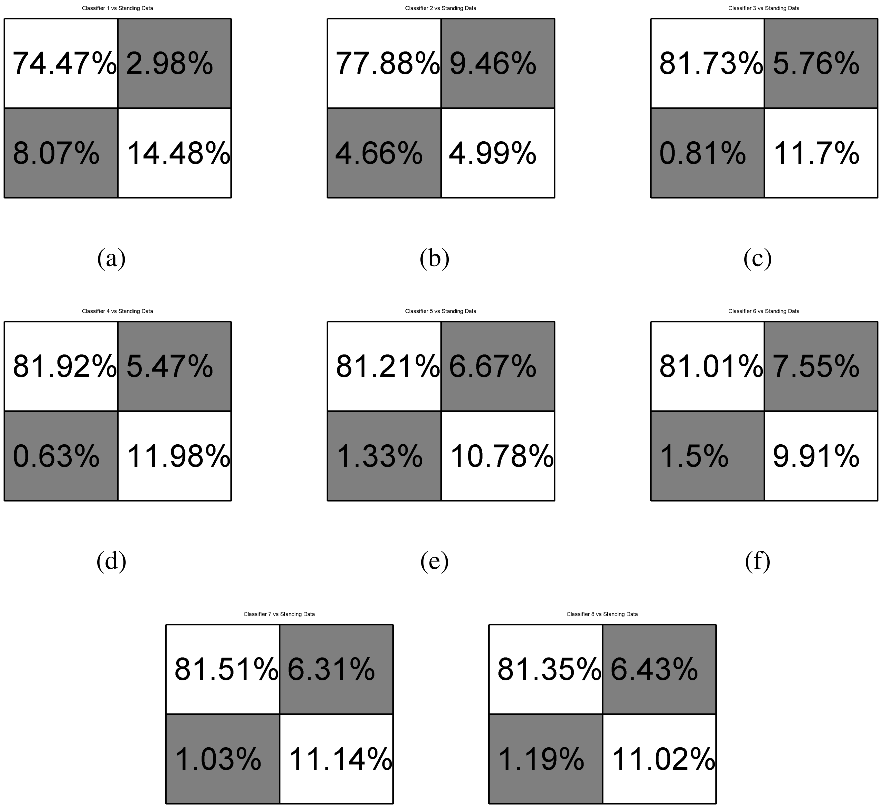

Classifier 1 vs Standing Data

74.47%	2.98%
8.07%	14.48%

(a)

Classifier 2 vs Standing Data

77.88%	9.46%
4.66%	4.99%

(b)

Classifier 3 vs Standing Data

81.73%	5.76%
0.81%	11.7%

(c)

Classifier 4 vs Standing Data

81.92%	5.47%
0.63%	11.98%

(d)

Classifier 5 vs Standing Data

81.21%	6.67%
1.33%	10.78%

(e)

Classifier 6 vs Standing Data

81.01%	7.55%
1.5%	9.91%

(f)

Classifier 7 vs Standing Data

81.51%	6.31%
1.03%	11.14%

(g)

Classifier 8 vs Standing Data

81.35%	6.43%
1.19%	11.02%

(h)

Figure 4.8: Confusion Matrices comparing Classifiers to Standing Data. Matrices a, c, e, g, used on SEMG data. Matrices b, d, f, h used SEMG and FMG data. a) Classifier 1-EMG_I b) Classifier 2-EMG&FMG_I c) Classifier 3-EMG_ISt d) Classifier 4-EMG&FMG_ISt e) Classifier 5-EMG_ISh f) Classifier 6EMG&FMG_ISh g) Classifier 7-EMG_IStSh h) Classifier 8-EMG&FMG_IStSh

The simulated prosthetic socket was then moved, as described above, 1cm and 2cm away from the "ideal" socket position. Figures 4.9(a)- 4.9(h) report the average performance data for each classifier, for each data set.

4.2.3.3 Performance against Fatigue

Figures 4.10(a)- 4.10(h) report results of the eight neural networks when classifying data collected in Sec. 4.2.1.4. This experiment simulated user fatigue as experienced

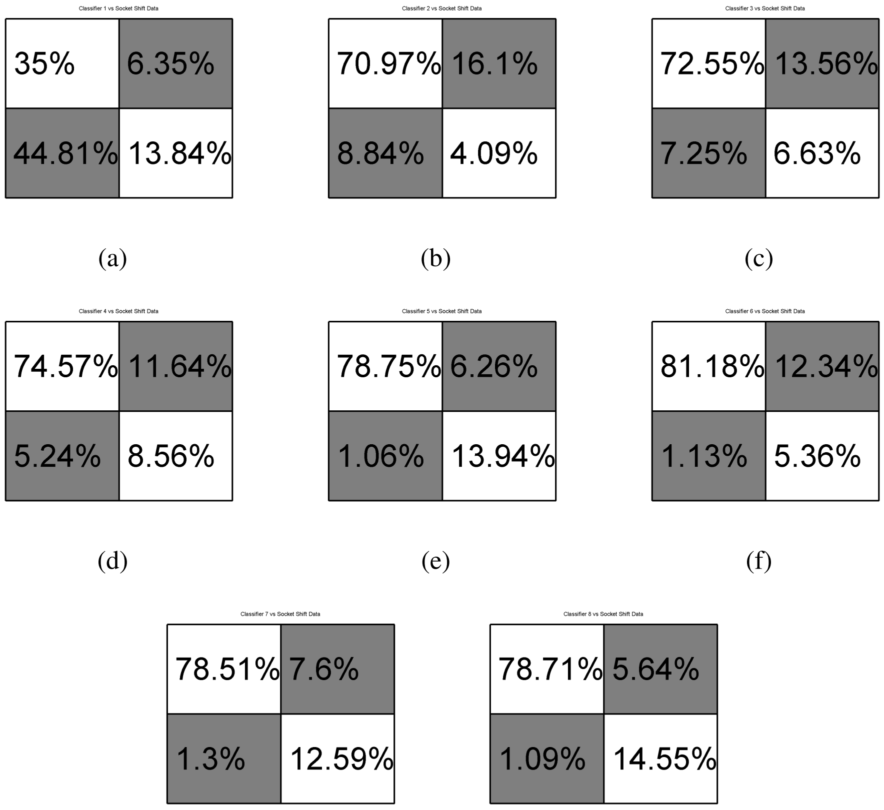

(a) (b) (c)

(d) (e) (f)

(g) (h)

Figure 4.9: Confusion Matrices comparing Classifiers to Socket Shift Data. Matrices a, c, e, g, used on SEMG data. Matrices b, d, f, h used SEMG and FMG data. a) Classifier 1-EMG_I b) Classifier 2-EMG&FMG_I c) Classifier 3-EMG_ISt d) Classifier 4-EMG&FMG_ISt e) Classifier 5-EMG_ISh f) Classifier 6EMG&FMG_ISh g) Classifier 7-EMG_IStSh h) Classifier 8-EMG&FMG_IStSh

throughout a user's typical day of powered prosthetic use. The subject squeezed a felt ball ten times and then squeezed a force sensor. These motions were repeated until the force output was reduced to a 80% of the initial force output. The user then performed wrist flexion and extension motions while their dominant arm was resting on an chair's arm rest. Figures 4.10(a)- 4.10(h) report the average performance data for each classifier, for each data set.

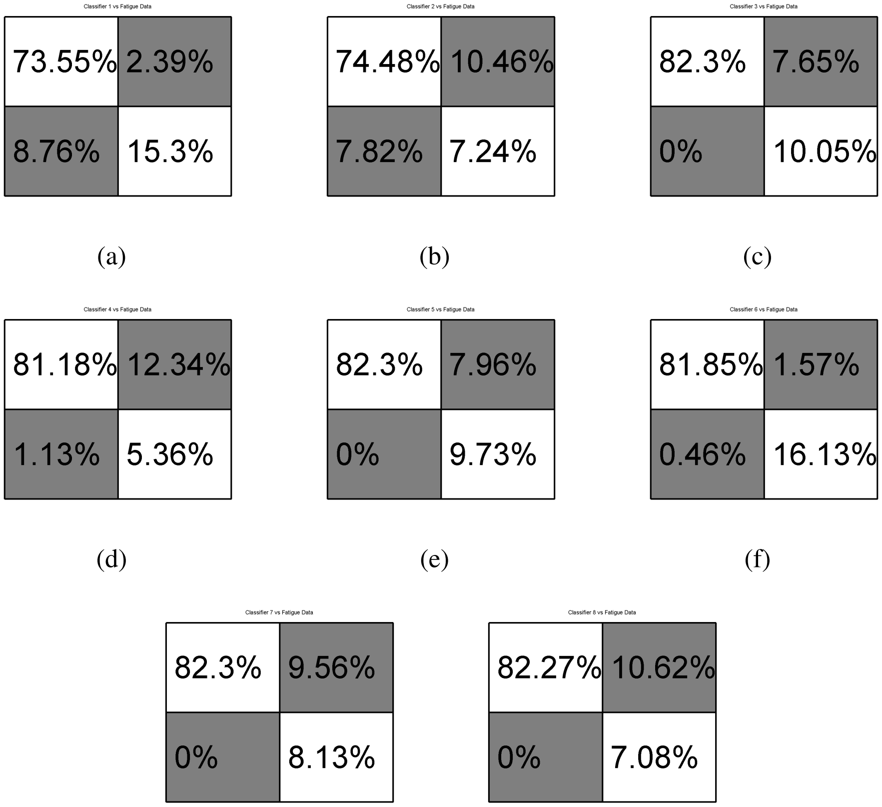

(a) (b) (c)

(d) (e) (f)

(g) (h)

Figure 4.10: Confusion Matrices comparing Classifiers to Fatigue Data. Matrices a, c, e, g, used on SEMG data. Matrices b, d, f, h used SEMG and FMG data. a) Classifier 1-EMG_I b) Classifier 2-EMG&FMG_I c) Classifier 3-EMG_ISt d) Classifier 4-EMG&FMG_ISt e) Classifier 5-EMG_ISh f) Classifier 6EMG&FMG_ISh g) Classifier 7-EMG_IStSh h) Classifier 8-EMG&FMG_IStSh

4.2.3.4 Performance of Radial and Ulnar Deviation Classification

Figures 4.11(a) and 4.11(b) report results of the trained neural network when classifying data collected in Sec. 4.2.1.5. The movements made by the subject simulated radial and ulnar deviation of the a user's hand during activities of daily living, such as during a "hammer" or "dart throwing" action. The subject deviated their dominant wrist ten times in the radial direction and then ten times in the ulnar direction while their dominant arm was

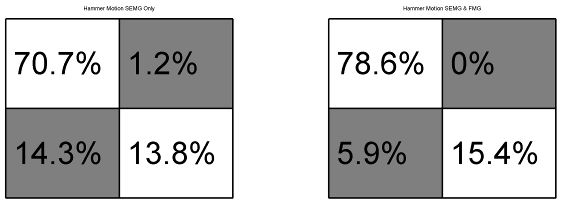

Hammer Motion SEMG Only

70.7%	1.2%
14.3%	13.8%

Hammer Motion SEMG & FMG

78.6%	0%
5.9%	15.4%

(a) (b)

Figure 4.11: Confusion Matrix reporting classification results for radial and ulnar deviation of the hand a) 4 SEMG inputs b) SEMG and FMG inputs

resting on an chair's arm rest. Figure 4.11(a) reports the average performance data for the classifier for this experiment using only the four SEMG sensors as input. Figure 4.11(b) reports the performance data for the classifier for this experiment using the four SEMG sensors and the four FMG sensors as input. These classifiers were trained and tested against data from this experiment only; 70% of the time samples were used for training, 15% for validation, 15% for testing.

4.3 Discussion

Flexion and extension motions were chosen for this study as a means of testing data typically available to "the greatest number of lower arm prosthetic users". Current commercial upper limb prosthetics already use SEMG from wrist flexion and extension. While it is true that clinical results using the most advanced techniques available in the literature boast classification results much higher then those presented here, the classifiers trained in this study were chosen for the simplicity and ease of implementation and to provide a baseline performance for comparison of classification of SEMG data to SEMG-FMG data. The improvements in classification rate percentages are significant considering the simplicity of these techniques. The results of classification using more advanced non-linear classifiers, such as Radial Basis Functions or Gaussian Mixture Models, will then have a basis for comparison.

It can be seen from Figures 4.8(a)- 4.10(h) that in general, those classifiers trained using larger training sets, *Classifiers 7 & 8* performed better than the classifiers including shorter training sets, *Classifiers 1-EMG_I & 2-EMG&FMG_I.* It is thought that inclusion of more data, more examples of flexion and extension motions, provides a more robust classifier. This can be illustrated by comparing the classification of activities of daily living data using different classifiers trained using different training data sets; 74.47% (*Classifiers 1-EMG_I*), 77.88% (*Classifiers 2-EMG&FMG_I*), 81.51% (*Classifiers 7-EMG_IStSh*), and 81.35% ((*Classifiers 8-EMG&FMG_IStSh*). This was also confirmed by Fougner *et, al* during their experiments which included data collected with the subject's arm in various positions and not just resting on a table top or a chair's arm.

From the data gathered as described in Sec. 4.2.1.3 & 4.2.1.2, it can be seen that those classifiers including intrasocket pressure data and SEMG outperformed classifiers with data collected from surface EMG only. This is especially true when considering *Classifiers 1-EMG_I & 2-EMG&FMG_I* during socket shifts, 35% compared to 70% classification rate. These classifiers were not trained with data collected when the socket was shifted but were tested against "shifted" data (Section 4.2.1.2. Interestingly, *Classifiers 3-EMG_ISt & 4-EMG&FMG_ISt*, trained including data while the subject's arm was in different positions, outperformed *Classifiers 2-EMG&FMG_I.* Comparing *Classifiers 2-EMG&FMG_I & 3-EMG_ISt*, one can see that a classifier using four SEMG and four FMG sensors is nearly as accurate as a classifier including additional training data. This could have implications during initial training, implementation, and deployment for a prosthetic user. One can imagine a system allowing for retraining of the classifier "at home, by the user" should functionality degrade. It would be preferable to have a shorter number of "retraining motions" needed in this case.

Fougner, *et al.* and Radman report to have improved SEMG signal classification errors due to limb position effects through fusion with accelerometry data Fougner2011,Fougner2012, Radman02014. While effective, more computationally intense data processing and classifiers were needed than were used in this work, a *linear discriminant analysis classifier* specifically. A larger array of SEMG sensors were necessary as well, eight (Fougner) and six (Radman) EMG sensors, along with additional accelerometers. It should also be noted that while socket shift was said to be accounted for in these work, actual socket or sensor displacement due to activities of daily living was not measured. This displacement was deliberately accounted for in the work presented here. Experiment 4.2.1.3 is meant as a means to effectively compare against the shifted socket, Experiment 4.2.1.2, where the sensor housings were displaced a controlled distance away from the ideal position. By performing linear shifts while the subject's arm was resting on a chair's arm-rest, EMG effects due to varied arm positions can be eliminated.

From data found in Fig. 4.8(a)- 4.8(h), one can see that *Classifiers 3-EMG_ISt - 8-EMG&FMG_IStSh* performed approximately equally. But, they did outperform *Classifier 2-EMG&FMG_I* which in turn outperformed *Classifier 1-EMG_I*. That is to say that classifiers including SEMG and FMG data as part of their training sets performed approximately equally to classifiers including only SEMG data when additional training data collected when the subject's arm is in different positions, is included. But, a classifier using the eight sensor set up outperforms the SEMG-only setup when additional training data is *not* included. This same conclusion can be made when comparing and classifying samples during times of user fatigue as seen in Fig. 4.10(a)- 4.10(g).

It should be noted that while the subject reported their arm "feeling tired", they did not report "feeling sweaty". A degradation of the measured amplitude of the SEMG signal of 2%-3%, depending on the type of sensor used, for every 0.02mm of sweat between the surface of the skin and the sensor was determined in [60]. Perspiration, a conductive fluid, can also cause intermittent short-circuits of an EMG sensor. While this can be partially compensated for as proposed by [59], a high frequency oscillator is necessary for signal injection, and is not used in clinical settings and the author is unaware of any production systems making use of this method. The system presented in this paper avoids EMG signal degradation issues due to sweat by making use of a multi-modal sensory input. Despite this, future experiments should attempt to force the subject to exert themselves enough to cause sweat on the skin surface in order to further test the SEMG-FMG system.

Figures 4.11(a) & 4.11(b) report findings from classification of radial and ulnar deviation motions of the subject's wrist and hand. These motions are found during several activities of daily living, including "hammering", "dart throwing" and many others. A significant improvement in classification can be seen between the two methods presented here, using only surface EMG and using a combination of surface EMG and force myography. It is believed that a more advanced classification algorithm could provide even further improvements. To this author's knowledge, classification of these actions has not been reported before in the literature. Previous work has focused on improving dexterous finger motions and classification. It should be noted that also to this author's knowledge, no powered prosthetic devices currently available to the public are able to provide this capability to a robotic hand. Currently, only wrist rotation actions are possible with available devices. The authors feel that the addition of radial and ulnar deviation to a powered device would improve usability and decrease long-term, compounding injuries of the remainder limb's elbow and shoulder joints.

It should also be noted that although methods for classifier training will be the same across a cohort of subjects, due to customization of the socket, only a single subject was considered at this time. Future work will necessitate testing of this technique using a larger number of subjects as well as a trans-radial powered prosthetic user.

No training sets included data collected during the fatigue experiment of 4.2.1.4. This protocol was used due to hardware limitations and in an attempt to measure classification robustness as the user perspired. Due to the nature of the method of data acquisition and signal processing performed and described above in Section 4.2.2.2 and 4.2.2.3, EMG signal frequency was not recorded. Future hardware will take this in to account, measuring the median EMG signal frequency, and using this as a means of determining user fatigue. Despite these limitations, this protocol allowed us to gather data and see that *Classifiers 3-EMG_ISt - 8-EMG&FMG_IStSh* were able to perform approximately equally and classify user intent.

Prior work by Young *et, al* discusses classification errors based on socket shift direction along the muscle body[57]. Young *et, al* found that socket shift, sensor displacement, affected classification more readily when the socket shifted perpendicularity to the muscle fiber, ie, rotated around the arm as compared to moved more distally or proximally. While we gathered data shifted in a similar method to Young*et, al*, we did not control for direction of shift as part of the classifier training. Only linear distance away from an ideal location was considered and controlled for. Study of classification results from a limited data set, taking shift direction in to account, should be undertaken. Future work may show that improvements in a reduction of training motions can be made by only rotating the socket without also moving the socket distally and proximally along the forearm.

While fine gesture recognition for highly dexterous motions is beyond the scope of this study, it has been considered in works by Scheme and Fougner, for example. While there has been interest in classifying data from a large array of EMG sensors, the advantages of studying smaller arrays for pattern recognition are apparent. Implementation will require real-time control of a device, making use of a micro-controller, more readily possible with fewer input signals. Sensor size must also be taken in to account when constructing a practical socket as well as actual, available muscle sites on a prosthetic user.

Advanced classification algorithms were not considered as part of this study as the goal was to test an SEMG-FMG system against an SEMG only system, using a known classification algorithm as a bench-mark. Additionally, large training sets were compared to more simple training sets. Classifiers trained in the method shown here would also inherently be tailored to an individual user and their individual SEMG and FMG signal profiles; generalized systems trained on data not gathered from the individual would not perform as desired. This is not seen as a disadvantage as training times are small and future systems could allow for retraining of systems online.

4.4 Control of a Powered Prosthetic via Pinch Gesture and Force Myography

In addition to the intra-socket pressure and sEMG correlation study already mentioned, a proof of principle device was completed allowing for activation and control of a powered prosthetic gripper. This low-encumberance device allowed for rapid switching between prosthetic grip configurations through the use of a wearable pinch gesture based grasp pattern switching method using finger-worn contact thimbles. Activation of the desired pattern is controlled through excitation of the user's forearm muscles and the resulting increased intra-socket force.

4.4.1 Contact Sensor Thimbles

A user is able to choose from a series of predefined gestures through the use of contact sensors worn on the tips of the fingers of their healthy hand. These custom contact sensors were molded from thermoplastic [137] and wired to an Arduino microcontroller [138]. This microcontroller read the user defined gestures and is used to control the grasp pattern of a Touch Bionics i-Limb hand [139]. The data acquisition software is described in more detail in a subsequent section. In order to chose a grasp pattern, a user makes contact between the tip of the thumb of their healthy hand, encased in a contact sensing thimble, with the tip of the finger, or combination of fingers, on their healthy hand. A figure showing the subject wearing the device is shown below in Figure 4.13.

4.4.2 Healthy Limb Socket and Prosthetic Device

It has been shown that able-bodied individuals can be considered as research analogs during initial studies of EMG data acquisition, classification algorithm development, and powered prosthetic development in general. From this assumption, a custom, prosthetic trans-radial amputee socket analog for for an able-bodied individual was created. See Figure 4.12. An alginate [140] mold was created of the subject's dominant side lower arm, below the bicep, and a plaster cast was created from this mold. From this plaster cast, a thermoplastic [141] socket was created by first wrapping the outside of the forearm in the socket material, thermoplastic, and then layering subsequent layers inside of the socket. These internal layers are necessary for proper fit of the socket to the subject's arm.

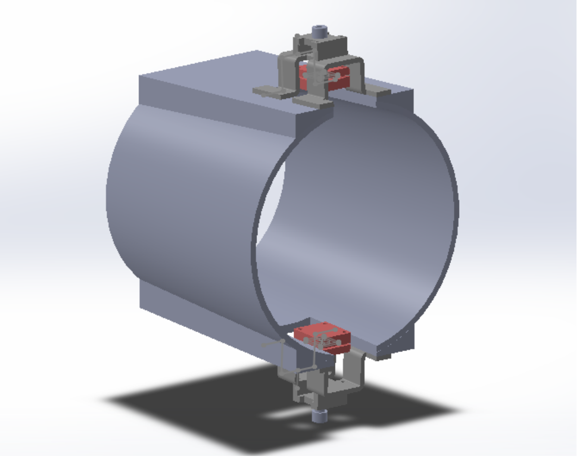

Figure 4.12: CAD model illustrating Pressure Sensor Housings in Superior and Inferior positions on healthy-limb socket analog (rear view)

The hand flexion and extension of the forearm were identified on the subject, located on the anterior and posterior sides of the forearm. These points were marked and corresponding positions within the socket were identified. Above these positions, custom designed sensor housing were mounted, as seen in Figure 4.12 and similar in design to those found in prior studies. These housings secured piezo-resistive force sensors for interaction detection. As the subject flexes or extends their hand, the carpi flexor and carpi extensor muscles change in volume. This volume change is detected as a force applied to the inside of the socket and is detected by the piezo-resistive sensor. Further discussion of the sensor, and data acquisition, is discussed in the Section 4.4.3.

Figure 4.13: The experimental setup, including contact sensors, healthy limb socket, and prosthetic device. The subject can be seen performing a hand extension action with their right hand.

A Touch Bionics i-Limb Ultra Powered Prosthetic Hand [139] was used to demonstrate possible grip configurations. Each of the 6 degrees of freedom are independently controllable, using an open-loop controller. Absolute position control is not possible at this time, the device is motor-driven and not servo-driven, but control of position via motor-drive-timing methods is to be explored in future work. Standard user interaction with this powered device involves the selection of a grip-type via an application stored on a mobile-device or chosen by "scrolling through" pre-programmed grip-patterns using a surface EMG as a scroll switch. Opening and closing of the grip is completed via a predefined input through the surface EMG. An alternate method of grip selection is described in the Section 4.4.3. The device itself was mounted to a housing using a standard Ottobock Quick Disconnect [142][139]. The housing and supporting hardware can be seen in Figure 4.13, in the background.

4.4.3 Data Acquisition of Pressure Sensor Data

The user interacts with this system through two main sensing modalities. Intra-socket force data is collected using two ultrathin FlexiForce® A201 model piezo-resistors (thickness - 0.208mm; active sensing area - $0.713cm^2$; force sensitivity range - 20g - 2200kg; response time - 5-20μsec; linearity¡ ±5%) [30]. These sensors are mounted inside the socket housing as described in the previous section. This intra-socket force is used to control the opening, closing, and stopping of the motion of the powered prosthetic device. That is to say that as a user activates the flexor or extensor muscles of the forearm of their remainder limb, these piezo-resistive sensors detect this force, and through the use of a classification algorithm described below, control the activation of the i-Limb hand.

A National Instruments myRIO device collects data and, using a custom written VI, performs processing and controller functions. The intent classification algorithm is described below in the Section 4.4.1. On the fly grip configuration choice is accomplished using custom contact sensors, described in 4.4.1, connected with an Arduino microcontroller running task specific software written for this application. This software determines which fingers have made contact with the thumb of the healthy hand, and depending on a predefined grasp pattern, pass this information on to subsequent portions of the system. Through this hand-mounted system, a user is able to define grip configurations in a natural way. Once prompted, through the activation of the user's forearm muscles and the Flexiforce force sensors, the i-Limb hand outputs the pre-defined grasping motion.

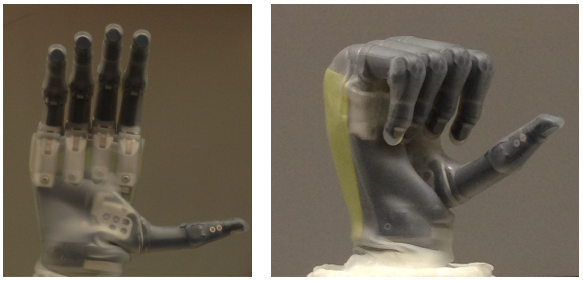

Figure 4.14: The prosthetic device in the fully open (left) and fully closed (right) positions.

4.4.4 User Interface Algorithm

A user controls the device making use of hardware inputs as commands to open or close the prosthetic hand, as previously discussed. An "open" gesture is defined as where the prosthetic device is in a configuration where the device's fingers are fully extended. A "closed" gesture is defined as where the fingers of the prosthetic hand are in full flexion. For the general case, a "closed" gesture can be thought of as a "fist". Examples illustrating this can be found in Figures 4.14. Figures illustrating the defined grips can be seen below in Figures 4.16. Two software defined thresholds were applied to these inputs: a signal amplitude level v_{th} and a time t_{th} threshold. To detect a valid command, the sensor signal has to cross v_{th}, at which point a timer is started. Once the timer reaches t_{th}, the open or close command is sent to the prosthetic hand. However, if the signal crosses v_{th} again before t_{th} is reached, the timer is reset and no command is sent to the hand. This ensures that sensor noise does not accidentally activate the hand and that a command is only sent when there is clear intent from the user. The two signals are processed individually and the action is determined according to Table 4.2.

Currently, it is assumed that the user will be activating the carpi flexor or carpi extensor muscles individually. That is to say that the signals s^1 and s^2 are either reading a constant value or reading inverse values. When the user flexes the hand, muscle X1, the carpi extensor, relaxes while muscle X2, the carpi flexor, expands resulting in a low value

Table 4.2: Control signals according to sensor input.

Action	s^1	s^2	o
Stop	low	low	-
Nothing	low	high	-
Close	high	low	0
Open	high	high	1

for s^1 and a high value for s^2. When the user tries to extend the hand, muscle X1 expands while muscle X2 relaxes resulting in s^1 being high and s^2 being low.

While deep muscle interactions of the forearm muscles are not fully understood, activation of these two muscles during flexion and extension of the hand is possible and provides readable data.

A Simple Moving Average (SMA) filter was used to pre-process the signals. It acts as a low-pass filter and reduces noise by smoothing out short-term fluctuations. The formula is

$$\mathrm{SMA}_k = \frac{1}{n} \sum_{i=k-(n-1)}^{k} s_k \tag{4.10}$$

which is the unweighted mean of the previous n data at time step k. A 100ms window was used, corresponding to $n = 1000$ samples for $\Delta t = 10$ms. This data was then written to a file in the .CSV format and saved for later analysis.

4.4.5 Experimental Evaluation with Human Subjects

Comparison between currently available usage scenarios of the powered prosthetic hand and the proposed method were completed and the experimental method is reported below. Data reporting findings from this experiment is reported below in the *Results* section. Proof of concept testing occurred prior to this experiment and is reported in the 4.4.6 section.

A single right hand dominant subject was recruited during this proof of concept experiment. Written consent was given after being informed of the test procedure, which was approved by the local ethics review committee.

During Proof of Concept testing, basic instruction regarding tasks to be performed were described to the subject. However, precise hand or arm configurations were not defined or prescribed. Three separate actions were performed while the subject held their forearm at approximately 90 degree elbow flexion. The subject performed all actions while sitting comfortably in a chair. The non-dominant hand was clad in the contact sensing thimbles and apparatus. The dominant arm rested in a neutral position with the elbow at 90 degrees flexion. Grip choice was made by the user by touching the tip of their thumb to the fore-finger, thumb to middle-finger, and thumb to ring-finger of their non-dominant hand. The subject was immediately instructed to flex their dominant hand from a relaxed position. These actions were repeated for each of the three grip selections. A brief table describing the motions and expected actions is included below in Table 4.2.

A comparison was to be drawn between usage scenarios of the robotic hand and a prosthetic user, during experimentation. A healthy-limbed subject was instructed to interact and operate the i-Touch prosthetic hand using two separate methods. The first method used the bundled smart-phone application available for download from TouchBionics. Communication between the smart-phone and the i-Limb hand occurred via Bluetooth. A user made a selection of their desired grip-type from a list of pre-built hand configurations, on the screen of their smart-phone, and this choice was communicated wirelessly to the hand. The subject was instructed to retrieve their smart-phone from their pocket, input the randomly selected grip-configuration choice as described by the experimenter, and then close the hand using the intra-socket force sensors described previously in the *Contact Sensor Thimbles and Healthy Limb Socket* sections. The smart-phone's screen was left unlocked during the entire experiment. Following each grip-selection, the subject's smart-phone is returned to their pocket.

The second interaction method was via the contact thimbles described previously. The subject was outfitted with contact sensor thimbles and read a series of randomly selected gesture numbers. Figure 4.13 illustrates the complete experimental setup. Upon instruction of which gesture was to be selected, the subject was told to close the i-Limb robotic hand using the intra-socket force sensors.

A total of twelve trials were completed by the subject for each of the two input methods. During all trials of the experiment the subject held their forearm at approximately 90 degree elbow flexion while seated comfortably in a chair. And, while the time of each trial was recorded, the subject was not instructed on relative speed with which to perform the actions. Sufficient rest was given to the subject between usage scenarios.

4.4.6 Results

Intra-socket force data and grip selection choices were measured during several experiments. Intra-socket force is a measure of the recorded forces as applied by the subject to inside of the healthy-limb socket system. Experimental data from the usage scenario experiment is reported below. Grip selection choice is a measure of the ability for a user to successfully choose a pre-defined grip and activate that grip using intra-socket force.

Table 4.3: Pinch Gesture and ForceMyography: Grip Selection Pattern

i-Limb Grip	**Contact Sensor**	**Contact Sensor**
Lateral Grip	Thumb	Fore-finger
Modified Lateral Grip	Thumb	Middle-finger
Index Finger Point	Thumb	Ring-finger

Data illustrating the entire data flow from a user's grip selection to grip activation is shown bellow.

4.4.6.1 Intra-socket force Data

Data was collected over several experimental sessions. Intra-socket pressure data was extracted from .CSV format as described above. Analysis of this data showed that it was possible to detect forces applied to an area local to each sensor within the socket. Data was sampled every 10ms for a total of approximately 30 seconds. Hand Flexion and Extension movements were performed for approximately 3 seconds. Output data can be seen and is labeled in Figures 4.15(a), 4.15(b), and 4.15(c). Force output thresholds were tuned empirically based on comfortable exertion levels for the subject. These thresholds corresponded to a change in voltage above 3.1V for sensor 1 and above 1V for sensor 2. Sensor 1 corresponded to the sensor at the "top" of the arm, and corresponding to extension movements. Sensor 2, mounted to the "bottom" of the arm, corresponded to flexion movements. Response times of the Moving Average Filter are adjustable and can be set to allow for a more or less responsive classification, and therefor output, of the control signal to be sent to the i-Limb hand.

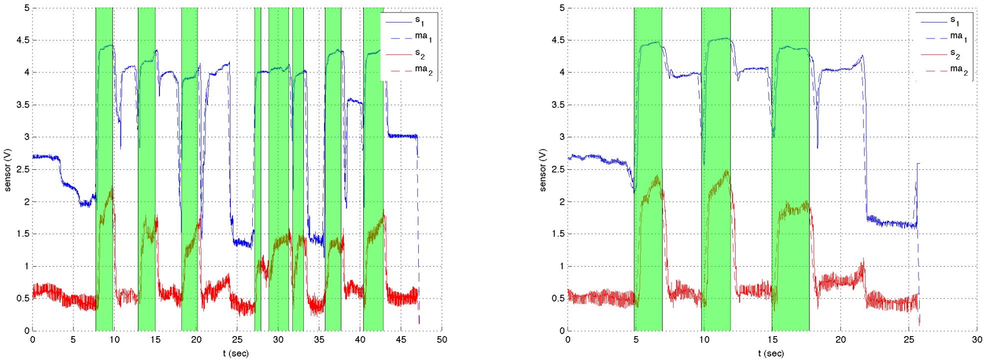

(a) Grip 1, “Lateral Grip”

(b) Grip 2, “Modified Lateral Grip”

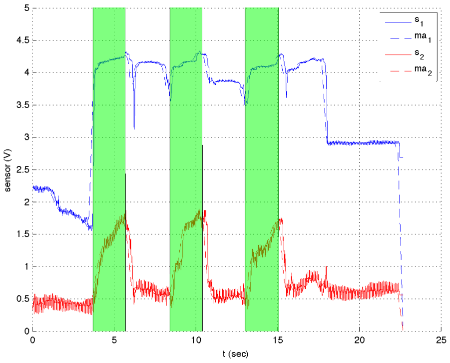

(c) Grip 3, “Index Finger Point”

Figure 4.15: Output of intra-socket force sensors during three grip strategies. Output from flexion motions presented here. Green areas correspond to times when both sensors detect values above threshold.

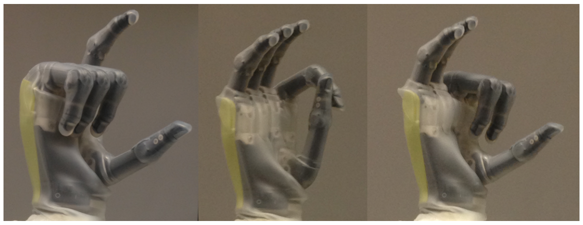

Figure 4.16: Prosthetic Device in each of the three closed grip configurations. Index Finger Point (Left) Lateral Grip (Middle) Modified Lateral Grip (Right)

In Figures 4.15(a),4.15(b), and 4.15(c), the time stamps highlighted in green show the times when both sensors are activated, ie. above their threshold values. Time stamps when sensor 1, s1, is activated are not highlighted but can be seen. The moving average, the classification filter, is listed as the dashed lines.

4.4.6.2 Grip Selection Data

As seen in the previous section and prior studies, we have shown that intra-socket force measurements can be made and can readily show high enough resolution to differentiate between activation of different forearm muscle groups. See Table 4.2. The activation pattern used to operate the i-Limb robotic hand is described previously in Sections 4.4.1 and 4.4.2 and a table outlining which grip pattern choices correspond to which grip outputs by the i-Limb hand can be seen in Table 4.3. Illustrations showing the "closed" positions for each of these grips can be seen in Figures 4.16. The "open" position for each of these grips was seen previously in Figure 4.14.

4.4.7 Usage Scenario Experiment

The two sets of data compared in Table 4.4 are based off of User Interface Method. Those columns listed under *Pinch Gesture* correspond to the input/ actions performed using the Contact Sensor Thimbles while the subject performed Pinch Gestures with their healthy-hand. Those columns listed under the column *Smart Phone Application* correspond to those grip-types selected using the subject's smart-phone. All time is reported in seconds. Statistical Measures are reported in Table 4.5.

4.4.8 Discussion

Similar moving average filters have been used in commercial prosthetic control systems [143] and have shown to have robust performance in a limited number of usage sce-

Table 4.4: Pinch Gesture and ForceMyography: Usage Experiment

Interface Method Comparison				
		Raw Data		
Pinch Gesture			**Smart Phone App.**	
Attempt	**Gesture**	**Time**	**Gesture**	**Time**
1	2	7.50	1	5.18
2	1	5.66	3	5.01
3	1	4.62	1	7.50
4	3	7.00	3	7.03
5	2	3.61	2	5.38
6	3	5.30	3	5.29
7	1	7.05	1	5.76
8	2	5.71	2	6.43
9	1	4.37	1	4.37
10	2	3.75	3	13.79
11	1	3.41	2	6.33
12	3	3.20	1	6.46

narios. The current classification system allows for open-loop control of the prosthetic device, similar to currently available commercial systems. Current prosthetic devices make use of motors and do not include encoders or other position sensing capabilities. The moving average filter, running on the myRIO system, functions in real-time. However, due to the non-real time nature of the Arduino microcontroller, which collects data “at best effort”, and the lag of the motor activity, both in the user’s muscle activation actions and the powered prosthetic device, we can not currently claim real-time control. The sampling window in the moving average algorithm is the determining factor for the speed of opening or closing switching signals. Of course, the response time of the hand’s motors, the physical system itself, is the true limiting factor for system responsiveness. That is to say that grip-selection, and therefore grip-selection switching, is dependent on the thresholding window of the algorithm. But, system response is more influenced by the motor’s response time in the hand.

Table 4.5: Pinch Gesture and ForceMyography: Statistical Measures

Raw Data		
	Pinch Gesture Time	**Smart Phone App. Time**
mean (μ)	5.10	6.54
stdev (σ)	1.51	2.45
max	7.50	13.79
min	3.20	4.37
median	4.96	6.05
μ **+1** σ	6.91	9.50
μ **-1** σ	3.28	3.60

As seen in the results section, in Figures 4.15(a), 4.15(b), and 4.15(c), it is possible to acquire data using off the shelf sensors. Figure 4.15(a) shows the output from both force sensors. It can be seen that at approximately 7 seconds, both sensors show an increase in voltage. This increase is proportional to the force applied to the sensor. As the subject's muscles are activated, resistance within the piezo-resistive sensor decreases. This allows for an increase in voltage, as seen in the corresponding rise of both the blue and red lines on the graphs. It should also be noted that starting at approximately 7 seconds, both sensors were activated. This corresponds to the i-Limb hand performing an "open" gesture. Immediately following, starting at about 10 seconds, sensor 2's voltage decreases while sensor 1's reading stays approximately the same. This reading corresponds to the i-Limb hand performing a "close" gesture. Outputs roughly alternate as the subject opens and closes the i-Limb hand throughout the trial. This is most readily seen in Figure 4.15(b) and 4.15(c).

Results of the Usage Scenario experiment do provide some insight in to the value of this system. Namely, it was found that the data were not statistically different (P=0.07) and took a comparable amount of time. That is to say that the raw data shows that the new input method using pinch-gestures made by the subject's healthy hand is at least as good as this current, commercially available system. When evaluating the data further, and removing

Table 4.6: Pinch Gesture and ForceMyography: Usage Experiment

Interface Method Comparison				
Outliers Removed				
Pinch Gesture			**Smart Phone App.**	
Attempt	**Gesture**	**Time**	**Gesture**	**Time**
1	2	**x**	1	5.18
2	1	5.66	3	5.01
3	1	4.62	1	7.50
4	3	**x**	3	7.03
5	2	3.61	2	5.38
6	3	5.30	3	5.29
7	1	**x**	1	5.76
8	2	5.71	2	6.43
9	1	4.37	1	4.37
10	2	3.75	3	**x**
11	1	3.41	2	6.33
12	3	3.20	1	6.46

outliers laying beyond 1.2 standard deviations for each input method, Pinch-Gesture vs. Smart-Phone, more compelling information can be seen. Table 4.6 reports this modified data set.

The adjusted data set shown in Table 4.7 indicates a further improvement in mean task completion time over the standard input method utilizing a smart-phone. It is thought that with an improved socket, further improvements of this interaction system will occur. It would be instructive to see the results of an experiment where the completion of a pinch-gesture automatically causes the robotic hand to close as this more closely resembles the functionality of the smart-phone based application's operation.

It was discovered during initial testing that individual activation of the muscles involved in flexion of the hand did not result in sufficient deflection of the force sensor. Future sensor placement considerations should not dismiss this site, however. Admittedly, the healthy-limb socket itself deflected more than expected. That is to say that the material

Table 4.7: Pinch Gesture and ForceMyography: Statistical Measures

Outliers Removed		
	Pinch Gesture Time	**Smart Phone App. Time**
mean (μ)	4.40	5.89
stdev (σ)	0.98	0.94
max	5.71	7.50
min	3.20	4.37
median	4.37	5.76
μ **+1** σ	5.38	6.83
μ **-1** σ	3.42	4.95

in that area may not have had a sufficient fit nor strength to illicit a more robust response. Improvement to socket fit and construction will be made in future work.

4.5 Conclusions

The described studies aimed to allow alternative control inputs to powered prosthetic devices. One method, identifying degraded surface-EMG signals due to linear displacement along a subject's arm from an ideal location is presented. Through a multi-modal sensing approach, unique at this time to the author's knowledge, control of a powered prosthetic device will be possible despite degraded EMG signals due to fatigue or socket displacement due to activities of daily living. This system increases robustness of prosthetic systems by allowing for socket movement while maintaining control input identification. This method also has shown that given basic training data created by a subject seated in a chair, a system of collocated surface EMG and FMG, and a basic neural network classifier performs better than a system trained using only SEMG data by at least 3% against data collected during arm movements found in daily life. An even more significant improvement was seen against data collected during times of subject fatigue and socket shift, 8% and 35% respectively. Additional and more complex training sets consisting of data gathered during shift of the prosthetic socket performs as well as, or better than, systems trained using data gathered during arm motions of daily living while standing. Should a user only be able to perform a single additional training data set, socket shift movements should be considered over arm movements with considerations for socket rotation. Insight in to classifying data gathered during times of user fatigue was gained. And although systems making use of additional training data outperformed systems including only basic training data during fatigued tasks, no information could be gained for tasks performed while a user was perspiring at this time. Further, while data during times of fatigue were not included in training sets, due to limitations of hardware and software restrictions, classification of data during times of fatigue were possible and did show improvements using the proposed system. Classification of radial and ulnar deviation of the wrist was shown to be possible, with a significant classification improvement of the SEMG-FMG system over the traditional SEMG only system. Future work will include implementation of DC offset compensation [62]. This should further improve the captured signals. Training using the recurrent neural network method, a more computationally intensive training algorithm, is considered impractical at this time but will be considered during future work. Other, more complex training algorithms will be considered and tasks designed to force a subject to exert themselves and cause perspiration will be performed. Another method, utilizing Force Myography as an activation signal controlling opening and closing a gripper was also described. This method allowed a user to define non-standard grip configurations using their sound hand, and then activate that grip choice using Force Myography.

Proposed work aims to improve performance of the SEMG and FMG system, through implementation of additional opposing SEMG-pressure sensor housings and increase in user grip-type identification. Increasing force-sensor array size will also be considered. Improvements to the classification algorithm will be necessary to make use of the additional user inputs available.

CHAPTER 5

Towards Optimal Placement of Accelerometers

5.1 Introduction

Modern feedback control methods allow for accurate manipulator positioning of robotic systems but require knowledge of the system in some manner, whether it is learned through an optimization or optimal control method or is fully described in advance. Central to this feedback is the need for sensors able to detect the current state of the system. Placement of those sensors in locations where they can provide the best possible information is necessary for accurate state data to be conveyed to the system's controller. The following sections describe the beginning of this optimization process through the use of the kinematic and dynamic descriptions of a two-link robot with two rotational degrees of freedom and introduction of noise in to the system through model uncertainties and sensor scaling effects. In these sections it is assumed that the robot is not equipped with joint-encoders and that accelerometers will be placed at defined locations along the link-lengths to provide acceleration information of both the first and second link in the kinematic chain.

This chapter is organized as follows: Section 5.2 discusses noise affects of accelerometers as seismic mass, as well as overall sensor size, decreases. Section 5.3 discusses the mathematical descriptions of a two-link manipulator using two separate methods. Section 5.4 outlines the algorithms to be implemented in an optimization study, including noise and model uncertainty.

5.2 Noise Considerations during Accelerometer Scaling

Owing to advances in manufacturing processes of MEMS devices in recent decades, inexpensive and relatively accurate sensors are allowing for improved control systems. Inertial measurement units (IMU), accelerometers, are now cheap and small enough to be placed at arbitrary locations on industrial and commercial robotics systems. As sensor footprints have shrunk with improved manufacturing processes, it has become important to study the effects of scaling features within the sensor itself. As a device becomes smaller, physical effects can affect the Signal-to-Noise Ratio (SNR) and Quality Factor. For this reason, it is important to first identify the limiting parameters within a particular sensor. The equations described below present the scaling effects acting on a seismic accelerometer as footprint size is reduced, focusing on SNR and Quality Factor.

Levinzon[102], whose notation is used below, describes the noise limit of a piezo-electric accelerometer in terms of the signal spectral densities and in turn, the Quality Factor. Of note, the electrical thermal noise was included. In previous work, due to overall effect of the mechanical-thermal noise with less sensitive accelerometers, this effect had been neglected[102]. In this work, we focus on the Quality Factor and how scaling effects influence noise. The SNR for a piezo-resistive accelerometer is:

$$\frac{Z_s^2}{Z_n^2} = \frac{a_s^2 m Q}{4 k_b T w_0} \tag{5.1}$$

where $Z_s^2, Z_n^2, a_s^2, m, Q, k_b, T, w_0$ are the signal response spectral density, noise response spectral density, input acceleration spectral density, Boltzman constant, mass of the accelerometer's seismic mass, Quality factor, temperature, and resonant frequency, respectively. The Quality factor term can be described as:

$$Q = \frac{m w_0}{b} \tag{5.2}$$

$$b = \frac{\mu A}{y_0} \tag{5.3}$$

where b is the damping coefficient, A is the area of the accelerometer's capacitive combs, y_0 is the separation distance between the combs. Couette Damping is assumed [144]. w_0 is the resonant frequency of the device and is defined, using the Boltzman constant and the accelerometer's seismic mass as:

$$w_0 = \sqrt{\frac{k}{m}} \tag{5.4}$$

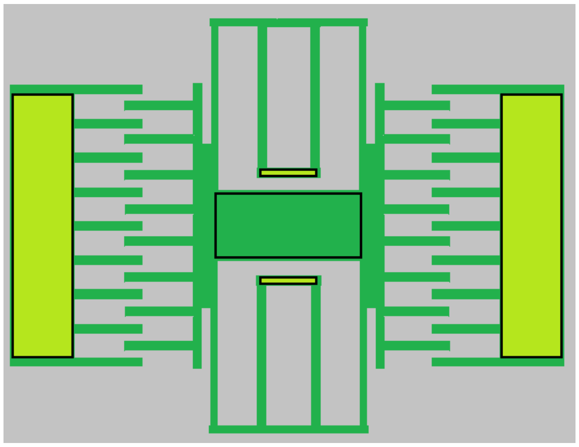

Figure 5.1: Example of interdigitated accelerometer features. Seismic mass outlined in black

It is assumed that the seismic mass is much larger than the combined masses of the seismic mass's trusses and beams, the shuttle's trusses and beams. That is to say that $m_S \gg \frac{m_T}{4} + \frac{12 m_B}{35}$. From these definitions and through algebraic simplification, the scaling equation follows:

$$SNR = \frac{Z_s^2}{Z_n^2} = \frac{a_s^2 y_0 m^2}{4 k_b T \mu A} \tag{5.5}$$

An example of the features described can be seen in Figure 5.1. The seismic mass can be seen outlined in black. The shuttle's trusses, beams, and interdigitated capacitive combs can be seen in green. Anchor points are seen in yellow. The acceleration spectral density (ASD) can be thought of as a power spectral density, the power distribution over the frequency range of excitation, and can therefor be considered constant within a defined frequency range. The remaining constant terms in the numerator and denominator (the temperature, T, comb separation distance, y_0, Boltzman's constant, k_b, and fluid viscosity, μ) allow one to see that the Signal-to-Noise Ratio scales proportionally with the square of the mass, m^2, and inversely with the area, A. Through further cancellation, due to constant thickness and an assumption of scaled feature width, the order of scaling of an accelerometer's signal-to-noise ratio is on the order, $O(L)$. That is to say that it is proportional to the feature length and scales linearly. Optimization of feature size parameters for a given accelerometer footprint needs to be considered in future work.

5.3 Simulation of Two-link Arm

A two-link planar robot is studied as part of a sensor optimal placement problem. The robot's joint-angles are described using the familiar Dynamics and Kinematic equations. Current progress on a Matlab simulation is presented. An alternative method to derive the elbow-joint angle is also considered, making use of Rotation Matrices between projected sensor data and trigonometric relationships.

5.3.1 Kinematics

One method of determining a robot's end-effector position in space is by using the robot's joint-angles. In the event that a particular robot is not equipped with joint-encoders, it is possible to determine end-effector position in space by comparing relative acceleration of positions on the robot's link lengths. The equation describing the end-effector position of a two-link planar robot, via the robot's descriptive Jacobian equation, is:

$$\dot{x} = J_a(q)\dot{q} \tag{5.6}$$

where $\dot{x}$ is the x-y velocity vector of a location on the robot, usually the end-effector, $\dot{q}$ is a vector containing the joint angle velocities, and $J_a(q)$ is the robot Jacobian. The acceleration of the system can be found via differentiation. Note, the (q) notation in $J_a(q)$ will be left out for simplicity moving forward.

$$\ddot{x} = J_a\ddot{q} + (\frac{d}{dt}J_a)\dot{q} \tag{5.7}$$

In order to include arbitrary adjustments to the position of an accelerometer along a link, changes to the J_a and $\dot{J}_a$ equations are necessary. Here, we assume an even distribution of accelerometers along the length of each link. This allows for adjustment of J_a and $\dot{J}_a$, for our two-link robot, as:

$$J_a = \begin{bmatrix} -l_1 r s(\theta_1) & 0 \\ l_1 r c(\theta_1) & 0 \\ -l_1 s(\theta_1) - l_2 r s(\theta_{1,2}) & -l_2 r sin(\theta_{1,2}) \\ l_1 c(\theta_1) + l_2 r c(\theta_{1,2}) & l_2 r c(\theta_{1,2}) \end{bmatrix} \tag{5.8}$$

$$\dot{J}_a = \begin{bmatrix} -l_1 r\dot{\theta}_1 c(\theta_1) & 0 \\ -l_1 r\dot{\theta}_1 s(\theta_1) & 0 \\ -l_1\dot{\theta}_1 c(\theta_1) - l_2 r(\dot{\theta}_{1,2})c(\theta_{1,2}) & -l_2 r(\dot{\theta}_{1,2})c(\theta_{1,2}) \\ -l_1\dot{\theta}_1 s(\theta_1) - l_2 r(\dot{\theta}_{1,2})s(\theta_{1,2}) & -l_2 r(\dot{\theta}_{1,2})s(\dot{\theta}_{1,2}) \end{bmatrix} \tag{5.9}$$

The terms $s(\theta)$ and $c(\theta)$ refer to the *sin* and *cosine* functions. $\theta_{1,2}$ is the angle $\theta_1 + \theta_2$. The scaling term, m, is used to place accelerometers at arbitrary, but equally spaced, locations along the robot links. This can be done using a series of calculations of J_a & $\dot{J}_a$, where

$$r = n/j$$

n and j are counter variables. n is the current accelerometer number and j is the total number of accelerometers per link. This scaling factor, r, allows a user to place an arbitrary number of accelerometers at equally spaced locations along the robot links. More discussion of this will occur below, in section 5.4.1.

5.3.2 Dynamics

It is also possible to solve the dynamical equations of a robot arm for acceleration:

$$\ddot{q} = M^{-1}(\tau - N(q, \dot{q})) \tag{5.10}$$

where $N(q, \dot{q})$ contains the velocity, gravity, and force terms of the dynamical equation. From these two equations, equations (5.7) and (5.10), one is able to determine an *expected* angular acceleration based off of the robot's dynamics and then use this value to solve for an expected acceleration, and through integration with respect to time, velocity, and position via the robot's Jacobian.

Standard methods to determine position of a robotic manipulator from accelerometry data require integration in order to determine velocity and then integration of velocity data to determine position. Numerically integrating acceleration data, twice, introduces mathematical errors at each integration step. These errors build up and induce instabilities in systems over a short time period. An accepted method to address these integration errors makes use of an Extended Kalman Filter, in combination with a sensor that is not an accelerometer.

In order to study these integration errors and noise scaling issues, simulations that include accelerometry data have been written and run.

5.4 Simulation Study

Initial studies have been conducted to simulate the Jacobian and Dynamical equations describing a two-link planar robot, ie two-link with two degrees of freedom. The Matlab ordinary differential equation solver, ode45, is used to solve for joint-angles and velocity as outlined above. These angles and velocities are saved, and are then used to solve for the positions at defined locations along the link-length. *ode45* is utilized again, but, instead of using the in-built function within *ode45* to define incremental joint-angles to be inserted in to equation (5.7), the joint-angles and velocities solved for previously using equation (5.10) are utilized. In this way, Matlab is able to calculate the x-y positions along the link-length using angular accelerations as the known value. The simulation increases the number of accelerometer sensors per link-length per simulation in order to study RMS error as the number of accelerometers are increased. Initial results indicate that a reduction in Root Mean Squared Error is seen as additional sensors are added to the end of each link of a simulated two-link system.

5.4.1 Noise

Noise considerations are included during simulation. Signal to Noise Ratio (SNR) of the accelerometers was scaled according to the accelerometer's foot-print and are accounted for in order to include the findings in section 5.2. This was accomplished by scaling proportionally to "$1/n$" where "n" is the number of accelerometers per link-length. That is to say that we assume that the number of accelerometers per link of the robot arm are of equal size and that that size is proportional to the length of the accelerometer foot-print. Then the SNR for each accelerometer is multiplied by a factor of "$1/n$", where "n" is the *"number of accelerometers per link"*. This scaling of the SNR, to account for size of the sensor's footprint is multiplied by the angular acceleration data found via the Dynamic equations. Model uncertainties were also included in these simulations. These are included as random variations in the link-lengths and acceleration values, multiplying these values by the user defined values and the Matlab function *rand*, used to solve equation (5.7).

5.4.2 Root Mean Squared Error

Currently, Root-Mean-Squared-Error (RMSE) is used to measure the estimation error between the Dynamical and Kinematic equations. Without the modeled noise added to the system as described in section 5.4.1, integration errors are seen. The RMSE between the two systems is determined from calculated angular acceleration found from the Dynamical equations as compared to the angular accelerations found from the Jacobian. It should be noted that finding the position, through double integration of equation (5.7), will introduce a small amount of error. Other sources of error will include rounding errors during calculations from the ode45 Matlab function and note of these errors, while small, will be seen in the RMSE, as well.

The two-link system discussed above was simulated, and the RMSE was recorded over a series of trials. This RMSE calculation is seen below in Equation 5.11.

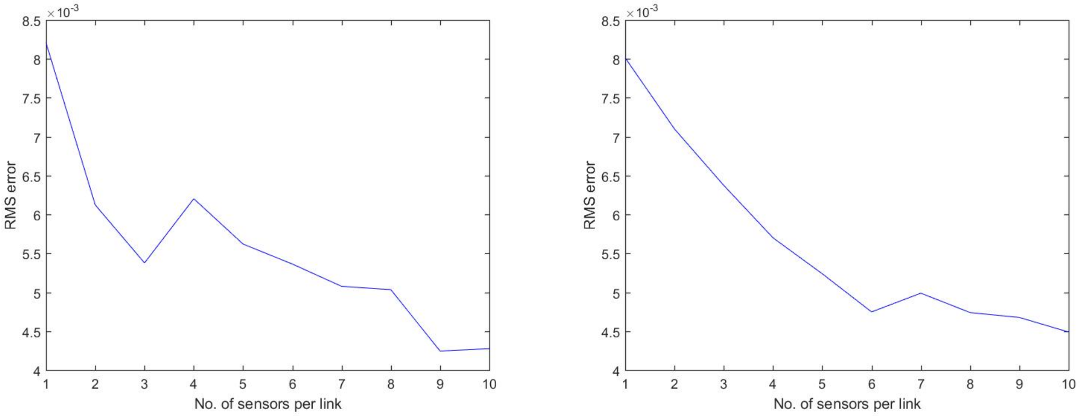

(a) (b)

Figure 5.2: Output of Simulated Study of two-link system joint angle error. RMSE reported for two separate simulations as the number of accelerometers are increased at the end of each link.

$$E_i = RMSE = \sqrt{\sum_{t=1}^{n} \frac{(e_t - \bar{e}_t)^2}{n}} \tag{5.11}$$

$$n = \left[Z_{\frac{\alpha}{2}} \frac{S}{me} \right]^2 \tag{5.12}$$

From this, a Monte-Carlo simulation was run to compare E_i, the RMSE, from each category. Here, n is the number of Monte Carlo simulations run, determined in Equation 5.12, where S is the estimated standard deviation and me is the required margin of error. $Z_{fraq\alpha 2}$ is given a value of 1.96 for a 95% confidence interval. Equation 5.11 returns the average error over n simulations at different times. Initial results indicate that a reduction in Root Mean Squared Error is seen as additional sensors are added to the end of each link of a simulated two-link system. The simulation was run for 1 to 10 accelerometers per link, and 100 times for each number of sensors, for a total of 1000 trials. The RMSE was compared over time to analyze any trends. This simulation was conducted twice, and output can be seen in Figure 5.2(a) and 5.2(b). A decreasing trend can be seen in RMSE as additional sensors are included.

The error values for subsequent cases were analyzed using this method as well. These cases, with RMSE listed, were:

1. 2 accelerometers per link
   (a) Both accelerometers attached at the end of the links - RMSE: error of 0.13
   (b) One accelerometer attached at the end of the link and the other at the mid-point of the link - RMSE: 0.17
   (c) Both accelerometers attached at the mid-point of the link - RMSE: 0.6
2. 2 accelerometers total
   (a) One accelerometer per link attached at the end of the links - RMSE: error of 0.01
   (b) Both accelerometers attached at the end-point of the second link - RMSE: error of 0.69
3. Several accelerometers placed at equal distances along both links (RMSE presented below)
   (a) 1-4 accelerometers per link with a maximum SNR of 60dB, found through scaling the accelerometer size at $1/n$ where n is the number of accelerometers, and 0 model uncertainty

(b) 1-4 accelerometers per link with 0 noise and up to 10% model uncertainty

(c) 1-4 accelerometers per link with SNR of 60dB and 0 model uncertainty

(d) 1-4 accelerometers per link with 0 noise and 0 model uncertainty

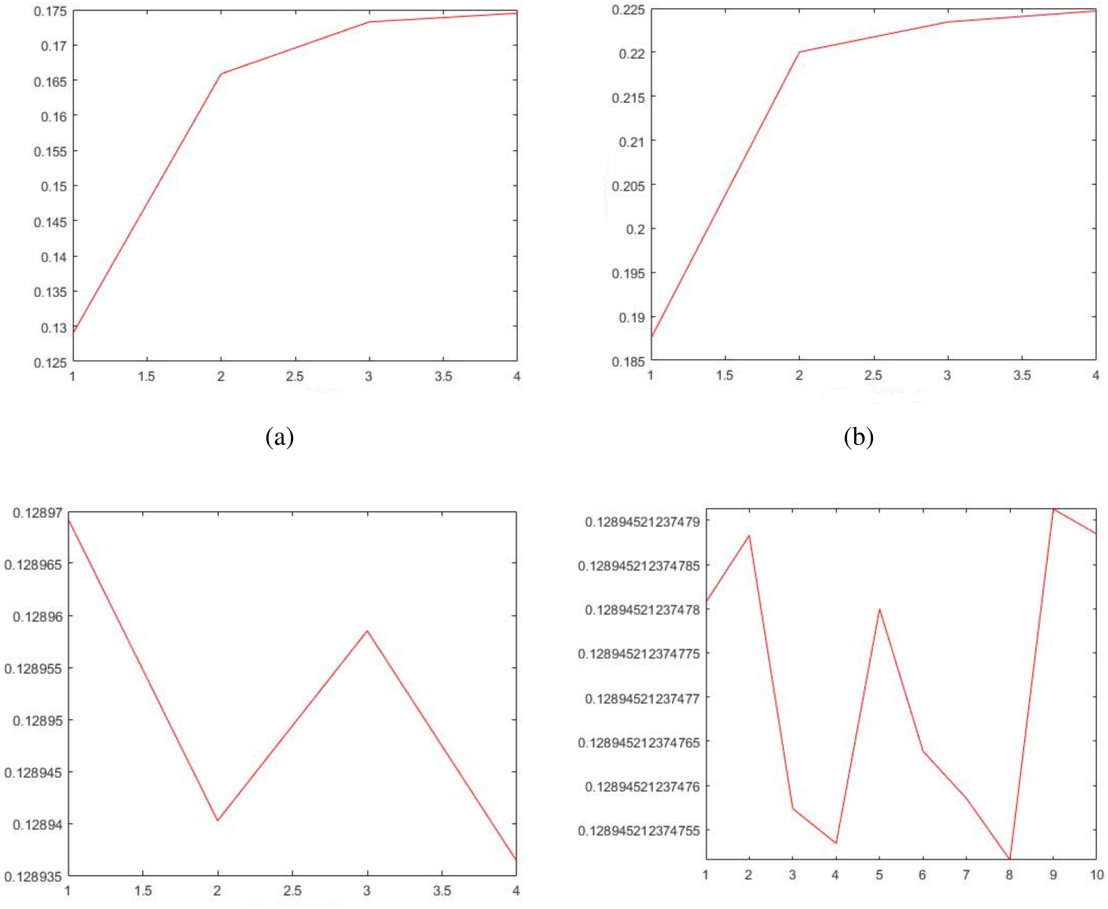

(a)

(b)

(c)

(d)

Figure 5.3: Output of Simulated Study of two-link system joint angle error. RMSE vs Number of Sensors. RMSE reported for the four separate simulations of a) 1-4 accelerometers per link with a maximum SNR of 60dB, calculated via scaling, and 0 model uncertainty b) 1-4 accelerometers per link with 0 noise and up to 10% model uncertainty c) 1-4 accelerometers per link with SNR of 60dB and 0 model uncertainty d) 1-4 accelerometers per link with 0 noise and 0 model uncertainty.

These results seem to indicate that some general conclusions can be made. These include that locating the accelerometers at the end of the link-lengths reduces the over-all error, as compared to the middle of the link-lengths. In addition, it can be seen that placing the accelerometers on all links reduces the error as opposed to placing all accelerometers on only one link. The RMSE error increases and seems to approach a maximum value when placing additional accelerometers along the link-length equidistantly, when SNR is scaled to accelerometers size at $1/n$ or Model Uncertainty is introduced Figures 5.3(a) and 5.3(b). When the SNR is fixed at 60dB, the RMSE exhibits a downward trend as additional accelerometers are placed equidistantly along the link-length Fig. 5.3(c). When no noise is introduced to the system, the RMSE trend is indeterminate Fig 5.3(d).

5.5 Conclusions

This chapter presented the current status of ongoing research to find the optimal placement and number of accelerometer sensors on a multi-link robot for use in determining joint-angle position without the need for internal encoders or other sensors. At this time, an optimal placement for a sensor is not found nor is an optimal number of accelerometers reported. Noise, based on the Signal-to-Noise Ratio, is introduced as well as Model Uncertainty. Root-Mean-Square Error was used as a method of reporting resulting data. Additional accelerometers located at the end point of the link-lengths reduces RMSE. Additionally, a downward trend in RMSE can be seen when additional accelerometers are placed, either equidistantly along the link-lengths or at the end-point of the link, when model uncertainty and noise are considered. No trend in RMSE is seen when no noise is included.

CHAPTER 6

Conclusion and Future Work

6.1 Conclusion

A series of studies whose goal was to inform and provide insight in to physical human-robot interaction were undertaken. These studies initially focused on determining required sensor performance ranges, human grip-type, and wrist-joint angles during activities of daily living. Continued studies expanded on these data and found that wrist velocity prior to contact with an object is a valid input for determining intent after contact was made. A series of machine learning techniques were applied to clinically gathered data and recommendations for future intent classifiers were made.

These fundamental studies led to work involving improvements to inputs to powered prosthetic sockets. Heterogeneous sensor arrays were developed, adding force myography inputs to the standard surface EMG sensors. A multi-layer perceptron neural network was used to provide data classification. Studies towards improving a two-link system's configuration estimate using accelerometry data were begun.

6.1.1 Measurements of Physical Interactions between Humans and Objects of Daily Living

Clinical studies involving measurements of human interaction forces and joint angles during manipulation of objects of daily living were undertaken. A cohort of subjects interacted with a weighted cylinder and weighted door, while donning a pressure sensitive glove and retro-reflective markers for motion capture, in order to determine sensor performance limits needs. Fundamental grip patterns were determined while also determining necessary sensor placement for positive grip-type identification. Wrist-joint deviation angle ranges during manipulation of a weighted cylinder were also measured. This information is intended to inform future safe physical-human robot interaction studies and implementations as well as the development of sensorized robotic skin.

6.1.2 Wrist Velocity Classification for Human Intent Detection

In addition to grip pressure and wrist-joint angle measurements, wrist velocity measurements during manipulation of objects of daily living were gathered. Human intent detection prior to contact with a weighted cylinder was found to be possible, using only the measured wrist velocity profile of a subject. These wrist velocity measurements were used to train a series of classifiers, using a series of fundamental machine learning techniques. A series of classifiers were produced and used to classify wrist velocity profiles from a unique group of subjects. Determination of minimum frame-capture rate for positive classification was made. Additionally, deployment to a real system, using off-the-shelf hardware and custom software was undertaken. Classification error rates were found and followed predicted values based on previous calculations using simulation.

6.1.3 EMG and EMG-FREE Control of a Powered Prosthetic Device

Studies involving the improvement of control and interaction of powered prosthetic devices using heterogeneous sensor arrays occurred. Correlation between data from Surface EMG sensors and intrasocket force sensors, using Force Myography, was determined. This correlation was used to study user intent detection during times of non-ideal sensor placement and poor socket fit. A series of multi-layer perceptron neural network classifiers were trained using data gathered during several arm and socket configurations. The results of the error classification rates were compared and recommendations for data to include during classifier training were made in the literature. A custom-fit prosthetic socket simulator was also developed for use by a healthy-limbed individual.

6.1.4 Towards Optimal Placement of Accelerometers on a two-link system

Work was begun towards developing algorithms to determine optimal placement of accelerometers on a two-link system in a two-dimensional space. Scaling studies focused on an accelerometer's seismic mass were conducted. Signal noise was found to increase linearly as the seismic mass's edge decreased in length. Following this, joint angle RMS error rate data was gathered from simulated two-link systems. Several simulations were calculated with between 1 and 10 accelerometers were placed at the end-joint of each simulated link of the two-link system. RMS error was found to decrease as the numbers of accelerometers increased on each link.

6.2 Future Work

Future work will involve expanding joint-angle estimation using accelerometers and expanding work in the field of powered-prosthetic devices.

6.2.1 Towards Optimal Placement of Accelerometers on a two-link system

Future work will vary the placement of the acccelerometers along the link length in simulation, and introduce noise to the both the sensor readings and the model description. The ability to adjust the seismic mass, in order to simulate changes in the size of the accelerometer package, will be included. Simulation will be expanded to include optimal sensor placement on an n-Degree of Freedom arbitrary robot, moving in three dimensions.

6.2.2 Development of a Powered Prosthetic Socket using a Heterogeneous Sensor Array

Current work using an SEMG-FMG sensor array to provide input to a powered prosthetic socket will be expanded to include accelerometry data. Accelerometers will be used to improve intent detection to include “context aware” grip-selection. Improvements to the classification algorithm will be made and deployment to a secondary-prototype will be made. Studies involving a trans-radial amputee and powered prosthetic user will also be conducted.

6.2.3 Improvements to Intent Detection During Physical Human Robot Interaction Scenarios

Although deployment to a real system has occurred, and initial software for intent detection has been produced, performance is limited. Robustness of the system needs to be improved and deployment using a robotic system, such as a PR2 robot(by Willow Garage), should occur. Expansion to include online learning algorithms, such as neuro-adaptive control, will be undertaken with the goal of updating system impedance during interaction.

CHAPTER 7

Aggregated Cohort Data: Activities of Daily Living

In this appendix, we present Data for the Grip-Pressure During Activities of Daily Living Experiments described in Chapter 3.1.3.

Table 7.1: Aggregated Cohort (Female) Data for action: Door 6lb Pull - kPa

Pull Door: 6lbs

Sensor Segment	**Subject 1**	**Subject 2**	**Subject 3**	**Subject 5**	**Subject 7**
Thumb Distal	99	24	62	53	40
Thumb Proximal	57	23	31	11	48
Fore-finger Distal	109	222	108	84	133
Fore-finger Intermediary	17	46	30	34	57
Fore-finger Proximal	16	49	29	23	29
Middle-finger Distal	100	110	100	96	97
Middle-finger Intermediary	38	24	33	55	43
Middle-finger Proximal	26	32	18	18	9
Ring-finger Distal	290	189	117	147	232
Ring-finger Intermediary	99	33	41	27	89
Ring-finger Proximal	298	36	18	27	94
Pinky Distal	238	101	32	13	61
Pinky Intermediary	194	101	60	15	65
Pinky Proximal	456	89	88	15	38
Thenar	107	118	60	169	71
Hyper-Thenar 1	78	119	74	61	83
Hyper-Thenar 2	24	154	67	78	30
Metacarpal Head	68	158	132	66	66
Sum	**2314**	**1628**	**1100**	**992**	**1285**

Table 7.2: Aggregated Cohort (Male) Data for action: Door 6lb Pull - kPa

Pull Door: 6lbs

Sensor Segment	**Subject 6**	**Subject 8**	**Subject 10**	**Subject 11**	**Subject 12**
Thumb Distal	151	32	30	65	81
Thumb Proximal	45	102	10	40	72
Fore-finger Distal	79	272	291	216	307
Fore-finger Intermediary	32	193	505	51	104
Fore-finger Proximal	22	129	19	56	72
Middle-finger Distal	174	162	296	93	99
Middle-finger Intermediary	59	40	178	38	69
Middle-finger Proximal	22	24	257	34	25
Ring-finger Distal	135	107	130	185	167
Ring-finger Intermediary	73	78	79	136	90
Ring-finger Proximal	48	101	83	148	72
Pinky Distal	210	91	334	76	58
Pinky Intermediary	44	69	386	53	50
Pinky Proximal	15	12	223	25	21
Thenar	25	182	228	41	18
Hyper-Thenar 1	102	252	241	117	98
Hyper-Thenar 2	19	319	72	23	59
Metacarpal Head	73	221	755	127	152
Sum	**1328**	**2386**	**4117**	**1524**	**1614**

Table 7.3: Aggregated Cohort (Female) Data for action: Door 6lb Push - kPa

Push Door: 6lbs

	Subject 1	**Subject 2**	**Subject 3**	**Subject 5**	**Subject 7**
Sensor Segment					
Thumb Distal	154	81	113	113	116
Thumb Proximal	25	6	43	86	122
Fore-finger Distal	105	95	46	41	47
Fore-finger Intermediary	11	63	18	23	29
Fore-finger Proximal	21	116	11	18	16
Middle-finger Distal	139	83	69	46	117
Middle-finger Intermediary	17	23	17	14	19
Middle-finger Proximal	34	21	19	18	7
Ring-finger Distal	238	99	79	69	400
Ring-finger Intermediary	72	34	18	15	74
Ring-finger Proximal	199	40	19	20	54
Pinky Distal	274	101	55	15	92
Pinky Intermediary	56	167	59	20	34
Pinky Proximal	149	77	56	11	42
Thenar	39	25	65	456	17
Hyper-Thenar 1	341	302	82	91	347
Hyper-Thenar 2	153	117	8	27	290
Metacarpal Head	41	119	173	137	64
Sum	**2068**	**1569**	**950**	**1220**	**1887**

Table 7.4: Aggregated Cohort (Male) Data for action: Door 6lb Push - kPa

Push Door: 6lbs

	Subject 6	**Subject 8**	**Subject 10**	**Subject 11**	**Subject 12**
Sensor Segment					
Thumb Distal	210	78	103	170	95
Thumb Proximal	233	67	9	330	54
Fore-finger Distal	48	150	619	64	279
Fore-finger Intermediary	24	86	145	43	96
Fore-finger Proximal	16	236	120	40	96
Middle-finger Distal	137	105	344	72	93
Middle-finger Intermediary	46	24	152	30	67
Middle-finger Proximal	26	12	196	18	27
Ring-finger Distal	109	123	135	168	131
Ring-finger Intermediary	78	75	42	92	81
Ring-finger Proximal	34	46	50	109	50
Pinky Distal	172	95	26	97	50
Pinky Intermediary	82	36	51	70	15
Pinky Proximal	17	7	214	34	19
Thenar	16	100	65	301	14
Hyper-Thenar 1	105	800	1230	303	157
Hyper-Thenar 2	126	700	747	373	177
Metacarpal Head	45	221	157	73	329
Sum	**1524**	**2961**	**4405**	**2387**	**1830**

Table 7.5: Aggregated Cohort (Female) Data for action: Door 11lb Pull - kPa

Pull Door: 11lbs

	Subject 1	**Subject 2**	**Subject 3**	**Subject 5**	**Subject 7**
Sensor Segment					
Thumb Distal	31	76	46	47	77
Thumb Proximal	17	18	27	9	167
Fore-finger Distal	63	313	94	63	149
Fore-finger Intermediary	4	49	26	29	63
Fore-finger Proximal	5	49	24	22	31
Middle-finger Distal	51	95	135	53	82
Middle-finger Intermediary	21	30	51	52	51
Middle-finger Proximal	11	22	29	19	9
Ring-finger Distal	38	172	171	80	282
Ring-finger Intermediary	18	34	25	16	69
Ring-finger Proximal	28	40	23	31	183
Pinky Distal	35	143	105	11	126
Pinky Intermediary	5	95	66	15	42
Pinky Proximal	40	101	80	13	54
Thenar	15	122	88	152	61
Hyper-Thenar 1	8	122	98	98	60
Hyper-Thenar 2	4	125	132	78	26
Metacarpal Head	12	132	58	56	73
Sum	**406**	**1738**	**1278**	**844**	**1605**

Table 7.6: Aggregated Cohort (Male) Data for action: Door 11lb Pull - kPa

Pull Door: 11lbs

	Subject 6	**Subject 8**	**Subject 10**	**Subject 11**	**Subject 12**
Sensor Segment					
Thumb Distal	143	31	52	355	320
Thumb Proximal	49	115	11	60	113
Fore-finger Distal	79	265	373	245	339
Fore-finger Intermediary	27	114	316	69	80
Fore-finger Proximal	16	57	0	67	108
Middle-finger Distal	153	158	318	165	94
Middle-finger Intermediary	60	36	170	41	66
Middle-finger Proximal	23	15	187	25	34
Ring-finger Distal	99	167	84	268	176
Ring-finger Intermediary	56	69	67	129	95
Ring-finger Proximal	21	83	64	197	63
Pinky Distal	119	76	317	57	50
Pinky Intermediary	26	36	292	55	41
Pinky Proximal	14	24	180	32	30
Thenar	16	64	288	301	25
Hyper-Thenar 1	91	338	125	1096	161
Hyper-Thenar 2	22	348	63	303	98
Metacarpal Head	61	158	755	163	160
Sum	**1075**	**2154**	**3662**	**3628**	**2053**

Table 7.7: Aggregated Cohort (Female) Data for action: Door 11lb Push - kPa

Push Door: 11lbs

	Subject 1	**Subject 2**	**Subject 3**	**Subject 5**	**Subject 7**
Sensor Segment					
Thumb Distal	50	76	154	71	119
Thumb Proximal	16	32	56	82	62
Fore-finger Distal	25	95	83	43	35
Fore-finger Intermediary	5	53	66	16	25
Fore-finger Proximal	6	141	56	14	16
Middle-finger Distal	29	91	146	36	149
Middle-finger Intermediary	24	21	37	14	20
Middle-finger Proximal	9	18	137	15	8
Ring-finger Distal	29	90	171	51	519
Ring-finger Intermediary	17	37	54	13	79
Ring-finger Proximal	14	34	71	16	109
Pinky Distal	17	89	80	13	138
Pinky Intermediary	6	66	85	18	34
Pinky Proximal	11	60	120	10	42
Thenar	3	27	108	582	19
Hyper-Thenar 1	9	142	125	81	124
Hyper-Thenar 2	4	219	16	30	147
Metacarpal Head	14	179	179	120	57
Sum	**288**	**1470**	**1744**	**1225**	**1702**

Table 7.8: Aggregated Cohort (Male) Data for action: Door 11lb Pull - kPa

Push Door: 11lbs

	Subject 6	**Subject 8**	**Subject 10**	**Subject 11**	**Subject 12**
Sensor Segment					
Thumb Distal	263	70	96	340	306
Thumb Proximal	235	68	14	310	72
Fore-finger Distal	39	57	164	91	430
Fore-finger Intermediary	24	100	208	67	96
Fore-finger Proximal	16	186	120	37	72
Middle-finger Distal	139	60	344	135	103
Middle-finger Intermediary	60	42	126	25	47
Middle-finger Proximal	24	46	191	13	30
Ring-finger Distal	95	87	156	380	230
Ring-finger Intermediary	106	84	38	146	54
Ring-finger Proximal	26	55	51	180	59
Pinky Distal	182	38	69	161	198
Pinky Intermediary	49	26	69	110	22
Pinky Proximal	13	0	214	72	0
Thenar	25	173	68	306	18
Hyper-Thenar 1	102	743	492	327	291
Hyper-Thenar 2	129	1086	665	295	622
Metacarpal Head	26	576	145	99	441
Sum	**1553**	**3497**	**3230**	**3094**	**3091**

Table 7.9: Average Values over Cohort (kPa) by Sensor Segment per Action (Average: $\overline{x}$, Standard Deviation: σ)

	Push Door: 3lbs		**Pull Door: 3lbs**	
	$\overline{x}$	σ	$\overline{x}$	σ
Thumb Distal	**95.20**	31.01	**74.20**	35.33
Thumb Proximal	**49.90**	25.99	**36.70**	33.88
Fore-finger Distal	**78.80**	83.48	**222.50**	162.75
Fore-finger Intermediary	**67.60**	82.27	**69.40**	56.77
Fore-finger Proximal	**57.00**	68.50	**55.70**	37.78
Middle-finger Distal	**107.20**	120.53	**128.30**	94.67
Middle-finger Intermediary	**39.00**	45.62	**60.30**	54.32
Middle-finger Proximal	**33.30**	51.15	**44.70**	70.33
Ring-finger Distal	**124.00**	101.33	**134.30**	52.35
Ring-finger Intermediary	**59.20**	46.07	**69.40**	33.61
Ring-finger Proximal	**58.70**	46.71	**73.60**	43.98
Pinky Distal	**93.40**	116.62	**118.50**	123.97
Pinky Intermediary	**59.40**	43.52	**99.60**	119.53
Pinky Proximal	**53.10**	51.26	**79.60**	81.11
Thenar	**133.60**	214.38	**112.70**	88.62
Hyper-Thenar 1	**292.60**	345.52	**213.00**	279.19
Hyper-Thenar 2	**280.70**	367.50	**86.60**	73.32
Metacarpal Head	**189.40**	216.49	**183.90**	216.39

	Push Door: 6lbs		**Pull Door: 6lbs**	
	$\overline{x}$	σ	$\overline{x}$	σ
Thumb Distal	**123.30**	42.11	**63.70**	38.82
Thumb Proximal	**97.50**	105.62	**43.90**	28.29
Fore-finger Distal	**149.40**	180.36	**182.10**	89.31
Fore-finger Intermediary	**53.80**	43.34	**106.90**	149.13
Fore-finger Proximal	**69.00**	73.15	**44.40**	34.90
Middle-finger Distal	**120.50**	84.02	**132.70**	64.31
Middle-finger Intermediary	**40.90**	42.32	**57.70**	44.30
Middle-finger Proximal	**37.80**	56.11	**46.50**	74.31
Ring-finger Distal	**155.10**	98.61	**169.90**	56.74
Ring-finger Intermediary	**58.10**	28.10	**74.50**	33.28
Ring-finger Proximal	**62.10**	54.23	**92.50**	82.27
Pinky Distal	**97.70**	76.54	**121.40**	104.06
Pinky Intermediary	**59.00**	43.46	**103.70**	110.23
Pinky Proximal	**62.60**	68.00	**98.20**	141.42
Thenar	**109.80**	148.82	**101.90**	71.86
Hyper-Thenar 1	**375.80**	366.82	**122.50**	67.95
Hyper-Thenar 2	**271.80**	261.95	**84.50**	91.70
Metacarpal Head	**135.90**	90.08	**181.80**	207.80

	Push Door: 11lbs		**Pull Door: 11lbs**	
	$\overline{x}$	σ	$\overline{x}$	σ
Thumb Distal	**154.50**	108.02	**117.80**	120.54
Thumb Proximal	**94.70**	98.11	**58.60**	54.86
Fore-finger Distal	**106.20**	120.96	**198.30**	122.14
Fore-finger Intermediary	**66.00**	59.68	**77.70**	89.61
Fore-finger Proximal	**66.40**	62.56	**37.90**	32.90
Middle-finger Distal	**123.20**	89.59	**130.40**	78.10
Middle-finger Intermediary	**41.60**	32.91	**57.80**	41.73
Middle-finger Proximal	**49.10**	62.89	**37.40**	53.13
Ring-finger Distal	**180.80**	156.87	**153.70**	79.93
Ring-finger Intermediary	**62.80**	41.52	**57.80**	36.16
Ring-finger Proximal	**61.50**	50.43	**73.30**	64.84
Pinky Distal	**98.50**	67.70	**103.90**	86.23
Pinky Intermediary	**48.50**	33.33	**67.30**	83.03
Pinky Proximal	**54.20**	68.12	**56.80**	51.77
Thenar	**132.90**	183.79	**113.20**	105.44
Hyper-Thenar 1	**243.60**	226.21	**219.70**	319.79
Hyper-Thenar 2	**321.30**	357.55	**119.90**	116.92
Metacarpal Head	**183.60**	183.36	**162.80**	214.80

Table 7.10: Average Values over Cohort (kPa) by Sensor Segment per Action: 3lb Cylinder. Top: Finger Tip. Bottom: Whole Hand. (Average:$\bar{x}$, Standard Deviation: σ)

	Push		**Pull**		**Lift**	
	Finger Tip					
	$\bar{x}$	σ	$\bar{x}$	σ	$\bar{x}$	σ
Thumb Distal	**140.4**	123.97	**101.9**	81.08	**209.3**	112.94
Fore-finger Distal	**97.7**	88.12	**95.2**	62.35	**132.2**	69.67
Middle-finger Distal	**85.3**	88.54	**106.9**	97.80	**141.9**	90.49
Ring-finger Distal	**80.1**	28.74	**107.1**	63.56	**157.7**	81.19
Pinky Distal	**95.3**	74.37	**88.5**	60.09	**109**	63.89
Thenar	**40.1**	24.48	**35.6**	29.80	**38.1**	20.02
Hyper-Thenar 1	**62.6**	50.79	**56.6**	66.24	**39.8**	42.74
Hyper-Thenar 2	**109.1**	91.68	**114.6**	149.09	**52**	36.08
Metacarpal Head	**23.8**	7.28	**24.8**	14.49	**31.5**	25.32

	Push		**Pull**		**Lift**	
	Whole Hand					
	$\bar{x}$	σ	$\bar{x}$	σ	$\bar{x}$	σ
Thumb Distal	**150.5**	114.63	**97.1**	91.91	**134.3**	85.11
Fore-finger Distal	**95.5**	80.46	**86.5**	65.42	**112.9**	90.88
Middle-finger Distal	**93**	105.47	**102.3**	81.98	**118.7**	72.34
Ring-finger Distal	**94.2**	44.39	**129.6**	104.65	**150**	91.63
Pinky Distal	**70.4**	82.72	**93.8**	103.34	**85.3**	67.44
Thenar	**64.5**	57.32	**68.7**	64.39	**53.6**	73.26
Hyper-Thenar 1	**85**	75.16	**82.7**	80.80	**126**	133.22
Hyper-Thenar 2	**91.3**	86.98	**141.3**	225.31	**114.3**	172.70
Metacarpal Head	**74.6**	40.43	**53.2**	36.45	**60.4**	43.36

Table 7.11: Average Values over Cohort (kPa) by Sensor Segment per Action: 5lb Cylinder. Top: Finger Tip. Bottom: Whole Hand. (Average:$\overline{x}$, Standard Deviation: σ)

	Push		**Pull**		**Lift**	
	Finger Tip					
	$\overline{x}$	σ	$\overline{x}$	σ	$\overline{x}$	σ
Thumb Distal	**239.6**	267.65	**138**	155.08	**182.8**	132.08
Fore-finger Distal	**103.2**	68.03	**128.3**	93.55	**206.9**	204.90
Middle-finger Distal	**90.4**	85.65	**139.9**	145.38	**203.5**	218.79
Ring-finger Distal	**89.7**	73.18	**130.5**	98.75	**214.2**	220.67
Pinky Distal	**129**	108.52	**107.6**	80.33	**129.8**	109.25
Thenar	**54.6**	23.21	**37**	19.82	**26.5**	20.94
Hyper-Thenar 1	**59**	67.53	**96.4**	161.72	**55.6**	115.45
Hyper-Thenar 2	**180.2**	217.27	**115.1**	103.73	**46.1**	45.58
Metacarpal Head	**50.8**	71.45	**24.1**	11.02	**26.4**	23.28

	Push		**Pull**		**Lift**	
	Whole Hand					
	$\overline{x}$	σ	$\overline{x}$	σ	$\overline{x}$	σ
Thumb Distal	**172.4**	134.29	**128.8**	91.96	**130.9**	131.52
Fore-finger Distal	**95.5**	63.66	**99.2**	73.31	**111.7**	112.79
Middle-finger Distal	**95.4**	66.40	**131.2**	65.60	**142.9**	126.46
Ring-finger Distal	**96**	58.01	**170.4**	125.90	**152.6**	106.89
Pinky Distal	**75.6**	66.86	**97.3**	58.55	**66.7**	58.76
Thenar	**62**	60.75	**64.7**	73.47	**64.6**	95.13
Hyper-Thenar 1	**88.6**	77.37	**88.7**	75.20	**170.5**	247.62
Hyper-Thenar 2	**68.7**	34.69	**84.5**	57.43	**82**	103.93
Metacarpal Head	**75.2**	55.93	**48.1**	23.72	**52.4**	49.98

Table 7.12: Average Values over Cohort (kPa) by Sensor Segment per Action: 10lb Cylinder. Top: Finger Tip. Bottom: Whole Hand (Average:$\overline{x}$, Standard Deviation: σ)

	Push **Finger Tip**		**Pull**		**Lift**	
	$\overline{x}$	σ	$\overline{x}$	σ	$\overline{x}$	σ
Thumb Distal	**241.7**	260.91	**124.7**	103.30	**151.2**	109.43
Fore-finger Distal	**180.3**	148.24	**264.4**	279.50	**337.8**	411.28
Middle-finger Distal	**109.7**	93.43	**197.5**	226.68	**229.5**	314.91
Ring-finger Distal	**126.5**	84.78	**125.1**	79.19	**156.1**	74.85
Pinky Distal	**103.8**	80.96	**122.9**	115.78	**169.1**	165.70
Thenar	**39.9**	32.64	**32.4**	25.32	**31.2**	24.48
Hyper-Thenar 1	**77.4**	73.06	**33.6**	30.68	**34.6**	35.45
Hyper-Thenar 2	**169.2**	267.11	**85.7**	71.69	**42.9**	42.44
Metacarpal Head	**42.8**	32.30	**26.8**	21.93	**53.1**	65.63

	Push **Whole Hand**		**Pull**		**Lift**	
	$\overline{x}$	σ	$\overline{x}$	σ	$\overline{x}$	σ
Thumb Distal	**174.1**	138.94	**125.2**	88.85	**215.3**	284.09
Fore-finger Distal	**214.6**	207.58	**191.4**	125.04	**163.3**	103.08
Middle-finger Distal	**143.4**	121.07	**176.9**	162.51	**238.2**	311.23
Ring-finger Distal	**133.1**	94.99	**207.6**	101.99	**214.7**	130.86
Pinky Distal	**129.6**	86.56	**142.7**	78.31	**170.2**	116.78
Thenar	**44.9**	23.82	**63.9**	54.44	**71.2**	101.63
Hyper-Thenar 1	**59.5**	45.34	**90.3**	86.76	**123.9**	97.17
Hyper-Thenar 2	**101.1**	61.11	**245.3**	183.64	**240.2**	379.30
Metacarpal Head	**107.5**	79.44	**165.4**	222.72	**160.9**	218.89

REFERENCES

[1] F. Mirza, "HUMAN ROBOT INTERACTION WITH 3D-PRINTED WHOLE BODY ROBOTIC," Master of Science in Electrical Engineering, University of Texas-Arlington, 2016.

[2] C. Nothnagle, J. R. Baptist, J. Sanford, W. H. Lee, D. O. Popa, and M. B. J. Wijesundara, "EHD printing of PEDOT: PSS inks for fabricating pressure and strain sensor arrays on flexible substrates," vol. 9494, p. 949403, 2015.

[3] K. B. Reed, M. Peshkin, M. J. Hartmann, J. Patton, P. M. Vishton, and M. Grabowecky, "Haptic cooperation between people, and between people and machines," in Intelligent Robots and Systems, 2006 IEEE/RSJ International Conference on, 2006, pp. 2109–2114.

[4] M. Vasic and A. Billard, "Safety issues in human-robot interactions," 2013 IEEE International Conference on Robotics and Automation, pp. 197–204, may 2013.

[5] V. Duchaine, N. Lauzier, M. Baril, M.-A. Lacasse, and C. Gosselin, "A flexible robot skin for safe physical human robot interaction," in Robotics and Automation, 2009. ICRA '09. IEEE International Conference on, 2009, pp. 3676–3681.

[6] S. Raspopovic, M. Capogrosso, F. M. Petrini, M. Bonizzato, J. Rigosa, G. Di Pino, J. Carpaneto, M. Controzzi, T. Boretius, E. Fernandez, G. Granata, C. M. Oddo, L. Citi, A. L. Ciancio, C. Cipriani, M. C. Carrozza, W. Jensen, E. Guglielmelli, T. Stieglitz, P. M. Rossini, and S. Micera, "Restoring natural sensory feedback in real-time bidirectional hand prostheses." Science translational medicine, vol. 6, no. 222, p. 222ra19, feb 2014.

[7] J. Rajruangrabin and D. O. Popa, "Enhancement of Manipulator Interactivity through Compliant Skin and Extended Kalman Filtering," 2007 IEEE International Conference on Automation Science and Engineering, pp. 1111–1116, sep 2007.

[8] P. S. Lum, C. G. Burgar, M. Van Der Loos, P. C. Shor, M. Majmundar, and R. Yap, "The MIME robotic system for upper-limb neuro-rehabilitation: Results from a clinical trial in subacute stroke," Proceedings of the 2005 IEEE 9th International Conference on Rehabilitation Robotics, vol. 2005, pp. 511–514, 2005.

[9] D. Popa, W. H. Lee, M. Wijesundara, N. Bugnariu, F. Lewis, Z. Celik-Butler, and D. Butler, "NRI Project #IIS 1208623: Multi-modal sensor skin and garments for healthcare and home robots," 2012.

[10] "Next Generation Systems Group."

[11] K. Ziegler-Graham, E. J. MacKenzie, P. L. Ephraim, T. G. Travison, and R. Brookmeyer, "Estimating the Prevalence of Limb Loss in the United States: 2005 to 2050," Archives of Physical Medicine and Rehabilitation, vol. 89, no. 3, pp. 422–429, 2008.

[12] W. Selpho, "William selpho," 1857.

[13] J. Retchenbagh, "Improvement in substitutes for artificial hands," 1865.

[14] D. W. Dorranoep, "Artificial hand," 1912.

[15] B. D. Argall and A. G. Billard, "A survey of Tactile HumanRobot Interactions," Robotics and Autonomous Systems, vol. 58, no. 10, pp. 1159–1176, oct 2010.

[16] I. Ranatunga, "MULTISENSORY INTEGRATION FOR ADAPTIVE PHYSICAL HUMAN-ROBOT INTERACTION," Ph.D. dissertation, 2015.

[17] C. Breazeal, C. D. Kidd, and E. al., "Effects of nonverbal communication on efficiency and robustness in human-robot teamwork," 2005.

[18] G. Taylor, R. Frederiksen, J. Crossman, M. Quist, and P. Theisen, "A multimodal intelligent user interface for supervisory control of unmanned platforms," in

Collaboration Technologies and Systems (CTS), 2012 International Conference on, 2012, pp. 117–124.

[19] S. Oviatt, R. Coulston, and R. Lunsford, “When Do We Interact Multimodally?: Cognitive Load and Multimodal Communication Patterns,” in Proceedings of the 6th International Conference on Multimodal Interfaces, ser. ICMI ’04. New York, NY, USA: ACM, 2004, pp. 129–136.

[20] A. Sanna, F. Lamberti, G. Paravati, and F. Manuri, “A Kinect-based natural interface for quadrotor control,” Entertainment Computing, no. 0, 2013.

[21] C. P. Quintero, R. T. Fomena, A. Shademan, N. Wolleb, T. Dick, and M. Jagersand, “SEPO : Selecting by Pointing as an Intuitive Human-Robot Command Interface,” no. Section II, pp. 1158–1163, 2013.

[22] D. Kim, O. Hilliges, S. Izadi, A. D. Butler, J. Chen, I. Oikonomidis, and P. Olivier, “Digits: Freehand 3D Interactions Anywhere Using a Wrist-worn Gloveless Sensor,” in Proceedings of the 25th Annual ACM Symposium on User Interface Software and Technology, ser. UIST ’12. New York, NY, USA: ACM, 2012, pp. 167–176.

[23] I. Ranatunga, N. A. Torres, N. Bugnariu, R. M. Patterson, C. Garver, and D. O. Popa, “Human-Robot Upper Body Gesture Imitation Analysis for Diagnosis and Treatment of Autism,” IEEE ... International Conference on Robotics and Automation, 2013.

[24] A. Habib, S. K. Das, I.-C. Bogdan, D. Hanson, and D. O. Popa, “Learning human-like facial expressions for Android Phillip K. Dick,” in Automation Science and Engineering (CASE), 2014 IEEE International Conference on, 2014, pp. 1159 – 1165.

[25] T. Kanda, H. Ishiguro, T. Ono, M. Imai, and R. Nakatsu, “Development and evaluation of an interactive humanoid robot ”Robovie”,” in Robotics and Automation,

2002. Proceedings. ICRA ’02. IEEE International Conference on, vol. 2, 2002, pp. 1848—-1855 vol.2.

[26] D. D. Rossi, F. Carpi, F. Lorussi, A. Mazzoldi, R. Paradiso, P. Scilingo, and A. Tognetti, “ELECTROACTIVE FABRICS AND WEARABLE BIOMONITORING DEVICES,” vol. 3, no. December, pp. 3–8, 2003.

[27] D. De Rossi, F. Carpi, and E. P. Scilingo, “Polymer based interfaces as bioinspired ’smart skins’.” Advances in colloid and interface science, vol. 116, no. 1-3, pp. 165–178, nov 2005.

[28] F. Lorussi, W. Rocchia, E. P. Scilingo, A. Tognetti, and D. De Rossi, “Wearable, redundant fabric-based sensor arrays for reconstruction of body segment posture,” Sensors Journal, IEEE, vol. 4, no. 6, pp. 807–818, 2004.

[29] A. Schmitz, P. Maiolino, M. Maggiali, L. Natale, G. Cannata, and G. Metta, “Methods and Technologies for the Implementation of Large-Scale Robot Tactile Sensors,” Robotics, IEEE Transactions on, vol. 27, no. 3, pp. 389–400, jun 2011.

[30] Tekscan, “FlexiForce Sensors: Standard FlexiForce Sensors for Force Measurement,” 2015.

[31] H. Iwata and S. Sugano, “Design of human symbiotic robot TWENDY-ONE,” pp. 580–586, 2009.

[32] “PPS RoboTouch: Pressure Profile Systems,” 2014.

[33] Y. Li and S. S. Ge, “Human–Robot Collaboration Based on Motion Intention Estimation,” IEEE/ASME Transactions on Mechatronics, vol. 19, no. 3, pp. 1007–1014, 2014.

[34] C. G. Burgar, P. S. Lum, P. C. Shor, and H. F. Machiel Van der Loos, “Development of robots for rehabilitation therapy: the Palo Alto VA/Stanford experience.” Journal of rehabilitation research and development, vol. 37, no. 6, pp. 663–73, 2000.

[35] S. E. Fasoli, H. I. Krebs, J. Stein, W. R. Frontera, and N. Hogan, "Effects of robotic therapy on motor impairment and recovery in chronic stroke," Archives of Physical Medicine and Rehabilitation, vol. 84, no. 4, pp. 477–482, 2003.

[36] I. L. Kahn, D. Reinkensmeyer, W. Z. Rymer, H. Fischer, J. Barbas, and H. Roth, "Robotic Therapy for Force Training of the Upper Extremity in Chronic Hemiparetic Stroke," p. 2006, 2006.

[37] P. S. Lum, C. G. Burgar, M. Van Der Loos, P. C. Shor, M. Majmundar, and R. Yap, "The MIME robotic system for upper-limb neuro-rehabilitation: Results from a clinical trial in subacute stroke," Proceedings of the 2005 IEEE 9th International Conference on Rehabilitation Robotics, vol. 2005, pp. 511–514, 2005.

[38] P. S. Lum, C. G. Burgar, and P. C. Shor, "Evidence for improved muscle activation patterns after retraining of reaching movements with the MIME robotic system in subjects with post-stroke hemiparesis," IEEE Transactions on Neural Systems and Rehabilitation Engineering, vol. 12, no. 2, pp. 186–194, 2004.

[39] M. Schuenke, E. Schulte, and U. Schumacher, General Anatomy and Musculoskeletal System, L. M. Ross, Ed. Thieme, 2014.

[40] R. A. R. C. Gopura, K. Kiguchi, and E. Horikawa, "A Study on Human Upper-Limb Muscles Activities during Daily Upper-Limb Motions," International Journal of Bioelectromagnetism, vol. 12, no. 2, pp. 54–61, 2010.

[41] G. Singh, S. Boddu, I. Chakravorty, G. M. Bairy, and M. Ganesh, "An instrumented glove for monitoring forces during object manipulation," pp. 212–215, 2013.

[42] J.-H. Lee, Y.-S. Lee, S.-H. Park, M.-C. Park, B.-K. Yoo, and S.-M. In, "A study on the human grip force distribution on the cylindrical handle by intelligent force glove(I-force glove)," pp. 966–969, 2008.

[43] C. Patten, J. Lexell, and H. E. Brown, “Weakness and strength training in persons with poststroke hemiplegia: Rationale, method, and efficacy ,” pp. 293–312, 2004.

[44] D. J. Magermans, E. K. J. Chadwick, H. E. J. Veeger, and F. C. T. Van Der Helm, “Requirements for upper extremity motions during activities of daily living,” Clinical Biomechanics, vol. 20, no. 6, pp. 591–599, 2005.

[45] A. K. Palmer, F. W. Werner, D. Murphy, and R. Glisson, “Functional wrist motion: A biomechanical study,” Journal of Hand Surgery, vol. 10, no. 1, pp. 39–46, apr 1985.

[46] K. Petuskey, A. Bagley, E. Abdala, M. a. James, and G. Rab, “Upper extremity kinematics during functional activities: Three-dimensional studies in a normal pediatric population,” Gait and Posture, vol. 25, no. 4, pp. 573–579, 2007.

[47] J. Aizawa, T. Masuda, T. Koyama, K. Nakamaru, K. Isozaki, A. Okawa, and S. Morita, “Three-dimensional motion of the upper extremity joints during various activities of daily living,” Journal of Biomechanics, vol. 43, no. 15, pp. 2915–2922, apr 2015.

[48] C. J. van Andel, N. Wolterbeek, C. A. M. Doorenbosch, D. H. Veeger, and J. Harlaar, “Complete 3D kinematics of upper extremity functional tasks,” Gait & Posture, vol. 27, no. 1, pp. 120–127, apr 2015.

[49] L. J. Hargrove, K. Englehart, and B. Hudgins, “A comparison of surface and intramuscular myoelectric signal classification.” IEEE Transactions on Bio-medical Engineering, vol. 54, no. 5, pp. 847–53, may 2007.

[50] S. A. Dalley, S. Member, D. A. Bennett, and M. Goldfarb, “Functional Assessment of a Multigrasp Myoelectric Prosthesis : An Amputee Case Study,” IEEE Internation Conference on Robotics and Automation, pp. 2625–2629, 2013.

[51] J. T. Belter, J. L. Segil, A. M. Dollar, and R. F. Weir, “Mechanical design and performance specifications of anthropomorphic prosthetic hands: a review.” Journal of Rehabilitation Research and Development, vol. 50, no. 5, pp. 599–618, jan 2013.

[52] M. R. Dawson, F. Fahimi, and J. P. Carey, “The development of a myoelectric training tool for above-elbow amputees.” The Open Biomedical Engineering Journal, vol. 6, pp. 5–15, jan 2012.

[53] V. Mathiowetz, G. Volland, N. Kashman, and K. Weber, “Adult Norms for the Box and Block Test of Manual Dexterity.pdf,” American Journal of Occupational Therapy, vol. 39, no. 6, p. 6, 1985.

[54] P. M. Pilarski, M. R. Dawson, T. Degris, J. P. Carey, and R. S. Sutton, “Dynamic switching and real-time machine learning for improved human control of assistive biomedical robots,” 2012 4th IEEE RAS & EMBS International Conference on Biomedical Robotics and Biomechatronics (BioRob), pp. 296–302, jun 2012.

[55] M. Asghari Oskoei and H. Hu, “Myoelectric control systemsA survey,” Biomedical Signal Processing and Control, vol. 2, no. 4, pp. 275–294, oct 2007.

[56] L. Hargrove, K. Englehart, and B. Hudgins, “The effect of electrode displacements on pattern recognition based myoelectric control.” Conference proceedings : ... Annual International Conference of the IEEE Engineering in Medicine and Biology Society. IEEE Engineering in Medicine and Biology Society. Conference, vol. 1, pp. 2203–6, jan 2006.

[57] A. J. Young, L. J. Hargrove, and T. A. Kuiken, “The effects of electrode size and orientation on the sensitivity of myoelectric pattern recognition systems to electrode shift,” IEEE Transactions on Biomedical Engineering, vol. 58, no. 9, pp. 2537–2544, 2011.

[58] E. Scheme, A. Fougner, Ø. Stavdahl, a. C. Chan, and K. Englehart, “Examining the adverse effects of limb position on pattern recognition based myoelectric

control." Conference proceedings : ... Annual International Conference of the IEEE Engineering in Medicine and Biology Society. IEEE Engineering in Medicine and Biology Society. Conference, vol. 2010, pp. 6337–40, jan 2010.

[59] G. C. Ray and S. K. Guha, "Equivalent Electrical Representation of the Sweat Layer and Gain Compensation of the EMG Amplifier," IEEE Transactions on Biomedical Engineering, vol. BME-30, no. 2, pp. 130–132, 1983.

[60] M. Abdoli-Eramaki, C. Damecour, J. Christenson, and J. Stevenson, "The effect of perspiration on the sEMG amplitude and power spectrum," Journal of Electromyography and Kinesiology, vol. 22, no. 6, pp. 908–913, 2012.

[61] N. a. Dimitrova and G. V. Dimitrov, "Interpretation of EMG changes with fatigue: Facts, pitfalls, and fallacies," Journal of Electromyography and Kinesiology, vol. 13, no. 1, pp. 13–36, 2003.

[62] M. Tomasini, S. Benatti, F. Casamassima, B. Milosevic, S. Fateh, E. Farella, and L. Benini, "Digitally Controlled Feedback for DC Offset Cancellation in a Wearable Multichannel EMG Platform," in Engineering in Medicine and Biology Society (EMBC), 2015 37th Annual International Conference of the IEEE, 2015, pp. 3189–3192.

[63] W. Craelius, R. L. Abboudi, and N. A. Newby, "CONTROL OF A MULTI-FINGER PROSTHETIC HAND," International Conference on Rehabilitation Robotics, Stanford, CA, pp. 255–260, 1999.

[64] D. J. Curcie, J. A. Flint, W. Craelius, and L. Member, "Biomimetic Finger Control by Filtering of Distributed Forelimb Pressures," IEEE Transactions on Neural Systems and Rehabilitation Engineering, vol. 9, no. 1, pp. 69–75, 2001.

[65] S. L. Phillips and W. Craelius, "Residual kinetic imaging : a versatile interface for prosthetic control," Robotica, vol. 23, pp. 277–282, 2005.

[66] A. Radmand, E. Scheme, and K. Englehart, “HIGH RESOLUTION MUSCLE PRESSURE MAPPING FOR UPPER LIMB PROSTHETIC CONTROL,” in Myoelectric Controls/ Powered Prosthetics Symposium, N. Brunswick, Ed., 2014.

[67] A. Radmand, Erik Scheme, and Kevin Englehart, “On the Suitability of Integrating Accelerometry Data with Electromyography Signals for Resolving the Effect of Changes in Limb Position during Dynamic Limb Movement,” Journal of prosthetics and orthotics: JPO, vol. 26, 2014.

[68] A. A. Polliack, R. C. Sieh, D. D. Craig, S. Landsberger, D. R. Mcneil, and E. Ayyappa, “Scientific validation of two commercial pressure sensor systems for prosthetic socket fit,” Prosthetics and Orthotics International, vol. 24, pp. 63–73, 2000.

[69] M. Wininger, N.-h. Kim, and W. Craelius, “Pressure signature of forearm as predictor of grip force,” Journal of Rehabilitation Research & Development, vol. 45, no. 6, 2008.

[70] F. Mobasser and K. Hashtrudi-zaad, “Hand Force Estimation using Electromyography Signals,” in Proceedings of the 2005 IEEE International Conference on Robotics and Automation, 2005, pp. 31–36.

[71] F. Chan, Y.-S. Yang, F. K. Lam, Y.-T. Zhang, and P. A. Parker, “Fuzzy EMG classification for prosthesis control,” Rehabilitation Engineering, IEEE Transactions on, vol. 8, no. 3, pp. 305–311, 2000.

[72] A. Chan and K. Englehart, “Continuous classification of myoelectric signals for powered prostheses using gaussian mixture models,” Proceedings of the 25th Annual International Conference of the IEEE Engineering in Medicine and Biology Society (IEEE Cat. No.03CH37439), vol. 3, pp. 0–3, 2003.

[73] Y. Huang, K. B. Englehart, S. Member, B. Hudgins, and A. D. C. Chan, "Scheme for Myoelectric Control of Powered Upper Limb Prostheses," IEEE Transaction on Biomedical Engineering, vol. 52, no. 11, pp. 1801–1811, 2005.

[74] M. Derry and B. Argall, "Extending Myoelectric Prosthesis Control with Shapable Automation: A First Assessment," in Proceedings of the 2014 ACM/IEEE International Conference on Human-robot Interaction, ser. HRI '14. New York, NY, USA: ACM, 2014, pp. 455–462.

[75] M. A. Oskoei and H. Hu, "GA-based Feature Subset Selection for Myoelectric Classification," 2006 IEEE International Conference on Robotics and Biomimetics, pp. 1465–1470, 2006.

[76] ——, "Support vector machine-based classification scheme for myoelectric control applied to upper limb." IEEE transactions on bio-medical engineering, vol. 55, no. 8, pp. 1956–65, aug 2008.

[77] M. B. I. Reaz, M. S. Hussain, and F. Mohd-Yasin, "Techniques of EMG signal analysis: detection, processing, classification and applications (Correction)." Biological procedures online, vol. 8, no. 1, p. 163, 2006.

[78] A. Fougner, E. Scheme, A. D. C. Chan, K. Englehart, and O. Stavdahl, "Resolving the limb position effect in myoelectric pattern recognition." IEEE transactions on neural systems and rehabilitation engineering : a publication of the IEEE Engineering in Medicine and Biology Society, vol. 19, no. 6, pp. 644–51, dec 2011.

[79] A. Fougner, M. Sæther, Ø. Stavdahl, P. J. Kyberd, and J. Blum, "CANCELLATION OF FORCE INDUCED ARTIFACTS IN SURFACE EMG USING FSR MEASUREMENTS," in MEC '08 Measuring Success in Upper Limb Prosthetics,' Proceedings of the 2008 MyoElectric Controls/Powered Prosthetics Symposium, held in Fredericton, New Brunswick, Canada, August 1315, 2008., New Brunswick, Canada, 2008, pp. 13–16.

[80] C. Assad, M. Wolf, T. Theodoridis, K. Glette, and A. Stoica, "BioSleeve: A Natural EMG-based Interface for HRI," in Proceedings of the 8th ACM/IEEE International Conference on Human-robot Interaction, ser. HRI '13. Piscataway, NJ, USA: IEEE Press, 2013, pp. 69–70.

[81] M. T. Wolf, C. Assad, M. T. Vernacchia, J. Fromm, and H. L. Jethani, "Gesture-Based Robot Control with Variable Autonomy from the JPL BioSleeve," IEEE International Conference on Robotics and Automation (ICRA), pp. 1160–1165, 2013.

[82] P. Axelsson, "A Simulation Study on the Arm Estimation of a Joint Flexible 2 DOF Robot Arm A Simulation Study on the Arm Robot Arm," Tech. Rep., 2009.

[83] P. Axelsson and M. Norrlöf, "Method to Estimate the Position and Orientation of a Triaxial Accelerometer Mounted to an Industrial Manipulator," in 10th International IFAC Symposium on Robot Control, Dubrovnik, Croatia., 2012.

[84] P. Axelsson, "Sensor Fusion and Control Applied to Industrial Manipulators," Ph.D. dissertation, Linköping University, 2014.

[85] M. Quigley, R. Brewer, S. P. Soundararaj, V. Pradeep, Q. Le, and A. Y. Ng, "Low-cost accelerometers for robotic manipulator perception," 2010 IEEE/RSJ International Conference on Intelligent Robots and Systems, pp. 6168–6174, oct 2010.

[86] Y. Wang, W. Chen, and M. Tomizuka, "Extended Kalman Filtering for Robot Joint Angle Estimation Using MEMS Inertial Sensors," pp. 406–413, 2013.

[87] E. Grood and W. Suntay, "A Joint Coordinate System forthe Clinical Description of Three-Dimensional Motions: Applications to the knee," Transactions of the ASME, vol. 105, 1983.

[88] X. Chen, "Human Motion Analysis with Wearable Inertial Sensors," 2013.

[89] M. Djuric-Jovicic, N. Jovicic, and D. Popovic, “Kinematics of Gait: New Method for Angle Estimation Based on Accelerometers,” Sensors, vol. 11, pp. 10 571–10 585, 2011.

[90] S. Jónsdóttir, “Validation and Biomechanical Measurements using a Novel Inertial Measurement Unit Validation and Biomechanical Measurements using a Novel Inertial Measurement Unit,” no. June, 2014.

[91] J. F. S. Lin and D. Kuli, “Human pose recovery using wireless inertial measurement units,” Physiological Measurement, no. 33, pp. 2099–2115, 2012.

[92] T. Seel and T. Schauer, “Joint Axis and Position Estimation from Inertial Measurement Data by Exploiting Kinematic Constraints,” pp. 0–4, 2012.

[93] W. Dong, I.-M. Chen, K. Y. Lim, and Y. K. Goh, “Measuring uniaxial joint angles with a minimal accelerometer configuration,” i-CREATe 2007 - Proceedings of the 1st International Convention on Rehabilitation Engineering and Assistive Technology in Conjunction with 1st Tan Tock Seng Hospital Neurorehabilitation Meeting, pp. 88–91, 2007.

[94] A. T. M. Willemsen, C. Frigo, and H. Boom, “Lower extremity angle measurement with accelerometers–error and sensitivity analysis.” IEEE Transactions on Bio-Medical Engineering, vol. 38, no. 12, pp. 1186–1193, 1991.

[95] S. Choudhury, Y. Wang, W. Chen, and M. Tomizuka, “Accurate Determination of Joint Angles from Inertial Measurement Unit Data,” pp. 406–413, 2013.

[96] M. A. El-gohary and J. Mcnames, “Joint Angle Tracking with Inertial Sensors,” Ph.D. dissertation, Portland State University, 2013.

[97] L. Vargas, A. Elias, A. Frizera, and E. Rocon, “BODY TO SENSOR CALIBRATION PROCEDURE FOR LOWER LIMB JOINT ANGLE ESTIMATION APPLIED TO IMU-BASED GAIT ANALYSIS,” in Brazilian Congress on Biomedical Engineering - CBEB 2014, 2014, pp. 777–780.

[98] B. Kamalizonouzi, “Optimal Inertial Sensor Placement and Motion Detection for Epileptic Seizure Patient Monitoring,” Ph.D. dissertation, The University of Western Ontario, 2012.

[99] T. Brunner, J.-p. Lauffenburger, S. Changey, and M. Basset, “Magnetometer-Augmented IMU Simulator: In-Depth Elaboration,” Sensors, vol. 15, pp. 5293–5310, 2015.

[100] M. Engesser, A. R. Franke, M. Maute, D. C. Meisel, and J. G. Korvink, “Miniaturization limits of piezoresistive MEMS accelerometers,” Microsystem Technologies, vol. 15, no. 12, pp. 1835–1844, 2009.

[101] ——, “A robust and flexible optimization technique for efficient shrinking of MEMS accelerometers,” Microsystem Technologies, vol. 16, no. 4, pp. 647–654, 2010.

[102] F. a. Levinzon, “Fundamental Noise Limit of Piezoelectric Accelerometer,” IEEE Sensors Journal, vol. 4, no. 1, pp. 108–111, 2004.

[103] K. Tyagi, “Second Order Training Algorithms For Radial Basis Function Neural Network,” Ph.D. dissertation, University of Texas Arlington, 2011.

[104] K. Tyagi and M. T. Manry, “Fuzzy C-Means Clustering Based Construction And Training For Second Order RBF Network,” pp. 248–255, 2011.

[105] T. Rakthanmanon, B. Campana, A. Mueen, G. Batista, B. Westover, Q. Zhu, J. Zakaria, and E. Keogh, “Searching and mining trillions of time series subsequences under dynamic time warping,” Proceedings of the 18th ACM SIGKDD International Conference on Knowledge Discovery and Data Mining, pp. 262–270, 2012.

[106] K. Fukunaga, “Statistical Pattern Stas-tical Pattern Recognit ion,” Pattern Recognition, vol. 22, no. 7, pp. 833–834, 1990.

[107] R.O. Duda, P.E. Hart, and D.G. Stork, Pattern Classification, 2nd ed., J. W. &. Sons, Ed., 2001.

[108] T. Wagner, “”Covergence of the nearest neighbor rule”,” IEEE Transactions on Information Theory,, vol. 17 (5),, no. x, pp. 566–571, 1971.

[109] A. Papoulis, Probability, random variables, and stochastic processes. New York, NY, USA: McGraw-Hill, 1965, no. 1.

[110] E. Gribovskaya and A. Billard, “Learning Nonlinear Multivariate Dynamics of Motion in Robotic Manipulators,” International Journal of Robotics Research, pp. 1–26, 2010.

[111] P. M. Yanik, J. Manganelli, J. Merino, A. L. Threatt, J. O. Brooks, K. E. Green, and I. D. Walker, “A gesture learning interface for simulated robot path shaping with a human teacher,” IEEE Transactions on Human-Machine Systems, vol. 44, no. 1, pp. 41–54, 2014.

[112] C. Nul, M. Q. Meng, P. X. Liu, X. Wmg, H. Chao, and W. Xiang, “Visual gesture recognition for human-machine interface of robot teleoperation,” in Intelligent Robots and Systems, 2003. (IROS 2003). Proceedings. 2003 IEEE/RSJ International Conference on, vol. 2, no. October, 2003, pp. 1560—-1565 vol.2.

[113] I. Guyon, V. Athitsos, P. Jangyodsuk, and H. J. Escalante, “The ChaLearn gesture dataset (CGD 2011),” Machine Vision and Applications, vol. 25, no. 8, pp. 1929–1951, 2014.

[114] S. Escalera, J. Gonzàlez, X. Baró, M. Reyes, O. Lopes, I. Guyon, V. Athitsos, and H. Escalante, “Multi-modal gesture recognition challenge 2013,” Proceedings of the 15th ACM on International conference on multimodal interaction - ICMI ’13, pp. 445–452, 2013.

[115] C. Conly, Z. Zhang, and V. Athitsos, “An evaluation of RGB-D skeleton tracking for use in large vocabulary complex gesture recognition,” … of the 7th International Conference on …, 2014.

[116] Z. Zhang, C. Conly, and V. Athitsos, "Hand Detection on Sign Language Videos," Proceedings of the 7th International Conference on PErvasive Technologies Related to Assistive Environments, pp. 26:1—-26:5, 2014.

[117] P. Jangyodsuk and C. Conly, "Sign Language Recognition using Dynamic Time Warping and Hand Shape Distance Based on Histogram of Oriented Gradient Features," Pervasive Technologies Related to Assistive Environments (PETRA), pp. 1–6, 2014.

[118] N. Neverova, C. Wolf, G. W. Taylor, and F. Nebout, "ModDrop: adaptive multi-modal gesture recognition," pp. 1–14, 2014.

[119] P. Neto, D. Pereira, J. N. Pires, and A. Paulo Moreira, "Real-Time and Continuous Hand Gesture Spotting: an Approach Based on Artificial Neural Networks," Karlsruhe, Germany, May 6-10, 2013, 2013.

[120] J. Sanford, R. Patterson, and D. Popa, "Surface EMG and Intra-socket Force Measurement to Control a Prosthetic Device," Next-Generation Robotics II; and Machine Intelligence and Bio-inspired Computation: Theory and Applications IX, vol. 9494, 2015.

[121] R. Rawat, J. K. Patel, and M. T. Manry, "Minimizing validation error with respect to network size and number of training epochs." Neural Networks (IJCNN), The 2013 International Joint Conference on. IEEE, no. Aug, pp. 1–7, 2013.

[122] R. Duda, P. Hart, and D. Stork, Pattern Classification. John Wiley and Sons, 2001.

[123] W. Karush, "Minima of Functions of Several Variables with Inequalities as Side Constraints." M.Sc., Univ. of Chicago, Chicago, Illinois, 1939.

[124] J. Sanford, C. Young, D. Popa, N. Bugnariu, and R. Patterson, "Grip Pressure Measurements during activities of daily life," in SPIE 9116, Next-Generation Robots and Systems, vol. 9116, 2014, p. 91160H.

[125] J. Sanford, C. Young, S. Cremer, D. Popa, N. Bugnariu, and R. Patterson, “Grip Pressure and Wrist Joint Angle Measurement during Activities of Daily Life,” in Procedia Manufacturing: 6th International Conference on Applied Human Factors and Ergonomics (AHFE 2015) and the Affiliated Conferences, AHFE 2015, vol. 03, 2015, pp. 1450–1457.

[126] “Microsoft Kinect,” 2016.

[127] M. Quigley, C. Ken, B. P. Gerkey, J. Faust, T. Foote, J. Leibs, R. Wheeler, and A. Y. N. Y., “ROS: an open-source Robot Operating System,” in IEEE Int. Conf. on Robotics and Automation, Kobe, Japan, 2009.

[128] Y. LeCun and L. Bottou, “Neural Networks: Tricks of the Trade (Lecture Notes in Computer Science),” G. B. Orr and K.-R. Müller, Eds. Springer Berlin Heidelberg, 1998, ch. Efficient.

[129] S. S. Ge, Y. Li, and H. He, “Neural-network-based human intention estimation for physical human-robot interaction,” URAI 2011 - 2011 8th International Conference on Ubiquitous Robots and Ambient Intelligence, pp. 390–395, 2011.

[130] C. Chen, R. Jafari, and N. Kehtarnavaz, “Improving human action recognition using fusion of depth camera and inertial sensors,” IEEE Transactions on Human-Machine Systems, vol. 45, no. 1, pp. 51–61, 2015.

[131] “Sensitronics, LLC.”

[132] B. Hudgins, P. Parker, and R. N. Scott, “A New Strategy for Multifunction Myoelectric Control.pdf,” IEEE Transactions on Bio-medical Engineering, vol. 40, pp. 82–94, 1993.

[133] J. Sanford, O. Yetkin, S. Cremer, and D. Popa, “A Novel EMG-Free Prosthetic Interface System Using Intra-Socket Force Measurement and Pinch Gestures,” in The 8th ACM International Conference on PErvasive Technologies Related to Assistive Environments, 2015.

[134] "3dMD," 2016.

[135] M. F. Møller, "A Scaled Conjugate Gradient Algorithm for Fast Supervised Learning Supervised Learning," Neural Networks, vol. 6, pp. 525–533, 1993.

[136] A. Y. Ng, "Coursera: Stanford University Machine Learning Course," 2016.

[137] "Instamorph Moldable Plastic," 2015.

[138] "Arduino," 2015.

[139] "Touch Bionics," 2014.

[140] "Alja-safe Alginate," 2014.

[141] "Worbla Thermoplastic," 2014.

[142] "Ottobock Prosthetics, Ottobock USA," 2016.

[143] P. K. Artemiadis and K. J. Kyriakopoulos, "EMG-based teleoperation of a robot arm in planar catching movements using ARMAX model and trajectory monitoring techniques," Robotics and Automation, 2006. ICRA 2006. Proceedings 2006 IEEE International Conference on, pp. 3244–3249, 2006.

[144] B.R. Munson, D.F. Young and T. Okiishi, Fundamentals of Fluid Mechanics. John Wiley and Sons, 2002.